UNCLASSIFIED

AD NUMBER

AD909688

NEW LIMITATION CHANGE

TO

Approved for public release, distribution unlimited

FROM

Distribution authorized to U.S. Gov't. agencies only; Test and Evaluation; 1 Apr 1971. Other requests shall be referred to Space and Missile Systems Organization, Norton AFB, CA.

AUTHORITY

SAMSO USAF ltr, 8 Nov 1978

THIS PAGE IS UNCLASSIFIED

THIS REPORT HAS BEEN DELIMITED
AND CLEARED FOR PUBLIC RELEASE
UNDER DOD DIRECTIVE 5200.20 AND
NO RESTRICTIONS ARE IMPOSED UPON
ITS USE AND DISCLOSURE.

DISTRIBUTION STATEMENT A

APPROVED FOR PUBLIC RELEASE;
DISTRIBUTION UNLIMITED.

SAMSO TR No. 73-129

AD909688

FINAL PROGRESS REPORT

ADVANCED PENETRATION PROBLEMS PROGRAM

February 1973

Prepared by:

A. Demetriades and A. J. Laderman

of

Philco-Ford Corporation
Aeronutronic Division
Newport Beach, California

Monitored by:

Space and Missile Systems Organization
Air Force Systems Command
Norton Air Force Base, California

Under Contract

F04701-71-C-0035

D D C
RECEIVED
MAY 9 1973
C

Distribution limited to U.S. Government Agencies only; Reason: Test and Evaluation; Date statement applied; 1 April 1972; Other requests for this document must be referred to Space and Missile Systems Organization (RSSE), Los Angeles AFS, California 90009.

SAMSO TR No. 73-129

FINAL PROGRESS REPORT

ADVANCED PENETRATION PROBLEMS PROGRAM

February 1973

Prepared by:

A. Demetriades and A. J. Laderman

of

Philco-Ford Corporation
Aeronutronic Division
Newport Beach, California

Monitored by:

Space and Missile Systems Organization
Air Force Systems Command
Norton Air Force Base, California

Under Contract

F04701-71-C-0035

Distribution limited to U.S. Government Agencies only; Reason: Test and Evaluation; Date statement applied; 1 April 1972; Other requests for this document must be referred to Space and Missile Systems Organization (RSSE), Los Angeles AFS, California 90009.

FOREWORD

This document describes the work performed by the Philco-Ford Corporation under the Advanced Penetration Problems project (APP) Contract F04701-71-C-0035 in the period 1971-1972. In the present period, emphasis was placed on the study of boundary-layer turbulence at supersonic and hypersonic Mach numbers, on the effect of altitude changes on the structure of the near wake behind a cone, and the statistical features of far wakes and ionized jets. The principal investigator of the project is Dr. Anthony Demetriades of the Fluid Mechanics Section, Research Laboratory, at the Newport Beach facility (Telephone 640-1500, Extension 1841). Project Scientists are Dr. Demetriades and Dr. Arnold Laderman, also of the Fluid Mechanics Section (Telephone 640-1500, Extension 1012). The work has had the able support of Mr. L. Von Seggern and Mr. E. L. Doughman at the Philco-Ford Supersonic Wind-Tunnel.

The present effort was sponsored jointly by SAMSO, United States Air Force and the U. S. Army Advanced Ballistic Missile Defense Agency (ABMDA). In addition to the Philco-Ford tunnel, facilities utilized for tests included the 21" Hypersonic Wind-Tunnel at NASA's Jet Propulsion Laboratory and Tunnel B at the Von Karman Facility at AEDC, Tullahoma, Tennessee. The courtesy extended by the General Electric Co. in making available the porous cone model for the latter tests is gratefully acknowledged. Also, the cooperation is acknowledged of the Von Karman Facility personnel for designing, fabricating and installing the hot-wire shield and actuator device utilized at Tunnel B.

This report has been reviewed and approved by

Leonard T. Atkins
Contracting Officer
Space and Missile Systems Organization
Air Force Systems Command
Los Angeles, California 90009

ABSTRACT

The study of turbulence on a flat plate at Mach 9.4 has been completed with the discovery that the pressure fluctuations predominate, that the velocity fluctuations are very small and that wall-cooling has a strong influence in decreasing the temperature fluctuations. Tests have been performed at AEDC/B to extend these results to the cone geometry, to broaden the Mach- and Reynolds-numbers matrix and to investigate ablation effects. Although still incomplete, analysis of the data show very large temperature fluctuations due to the adiabatic wall, relatively little change of the turbulence level past the transition point, and discernible but small fluctuation increase for small mass injection rates. Correlations have began of all the available boundary-layer turbulence data for the purpose of scaling the fluctuation distribution to arbitrary flight conditions. Thus far the available correlation schemes fit the velocity fluctuation data only in the outer half of the layer. Better success is enjoyed for the temperature difference between the wall and the external flow. Experiments were also conducted to measure the transverse velocity fluctuation component and the turbulent shear stresses with specially-developed hot-wire probes; these data are now available on tape. In the near-wake investigation the completed mean-flow measurements were analyzed and show that a "plateau" tends to form as the Reynolds number increases beyond BLT. The turbulent viscosity was measured and was found to decrease beyond BLT as predicted by the AVCO theory. Other theoretical predictions, such as the radial distribution of velocity beyond the neck, were also verified. Fluctuation measurements revealed that the shoulder expansion nearly destroys the velocity but not the temperature fluctuations, and that the wake is "double-structured" beyond the neck. The study of electron, velocity and temperature space-time correlations in the far wake has been completed.

Page iv Intentionally Left Blank

CONTENTS

SECTION		PAGE
I	SUMMARY OF MAJOR FINDINGS	1
II	TURBULENT BOUNDARY LAYER MEASUREMENTS AT M = 9.4	4
	2.1 Summary of Previous Work	4
	2.2 Further Turbulence Characteristics of the Boundary Layer	5
	2.2.1 Consistency Checks: Pressure Gradient and Sub-layer Thickness	5
	2.2.2 Status of TBL-A Results: New Findings	8
	2.3 Study of Turbulence at Reduced Reynolds Number	8
III	HYPERSONIC CONE BOUNDARY LAYER EXPERIMENT	16
	3.1 Objective	16
	3.2 Hot-Wire Survival Tests	16
	3.3 Final Experiment Design	19
	3.3.1 Test Facility	19
	3.3.2 Test Hardware	22
	3.3.3 Instrumentation	26
	3.3.4 Test Procedure	29
	3.4 Test Results	38
	3.4.1 Phase III Tests	38
	3.4.2 Phase IV Tests	43
	3.5 Status and Plans	50
IV	CORRELATION OF BOUNDARY LAYER FLUCTUATION RESULTS	53
	4.1 Available Experimental Data	53
	4.2 Velocity-Fluctuation Correlations	53
	4.3 Temperature-Fluctuation Correlations	56
	4.4 Conclusions from the Correlation Study	60
	4.5 Status and Plans	62
V	MEASUREMENT OF SHEAR STRESSES IN A HYPERSONIC BOUNDARY LAYER	63
	5.1 Purpose	63
	5.2 Summary of Previous Work	63
	5.3 Present Status	63

CONTENTS (Continued)

SECTION		PAGE
VI	THE NEAR WAKE OF A CONE	70
	6.1 Summary of Previous Work	70
	6.2 Further Reduction of the Mean Flow Data	72
	6.3 Results of the Mean Flow Measurements	74
	6.3.1 Characterizing Parameters	74
	6.3.2 Expectations from Intuition and Finson's Theory	75
	6.3.3 The Mean Flow Properties	76
	6.4 Turbulence Properties	85
	6.4.1 Method of Collecting the Data	85
	6.4.2 Preliminary Results of the Turbulence Measurements	89
VII	ELECTRON SPACE-TIME CORRELATIONS IN TURBULENT PLASMAS	96
APPENDIX		
A	EFFECT OF SURFACE CURVATURE ON PROBE HEIGHT	97
B	X-PROBE RESPONSE WITH PRESSURE FLUCTUATIONS	103
C	CONE DRAG BUDGET	110
D	COMPUTER PROGRAM WEB-IV (DRB4E)	116
E	A CRITERION ESTABLISHING A MINIMUM REYNOLDS NUMBER FOR THE EXISTENCE OF TURBULENCE	125
REFERENCES		126

ILLUSTRATIONS

FIGURE		PAGE
1.	Evidence of pressure gradient normal to the wall at supersonic and hypersonic speeds.	6
2.	Variation of sublayer thickness normalized with the boundary layer thickness.	7
3.	Variation of pressure, density, temperature and velocity fluctuation intensities in the boundary layer.	9
4.	Turbulence Reynolds number variation across the hypersonic boundary-layer	10
5.	Final results on the integral scale length distribution.	11
6.	Fluctuation intensity distribution in the JPL/HWT boundary layer at P_0 = 1700 cm Hg abs	13
7.	Comparison of the Strong Reynolds Analogy in the boundary layer for 1700 cm Hg and 3200 cm Hg.	14
8.	Comparison of scale lengths for the 1700 cm and 3200 cm case . .	15
9.	Instrumentation rake used for hot-wire survival tests located in free-stream of AEDC Tunnel B.	17
10.	Schematic of AEDC Tunnel B	21
11.	Vacuum enclosure used to provide access to hot-wires. (a) Operating Position, (b) Raised Position.	23
12.	Photograph of GE cone model located in access tank	24
13.	Location of cone surface pressure and temperature gauges	25
14.	Philco-Ford instrumentation rake with probes installed. From front to back: pitot probe, hot-wire, surface sensor, total temperature probe.	27
15.	Hot-wire anemometer.	28
16.	Details of mean flow probes.	30
17.	Photograph of probe traversing mechanism located on top of test section showing hot-wire shield in raised and lowered positions.	31
18.	Photograph of Philco-Ford probes located within cone boundary layer at x = 37 inch station	32

ILLUSTRATIONS (Cont'd)

FIGURE		PAGE
19.	Block diagram of turbulence measurement instrumentation in configuration A.	36
20.	Block diagram of turbulence measurement instrumentation in configuration B.	37
21.	Photograph of turbulence measurement station located just downstream of wind tunnel test section	39
22.	Shadowgraph of cone boundary layer for Re/ft = 1.7×10^6 and P_o = 350 psi. (A) $\lambda = 0$, (B) $\lambda = 0.0015$.	42
23.	Shadowgraph of cone boundary layer for Re/ft = 2.6×10^6 and P_o = 600 psi. (A) $\lambda = 0$, (B) $\lambda = 0.0015$.	44
24.	Shadowgraph of cone boundary layer for Re/ft = 3.7×10^6 and P_o = 850-psi. (A) $\lambda = 0$, (B) $\lambda = 0.0015$.	45
25.	Typical variation of wideband hot-wire signal at fixed overheat current across the boundary layer showing effect of Reynolds number and blowing rate.	46
26.	Typical spectra of hot-wire signals for: (A) turbulent boundary layer, and (B) "laminar like" boundary layer. Each curve corresponds to fixed overheat current	48
27.	Typical mode diagrams of hot-wire data for P_o = 350 psi, $\lambda = 0$, at x-Station = 39 inches. Open circles indicate data points and solid lines represent curve fits used to deduce fluctuation intensities.	49
28.	Results of preliminary analysis showing velocity and temperature fluctuations at P_o = 350 psi	51
29.	Results of preliminary analysis showing velocity and temperature fluctuations at P_o = 600 psi	52
30.	Longitudinal wideband turbulence component in boundary-layers (u and $\overline{u}_e$ correlations).	55
31.	Longitudinal wideband turbulence component in boundary-layers (u_T correlation)	57
32.	Correlation of wideband longitudinal velocity fluctuations based on friction-velocity scheme for compressible flow.	58

ILLUSTRATIONS (Cont'd)

FIGURE		PAGE
33.	Wideband static temperature fluctuations in boundary layers. . .	59
34.	Correlation of wideband temperature fluctuations in supersonic/ hypersonic boundary-layers	61
35.	Nusselt number - Reynolds number calibration for X-probe No. 11.	65
36.	Recovery factor - Reynolds number calibration for X-probe No. 11	66
37.	Nusselt number - Reynolds number calibration for X-probe No. 4 .	68
38.	Recovery factor - Reynolds number calibration for X-probe No. 4.	69
39.	Experiment matrix for the WEM (near wake) tests.	71
40.	Measured drag of the near wake	78
41.	Variation of wake velocity defect on near-wake axis with Re_D solid curve is from far-wake experiment.	79
42.	Eddy kinematic viscosity measured in the near wake	81
43.	Variation of the turbulent Prandtl No. σ_T along near wake axis for each Re_D. Straight line in each graph is the fully-turbulent wake expectation ($\sigma_T = 0.84$).	82
44.	Radial variation of non-dimensional longitudinal velocity in the near wake (Highest-Re_D turbulent boundary layer)	83
45.	Radial variation of non-dimensional static temperature in the near wake (highest-Re_D turbulent boundary layer)	84
46.	Diagram of electronic components used in measuring the near-wake turbulence.	86
47.	Wideband velocity and temperature fluctuations in the region $0 < X < 0.8D$ of the turbulent near-wake (Re = 178,000)	91
48.	Wideband temperature and longitudinal velocity fluctuations in the near wake.	92
49.	Velocity fluctuations in post-BLT near wake as viewed in fluid and ground-fixed coordinates	93

ILLUSTRATIONS (Cont'd)

FIGURE		PAGE
A1.	Location of probes relative to cone surface with sense probe contacting cone.	98
A2.	Location of probes relative to cone surface showing effect of surface curvature on true probe height	99
A3.	Approximation for true probe height above cone surface	101

LIST OF TABLES

TABLE		PAGE
I	RESULTS OF HOT-WIRE ENDURANCE TESTS - MAY 18-23.	20
II	ORIGINAL TEST MATRIX FOR AEDC TURBULENCE MEASUREMENTS. . . .	34
III	FINAL TEST MATRIX FOR TURBULENCE MEASUREMENTS.	35
IV	AEDC CONE BOUNDARY-LAYER EXPERIMENT.	40
V	EXPERIMENTS SUPPLYING HIGH-SPEED BOUNDARY-LAYER TURBULENCE DATA	54

NOMENCLATURE

A	Area
A_w'	Non-dimensional hot-wire overheat
BLT	Boundary-layer transition
C_D	Drag coefficient
$(C_D A)_w^{\frac{1}{2}}$	Effective drag diameter of wake
C_{D_ℓ}	Laminar friction drag coefficient
C_{D_p}	Drag coefficient due to pressure forces
C_{D_v}	Viscous drag coefficient
C_f	Friction coefficient
C_f	Hot-wire circuit constant
D	Body base diameter
$D(i)$	Approximate true height of probe i above cone surface
d	Diameter of hot-wire
d_w	wake diameter
e	Hot-wire mean voltage
e'	Instantaneous hot-wire fluctuating voltage signal
e_m	Hot-wire sensitivity to mass flux fluctuations
e_T	Hot-wire sensitivity to total temperature fluctuations
e_ξ	Hot-wire sensitivity to transverse component of vorticity fluctuations
e_π	Hot-wire sensitivity to sound field fluctuations
e_π^*	Sound mode sensitivity coefficient for skewed hot-wire
e_σ	Hot-wire sensitivity to entropy fluctuations
e_η	Hot-wire sensitivity to longitudinal component of vorticity fluctuations.

NOMENCLATURE (Continued)

F	D.C. voltage related to low-frequency fluctuations
F_N	D.C. voltage related to low-frequency fluctuation noise
f	frequency
$f(M)$	Function of Mach number
f_o	Low-frequency used as a "zero-frequency limit"
G	Low-frequency amplifier gain
$g(M,n_x)$	Friction of Mach number and longitudinal component on normal vector
H_1,H_2,H_3	Constants of curve-fitting η versus Re
$H(i)$	True height of probe i above cone surface
$h(M,n_y)$	Function of Mach number and longitudinal component of normal vector
i	Current
J	Transfer function of wave analyzer
K	Non-dimensional hot-wire overheat parameter
k	Heat conductivity; also, constant appearing in $\tilde{u}$, $\tilde{T}$ variations
L	Wake transverse scale
$L(i)$	Lateral displacement of probe i from vertical through cone axis
ℓ	Length of hot-wire
M	Mach number
$\dot{m}$	Mass-injection flux
m'	Instantaneous mass flux fluctuation normalized with respect to local mean mass flux
N_1,N_2	Constants in curve-fit Nu_m versus Re
Nu	Nusselt number
Nu_m	Nusselt number (measured)

NOMENCLATURE (Continued)

n_x	Component of normal vector in longitudinal direction
n_y	Component of normal vector in transverse direction
P	Pressure
P_b	Base pressure
p	e_T; also, pressure
p'	Instantaneous sound field fluctuation normalized with respect to local mean strength of sound field
$Q^2(f=0)$	(As in $e^2(f=0)$ spectral density of Q at f = 0
q	p cot Ø; also, dynamic pressure; also, heat-transfer rate
R	Hot-wire resistance
R_c	Local cone radius
Re	Reynolds number
Re'	Unit Reynolds number
Re_s	Reynolds number based on distance s along cone ray.
Re_w	Wake Reynolds number
Re_Λ	Turbulence Reynolds number
$Re_{\infty,D}$	Cone Reynolds number based on ambient conditions and base diameter
R(i)	Distance between cone center and probe (i)
R_o	Hot-wire resistance at 0^oC
R_T	Turbulent Reynolds number
R_θ	Momentum-thickness Reynolds number
$R_{\sigma\pi}$	Correlation coefficient such as entropy-pressure
r	Cone base radius; also, e_σ
$r_{\sigma T}$	Temperature-velocity cross-correlation

NOMENCLATURE (Continued)

S	Cone drag integral
S_1	Cone drag integral based on viscous drag only
S_2	Cone drag integral based on pressure drag only
s	e^*; also, distance along cone ray
T	Temperature
T'	Instantaneous static temperature fluctuation normalized with respect to local mean static temperature
$\tilde{T}$	Non-dimensional mean static temperature
T_{aw}	Hot-wire temperature (adiabatic recovery)
T_T'	Instantaneous total temperature fluctuation normalized with respect to local mean total temperature
T_w	Hot-wire temperature
t_1, t_2	Transfer function of rms voltmeters in wake tests
u	Velocity
u'	Instantaneous longitudinal velocity fluctuation normalized with respect to local mean velocity
$\tilde{u}$	Non-dimensional mean velocity
u_τ	Friction velocity
$\overline{u'T'}$	Correlation of non-dimensional longitudinal velocity and temperature fluctuations
$\overline{u'v'}$	Correlation of non-dimensional longitudinal and transverse velocity fluctuations
V	Mean hot-wire voltage
v'	Instantaneous transverse velocity fluctuation normalized with respect to local mean velocity
$\overline{v'T'}$	Correlation of non-dimensional transverse velocity and temperature fluctuations

NOMENCLATURE (Continued)

w	Velocity defect
X	Overheat parameter $\equiv e_T/e_\sigma$
x	Axial, or longitudinal, distance
$\bar{x}$	Non-dimensional distance along wake axis
x_n	Distance of wake neck (from cone base)
Y	Non-dimensional rms hot-wire voltage fluctuation
Y_F	Analogous to Y for the narrow-band data in the wake test
Y_{FF}	Analogous to Y for the wide band data in the wake test
y	Distance along the normal to the surface or wake axis
$\tilde{y}$	Normal distance in Howarth coordinates
$y+$	Non-dimensional normal distance
$y_o(i)$	Vertical displacement between the bottom of the surface sense probe and the probe i
Z	D.C. voltage output of wide band data (wake test)
Z_F	Non-dimensional narrow-band fluctuations
Z_N	Noise equivalent of Z
α	Function of Mach number
α_o	First hot-wire resistivity coefficient at 0^oC
β	Function of Mach number
γ	Ratio of specific heats
δ	Boundary layer thickness
δ_L	Sublayer thickness
ζ	Drag
η	Recovery factor; also, coordinate $\tilde{y}/L$

NOMENCLATURE (Continued)

θ	Momentum thickness; also, temperature defect; also, cone half-angle
$\theta(i)$	Angle between vertical and straight line connecting probe i to cone center
Λ	Integral turbulence scale
λ	Non-dimensional blowing rate
ν	Kinematic viscosity
$\bar{\nu}_T$	Eddy kinematic viscosity
ξ'	Instantaneous transverse component of vorticity fluctuation normalized with respect to local mean vorticity
π'	Instantaneous sound field fluctuation normalized with respect to strength of local mean sound field
ρ	Density
ρ'	Instantaneous density fluctuation normalized with respect to local mean density
σ	$(\overline{\sigma'^2})^{\frac{1}{2}}$
σ'	Instantaneous entropy fluctuation normalized with respect to local mean entropy
σ_T	Turbulent Prandtl number
τ	$(\overline{\tau'^2})^{\frac{1}{2}}$
τ'	Instantaneous longitudinal component of vorticity fluctuation normalized with respect to local mean vorticity
τ_w	Wall friction
ϕ	Angle between hot-wire element and mean flow velocity vector; also, circumferential angle; also, slope of Nu-Re curve
ψ	Slope of recovery-factor versus Mach number curve

SUBSCRIPTS

e	Edge condition
o	Stagnation conditions
r	Recovery conditions
rms	Root mean square value
w	Wall condition
x,y,z	In the x, y, z directions
∞	Free-stream conditions

SUPERSCRIPTS

$(\overline{\ })$	Denotes time averaged mean value
$(\ )'$	RMS fluctuation

SECTION I

SUMMARY OF MAJOR FINDINGS

In the present contract period a major portion of the work was concentrated on the definition of hypersonic boundary-layer turbulence properties. In actual flight the problem requires knowledge of a thin boundary-layer ($\delta \ll$ the local body section diameter) on a cone with external Mach number $M_e \simeq 10$ to 12, Reynolds number R_θ from 10^4 to 10^5, heat rates such that $0.05 < T_w/T_o < 1$ and ablation rates $\dot{m}/\rho_e u_e$ ranging from 0 to 0.01. Since it is nearly impossible to produce these conditions in a single ground test suitable for turbulence measurements, scaling laws are required which can be formed by tests over a wider matrix of conditions.

Data from the $M_e = 9.4$, $R_\theta = 37{,}000$ tests at JPL/HWT (code-named "TBL-A") completed during 1971-1972 were re-examined and refined (see Section II), and a summary Technical Report has been issued separately (Reference 1). Doubts cast earlier on the ability of this test to represent highly "mature" layers have been dispelled because the vertical gradient $\partial p/\partial y$ has since been found to be independent of the wind tunnel. The pressure fluctuations p' have been found to be the dominant turbulence mode at high M_e, reaching 18% intensity, with the density, temperature and velocity fluctuations following in that order. Intermittency measurements made from the TBL-A tape library also showed an unexpectedly smooth ("unwrinkled") turbulent front implying, for example, reduced radar scattering from a very overdense layer as opposed to what would be predicted from low-Mach-number boundary-layer experience.

To apply the flat-plate lessons learned at JPL to a flight-realistic cone geometry, to supply further variations in M_e and R_θ and to introduce ablation simulation, tests have been performed at AEDC/B (code-named "TBL-C") in the experiments discussed in Section III. With the cooperation of AEDC personnel the initially serious problem of hot-wire anemometer survival and endurance in Tunnel B was resolved successfully. The tests were then performed at Mach 8 ($M_e \simeq 7$) at various combinations of R_θ, stations x from the cone tip and mass injection rates. The data are presently under reduction, but sufficient preliminary information is available to draw some conclusions. For example, it appears that mass injection as high as $\lambda \equiv \dot{m}/\rho_e u_e = 0.0015$ does not affect the maximum fluctuation magnitude in the layer. It also appears that the relative distribution of the velocity-vs-temperature fluctuations is not changed at AEDC over what had been found at JPL.

With such information now becoming available, a separate effort was set up to collect and correlate the turbulence data from TBL-A, TBL-C and other sources into a coherent picture (Section IV). Increasing M_e was found to cause a decrease of the velocity fluctuations u'. Tentatively, a correlation of the form $(u'/u_\tau)(\rho/\rho_w)^{\frac{1}{2}}$ vs y/δ was found to describe all data fairly well for $y/\delta > 0.5$, but only poorly closer to the wall, for a wide range of M_e, q and R_θ. On the other hand, the temperature fluctuations T' increase rapidly with M_e, appear to be independent of R_θ, and decrease rapidly as the wall temperature decreases below the adiabatic-recovery level. Fair-to-good success has been found in correlating the T' data with Kistler's original suggestion that the "driving force" for T' is the mean temperature drop

$T_w - T_e$ across the layer. Finally, the longitudinal integral scales of all variables but the pressure appear to follow a geometrical relation $\Lambda \sim \delta/5$ independent of M_e, R_θ and heat rate.

To measure the transverse turbulent components v' and the turbulent shear stresses u'v' and ρ'v', a test code-named TBL-B was performed during this period with specially-made crossed hot-wires ("X probes"). To reduce time and costs the now-familiar boundary-layer at JPL was again used. Section V describes the tests; this measurement was the first attempt ever made to obtain directly the ingredients of the "eddy viscosity" at speeds other than $M_e = 0$. By also obtaining v' it will be possible to resolve, at least partly, the question of isotropy which is usually assumed to hold in the boundary-layer. Provisions to reduce these data, which now exist on tape, had not been made in the contract; data reduction is provided for, however, in the 1972-1973 period.

The boundary-layer turbulence also defines initial conditions for wake formation. The wake development subsequent to the cone shoulder formed the second major effort area under this contract. Previously, a 5-degree half-angle cone had been placed in the Philco-Ford Supersonic Wind-Tunnel (PF/SWT) and its wake subjected to mean-flow measurements in an experiment code-named WEM. In the present period turbulence data were acquired behind the same cone as described in Section VI. The tests are performed in a background of urgent discussion in the defense community about the peculiarities of a wake formed when the vehicle boundary-layer is turbulent ("below BLT"). The main contention is that the shed boundary-layer structure decreases the wake eddy viscosity by its small scale and causes a delay in wake diffusion. However there had previously been no conclusive evidence that this contention was true. During this period continued analysis of the mean-flow data in $0 < x < 6D$ $(0 < x < 45(C_DA)^{\frac{1}{2}})$ showed that an increase of flight Reynolds number Re_D towards BLT and beyond causes an increase and a "flattening" of the wake velocity. Furthermore the eddy viscosity, when extracted from the data, showed the claimed decrease from the pre-BLT to the post-BLT case. On the other hand, the seemingly contradictory assumption of a Gaussian radial velocity profile beyond the neck was also verified. In fact these profiles are numerically almost identical to the known equilibrium far-wake profiles.

Quantitative turbulence measurements, covering most of the required matrix, were also made during this period. The technique used measures both the fluctuation intensities and their scales, from the body shoulder to $40(C_DA)^{\frac{1}{2}}$. It was found that the shoulder expansion indeed decreases the velocity fluctuations u', but that it hardly affects T'. This provides an explanation of the "turbulence persistence" seen in ballistic-range photographs. Indeed, due to the "Strong Reynolds Analogy" (i.e., kinetic-thermal energy exchange) the near-wake consists of a core of velocity fluctuations surrounded by an annulus of temperature fluctuations. Presently the shear layer and the boundary-layer are found to be equally responsible for creating this double structure.

In addition to the near wake studies, two projects remaining from an earlier contract period have been concluded. The space-time correlations of an equilibrium ("far") wake have been mapped and are now available for numerical insertion into scattering calculations. Also, the functional relations have been obtained between electron and gas-dynamical fluctuations in a turbulent plasma. Separate reports on these two projects will be issued soon.

In the course of the AEDC tests at $M_\infty = 8$, it was observed that for a considerable distance preceding transition the boundary-layer showed intense sinusoidal instabilities. These waves have been previously observed photographically, but never before quantitatively with turbulence-measuring probes. The wavelength found is approximately 1.7δ, the intensity nearly 30% (a large number considering that the turbulence levels were found to be about the same) and the spectral composition almost purely temperature. Since similar waves photographed elsewhere show the same wavelength, it has been concluded that this is a real effect which is important to the transition process.

SECTION II

TURBULENT BOUNDARY LAYER MEASUREMENTS AT M = 9.4

2.1 SUMMARY OF PREVIOUS WORK

Under the APP project, Philco-Ford has been investigating in detail the mean and fluctuating flow in a highly equilibrated (R_θ = 36,000) turbulent boundary-layer over a cooled wall at M_∞ = 9.4. The nozzle wall of the Jet Propulsion Laboratory's Hypersonic Wind-Tunnel (JPL/HWT) has been utilized because of its low cost, ease of access and the inherent advantages to the diagnostic methods of the large thickness (4 inches) of its boundary-layer. This project code-named "TBL-A" is the first serious, quantitative attack on the high-speed boundary-layer turbulence problem since 1957 and the first ever into its truly hypersonic regime.

During the 1971-1972 period the mean flow tests on this flow were completed and the results presented in Reference 2. For background purposes these results are abstracted below from that reference:

> "An experimental investigation was carried out to determine the structure of the turbulent boundary-layer on the wall of the Jet Propulsion Laboratory Hypersonic Wind-Tunnel at a free-stream Mach number of 9.37. Profiles of flow properties were obtained from pitot pressure, static pressure, and total temperature surveys made through the 4-inch thick boundary-layer at a station 160 inches from the nozzle throat. Tests were conducted primarily for the following conditions: unit free-stream Reynolds number of 127,000 per inch, corresponding to a Reynolds number based on momentum thickness of 36,800, and a wall-to-free-stream total temperature ratio of 0.385. A cursory examination of the boundary layer was also made at a unit stream Reynolds number of 67,000. The static pressure measurements, although indicating negligible streamwise variation, revealed the existence of a significant pressure gradient normal to the wall, with the pressure at the wall approximately 45% greater than its free-stream value. The data indicate that the profile of total-temperature-ratio-versus-velocity-ratio agrees with the linear Crocco theory in the sub-layer region, but in the outer portion of the boundary-layer, closely follows the quadratic relation which has been observed to characterize nozzle wall measurements. The data also indicate that the sub-layer is 0.05 to 0.10 inches thick which corresponds to only several percent of the total boundary-layer thickness. Correlation of the velocity profile with the conventional incompressible profile shows poor agreement in the sub-layer and wall-of the-wake regions, with the latter attributed primarily to the pressure gradient normal to the wall. However, the experimental skin friction coefficient agrees with the value predicted by the Van Driest theory within several percent. Finally, the total temperature profile determined from a hot-wire anemometer traverse through the boundary-layer is in good agreement with the thermocouple measurements."

The results of the turbulence study also completed to a large extent in the 1971-1972 period, were issued under a separate report (Reference 1) from which the abstract is produced below:

"An experiment has been performed to measure the distribution of fluctuations in a turbulent, cooled-wall boundary-layer in continuous flow at Mach 9.4. The 0.00001 inch diameter constant-current hot-wire anemometer was employed. The hot-wire signals have been interpreted both with and without aid from the "no-sound" assumption. Both signal interpretation schemes give results within 30% of each other. The fluctuation intensity in the boundary-layer was found to consist mainly of high-frequency pressure fluctuations, whose magnitude at the wall and beyond the layer edge agree with expectations. Static temperature fluctuations are lower than expected, and it is suggested that this is caused by wall cooling. The fluctuations in the longitudinal velocity component are generally small and numerically differ little from the lower Mach number results. The maturity of the boundary-layer was judged high because of the measured large turbulence Reynolds number and the observed inertial subrange in the spectra. In the latter no changes were noted from one convection variable to another, but the pressure spectra are different from the velocity and temperature spectra. The sublayer and boundary-layer thicknesses were determined by intermittency measurements, which also showed that turbulence bursts occur throughout the sublayer and occasionally reach the wall. The standard deviation of the boundary-layer front is much smaller than observed at low speeds."

Additional points of importance have been brought to light during the present period; these are described below.

2.2 FURTHER TURBULENCE CHARACTERISTICS OF THE BOUNDARY-LAYER

2.2.1 CONSISTENCY CHECKS: PRESSURE GRADIENT AND SUBLAYER THICKNESS

Since this experiment was crucial because it produced the long-desired turbulence information, it is important to ensure that its boundary-layer was not limited in its applicability. For example, we had observed a pressure gradient $\partial p/\partial y$ such that the wall static pressure $p_w = 1.43\ p_\infty$ (see Figure 15, Reference 2). This was considered unusual and was at first met with some skepticism; suggestions were advanced that it was peculiar to dynamic non-equilibrium effects in wind-tunnel nozzles. Since then, however, Owen (Reference 3) has presented a correlation of a similar effect for a number of experiments in the range $2 < M_\infty < 40$. Significantly his correlation, reproduced here in Figure 1, includes data on various bodies such as cones, wedges and flat plates in addition to data from nozzle walls. The Philco-Ford point, marked "TBL-A" is not far from Owen's correlation. The conclusion is that, within experimental accuracy, the pressure gradient found by Philco-Ford at JPL/HWT is a true effect not limited to wind-tunnel nozzle walls.

Another criterion for normalcy is the sublayer thickness δ_L. Figure 2 shows another finding by Owen (Reference 3) in which δ_L/δ is correlated with the parameter $M_e/R_\theta^{1/2}$. Again, the Philco-Ford results are in satisfactory agreement with this correlation, especially since the definition of δ_L and δ are subject to some error. In our case we chose δ_L as found from the intermittency data (see Section III, Reference 1).

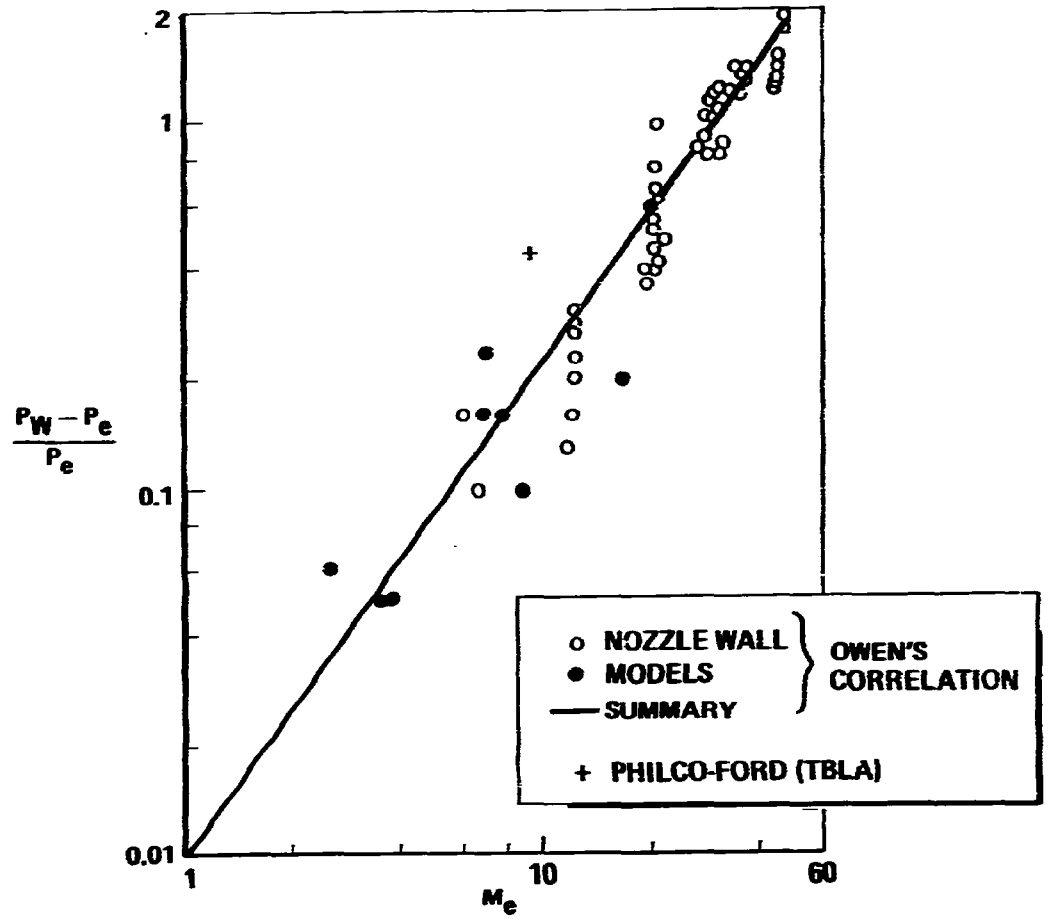

FIGURE 1. EVIDENCE OF PRESSURE GRADIENT NORMAL TO THE WALL AT SUPERSONIC AND HYPERSONIC SPEEDS.

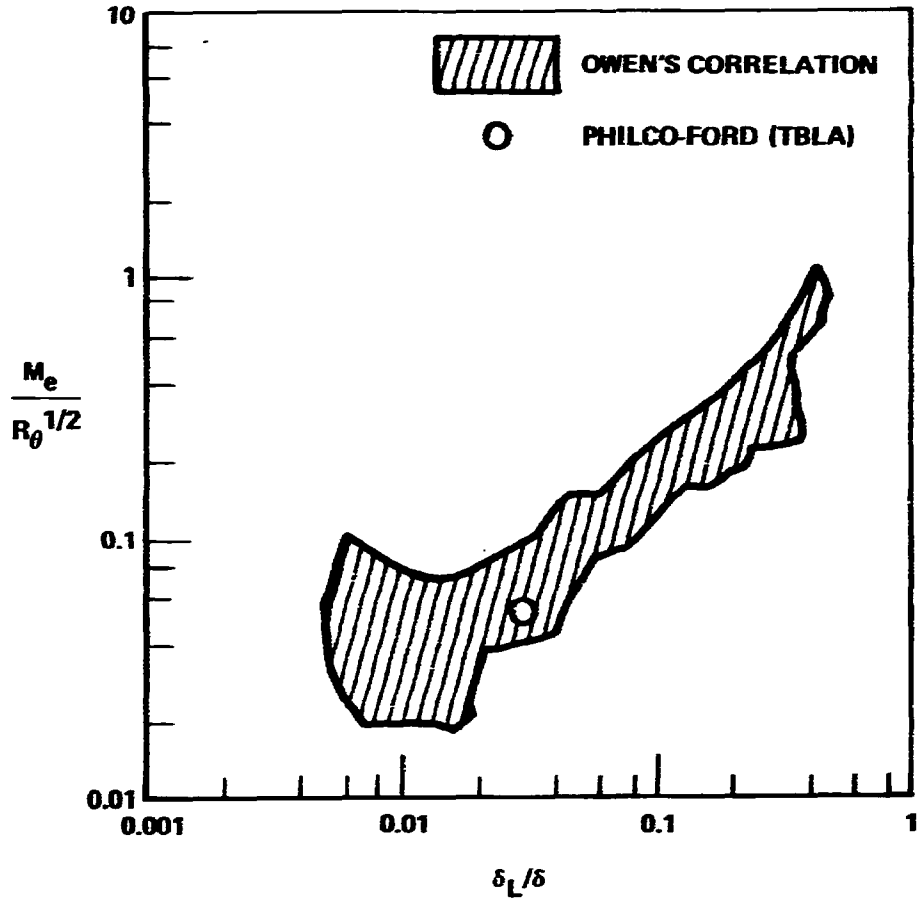

FIGURE 2. VARIATION OF SUBLAYER THICKNESS NORMALIZED WITH THE BOUNDARY LAYER THICKNESS.

2.2.2 STATUS OF TBL-A RESULTS: NEW FINDINGS

Following some minor refinements, the final distribution of p', ρ', T' and u' in the JPL/HWT boundary-layer is shown on Figure 3. Generally the fluctuations peak at the sublayer edge as well as in the main boundary-layer itself. Comments on extrapolating or interpolating these results to different flow conditions are given in Section IV.

Some other recent findings are also important. One, shown on Figure 4, is that the turbulence Reynolds number Re_Λ is extremely high. Since a high Re_Λ denotes also a highly equilibrated layer, and since the suspicions about the pressure gradient $\partial p/\partial y$ have now been allayed (Section 2.2.1), the extreme "maturity" of this boundary-layer has been confirmed.

Figure 5 plots the final picture of the distribution of integral lengths Λ. Repetitive tests with different sensors, interpreted in different ways, are in mutual agreement that Λ_u and Λ_T are concentrated at $\Lambda/\delta = 1.8/10 = 0.18$ with a "scatter" band of about 30%. However, the pressure scale Λ_p is much smaller. Presently the magnitude of Λ_p shown on Figure 5 is somewhat unsettled for the following reason. Like Λ_u and Λ_T, Λ_p is computed from the data via Taylor's hypothesis, i.e.,

$$\Lambda_p = \frac{u}{4}\left(\frac{p'^2(f=0)}{p'^2}\right)$$

where u is the local velocity, $p'^2(f = 0)$ the low-frequency spectral limit and p' the wideband pressure fluctuations. Within the test accuracy, $p'^2(f = 0)/p'^2$ (which is an integral time scale) is definitely known, but the factur u/4 used to convert to a space scale is, perhaps, used too prematurely. The point is that the propagation speed of p' is radically different from that of u' and T', which are known to convect with the local flow speed (Reference 4). Therefore the question of Λ_p cannot be finally settled unless a suitable propagation velocity is found to replace u.

2.3 STUDY OF TURBULENCE AT REDUCED REYNOLDS NUMBER

In addition to the TBL-A results presented above (and in Reference 1) which were done at $P_o = 3200$ cm Hg (Re = 49,500 per cm), some data are available on tape from tests at $P_o = 1700$ cm Hg (Re = 26,300 per cm). In the present contract period these data, too, were analyzed.

The experimental procedures, instrumentation and method of data reduction were identical to those described in Reference 1. The measurements were made using hot-wire 6-3, the same anemometer with which approximately one-half the turbulence data at $P_o = 3200$ cm Hg was acquired. Calculation of fluctuation intensities included the effect of non-zero pressure fluctuations using the assumption $R_{\sigma\pi} = R_{T\pi} = 0$, $R_{\sigma T} = -1$. The wideband fluctuation intensities of velocity, temperature and pressure, which were obtained from integrating over frequency the results of spectral modal analysis, are listed below as a function of distance from the wall, y. At each y position both the spectral results and the wideband mode diagram

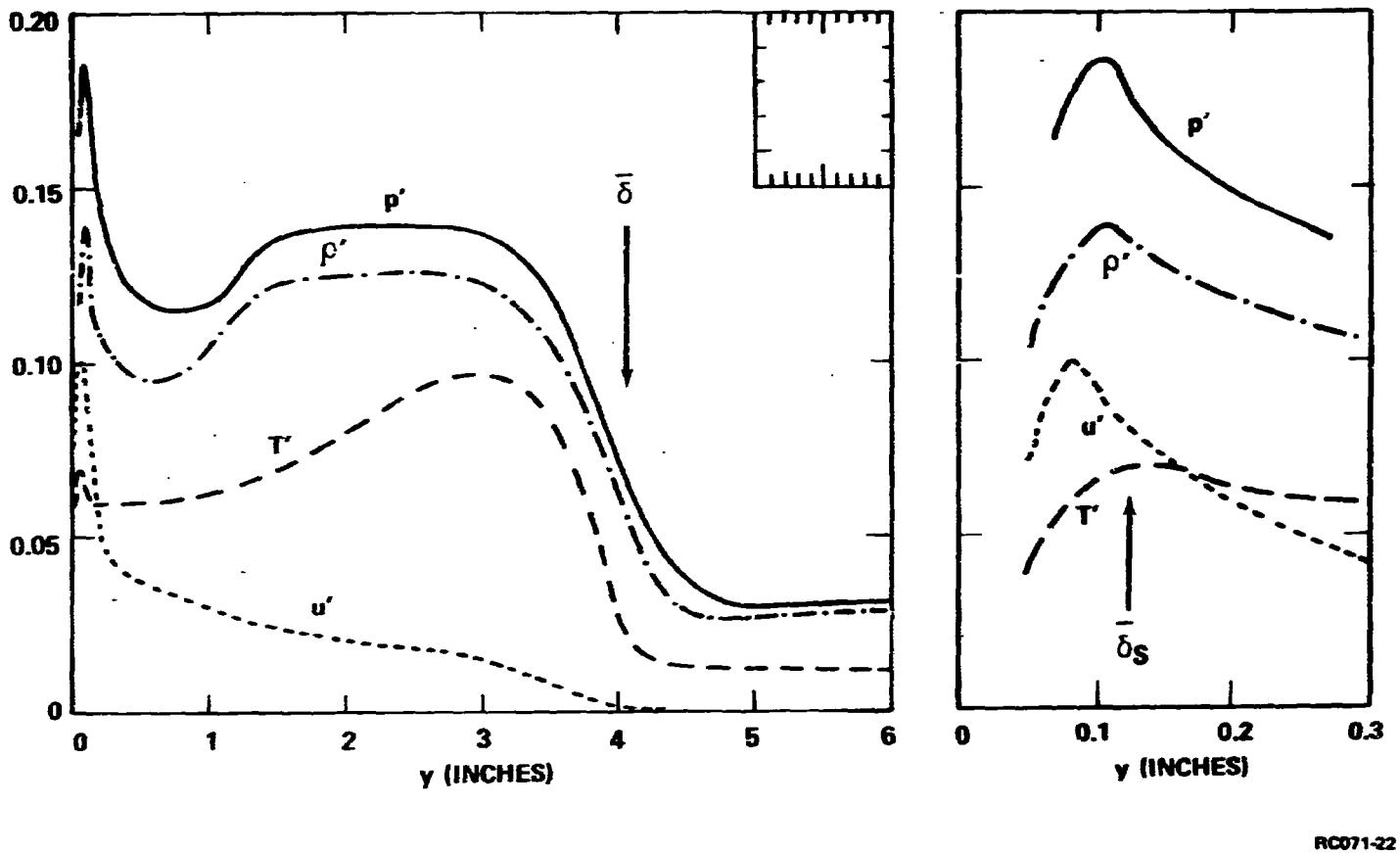

FIGURE 3. VARIATION OF PRESSURE, DENSITY, TEMPERATURE AND VELOCITY FLUCTUATION INTENSITIES IN THE BOUNDARY LAYER.

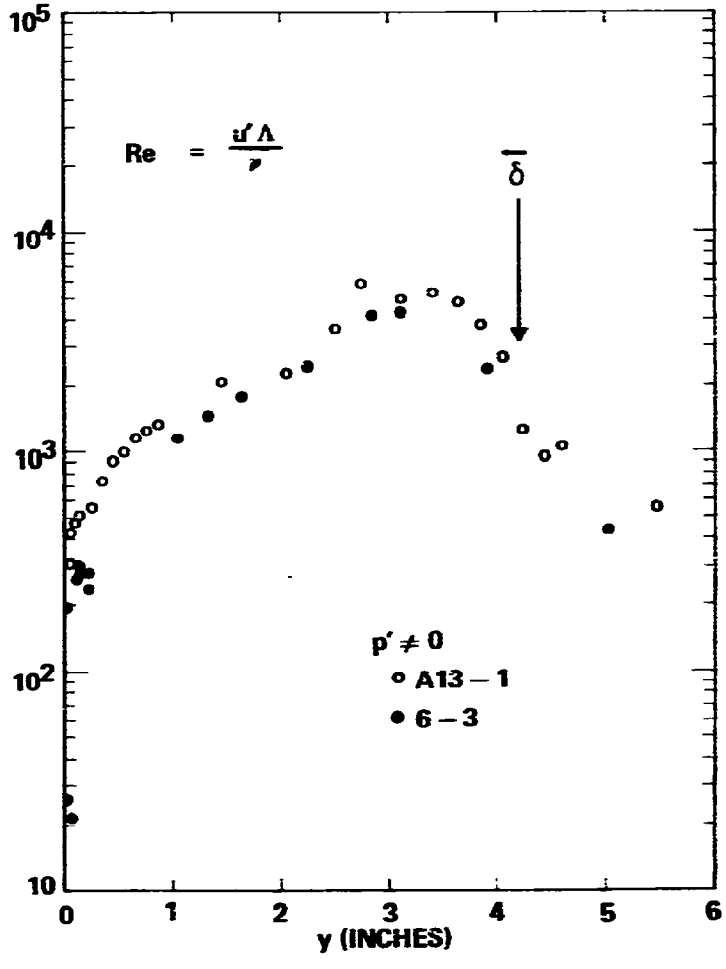

RC071-20

FIGURE 4. TURBULENCE REYNOLDS NUMBER VARIATION ACROSS THE HYPERSONIC BOUNDARY LAYER.

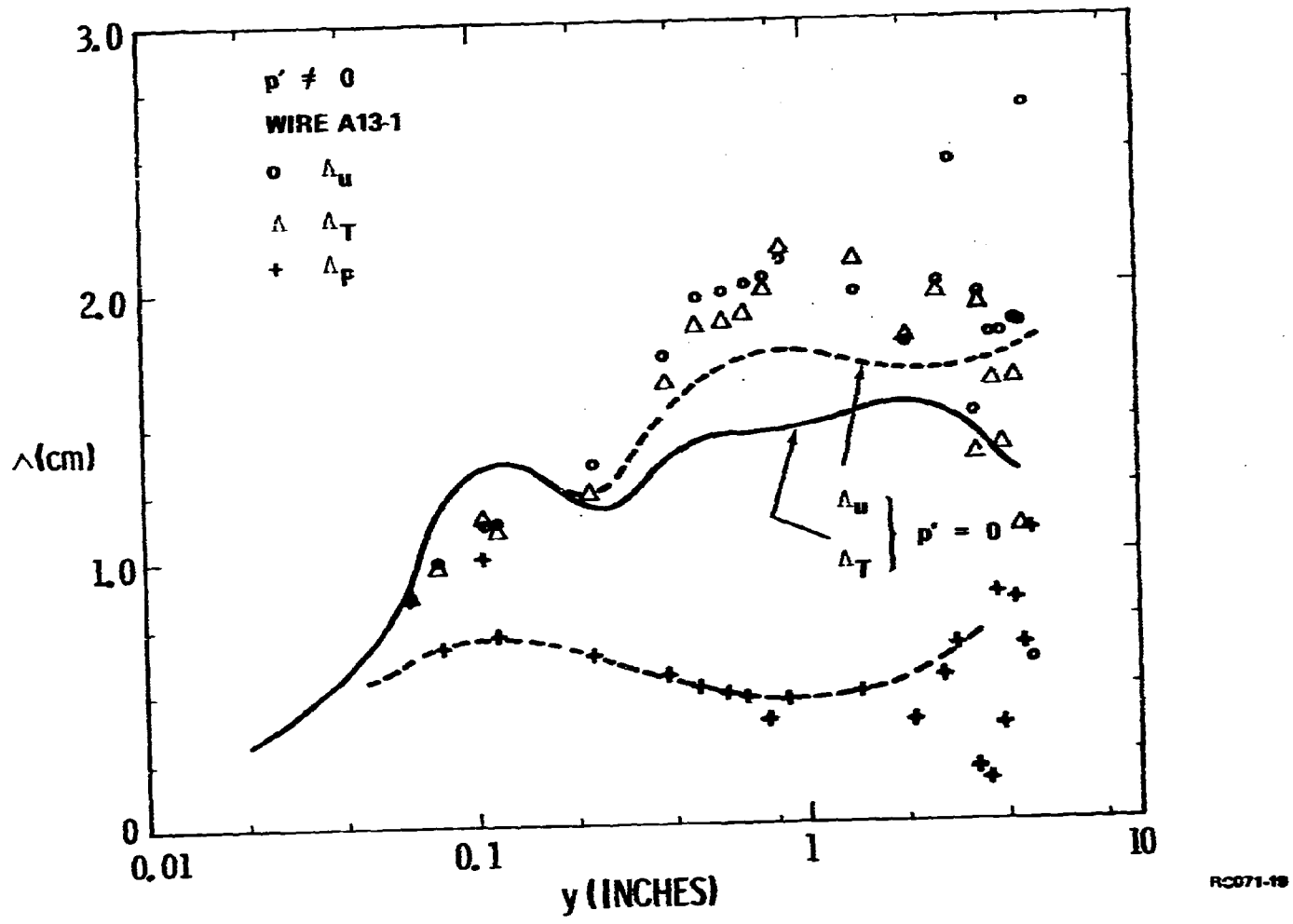

FIGURE 5. FINAL RESULTS ON THE INTEGRAL SCALE LENGTH DISTRIBUTION.

were carefully examined to assess the data and three points were found to be unacceptable. At y = 0.968 inches an excessive scatter in the data was observed which precluded a rational curve fit to find the fluctuation intensities. While the data was better behaved at y = 4.469 inches, errors in several low current data points resulted in negative mean square values for the turbulent fluctuations. Although the results of this point could be improved by eliminating the offending low current data points, this procedure was not carried out. Finally, at y = 2.967 inches, an error in the lowest current data point led to an overprediction in the pressure fluctuations by 50%. Since this y position is located near the point of peak fluctuations, a wideband analysis was carried out with the erroneous point omitted, yielding the corrected results listed below.

P_o = 1700 cm WIDEBAND FLUCTUATIONS

y	u'(%)	T'(%)	p'(%)
0.968	0.92	2.52	5.49
1.467	0.98	3.76	7.80
1.968	0.80	3.92	8.35
2.464	0.72	4.35	9.79
2.967	0.61	4.70	12.00
3.467	0.45	4.88	11.53
3.969	0.25	3.26	7.64
4.469	0.07	0.96	2.88
4.968	0.031	1.23	2.99

The seven acceptable results for velocity, temperature and pressure fluctuations are plotted in Figure 6 for comparison with the 3200 cm Hg results, which are represented by curves re-drawn from Figure 3. It is seen that near the outer edge of the boundary-layer ($y \geq 3.00''$) the results at the two pressures are in good agreement. Closer to the wall, however, the 1700 cm Hg results yield fluctuation intensities that are less than those at 3200 cm Hg, particularly the temperature fluctuations which differ by as much as a factor of two. In making such a comparison it should be recalled that of the two hot-wires used at 3200 cm Hg, wire 6-3 consistently gave results that were slightly smaller and this may be reflected in the results at 1700 cm Hg.

Figures 7 and 8 show, respectively, the variation of the quantity $T'/(\gamma-1)M^2u'$ and the integral scale lengths, Λ, as a function of y. In foth figures, the agreement between the results obtained at the two tunnel pressures is quite good. In view of this it is not clear whether the difference in fluctuation intensities obtained within the interior of the boundary-layer is due to the change in Reynolds number corresponding to the two tunnel pressures, or is a consequence of the peculiarities of the hot-wire with which the data was acquired. Since the former alternative is in variance with other evidence (see Section IV) it raises a need to continue and intensify the search for the Reynolds number effect on the boundary-layer turbulence.

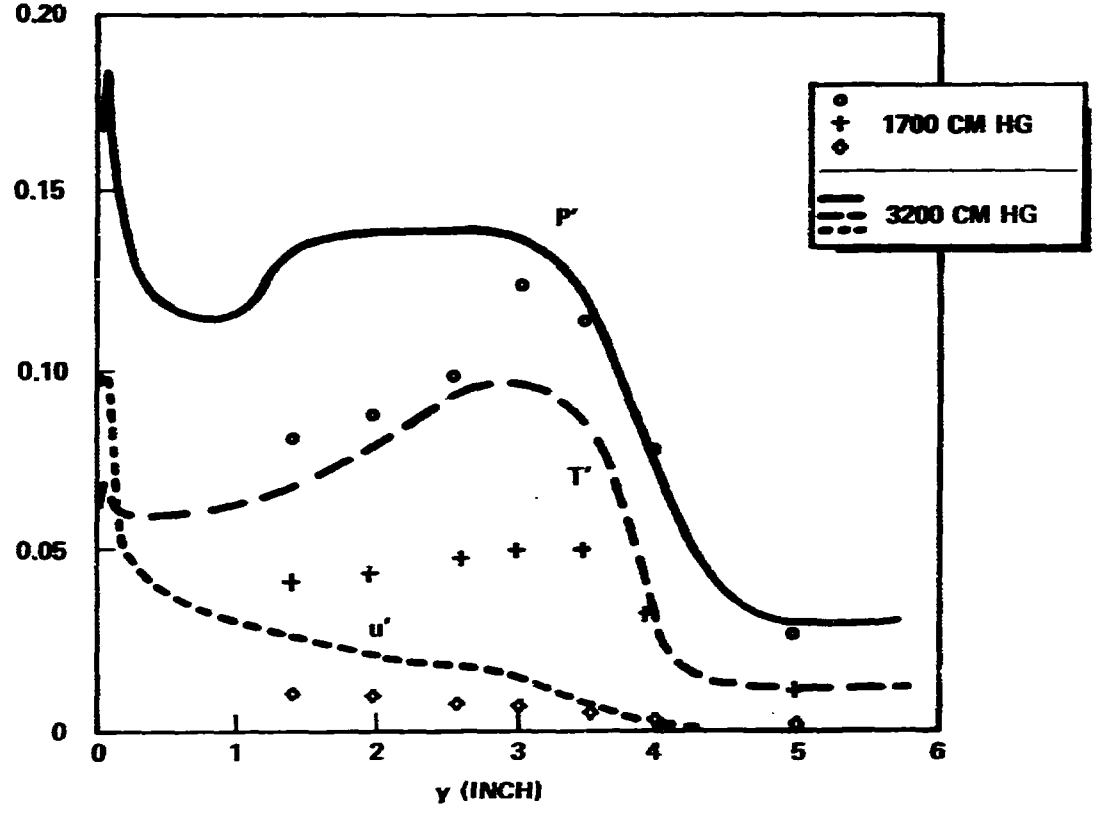

FIGURE 6. FLUCTUATION INTENSITY DISTRIBUTION IN THE JPL/HWT BOUNDARY LAYER AT P_o = 1700 cm Hg and 3200 cm Hg.

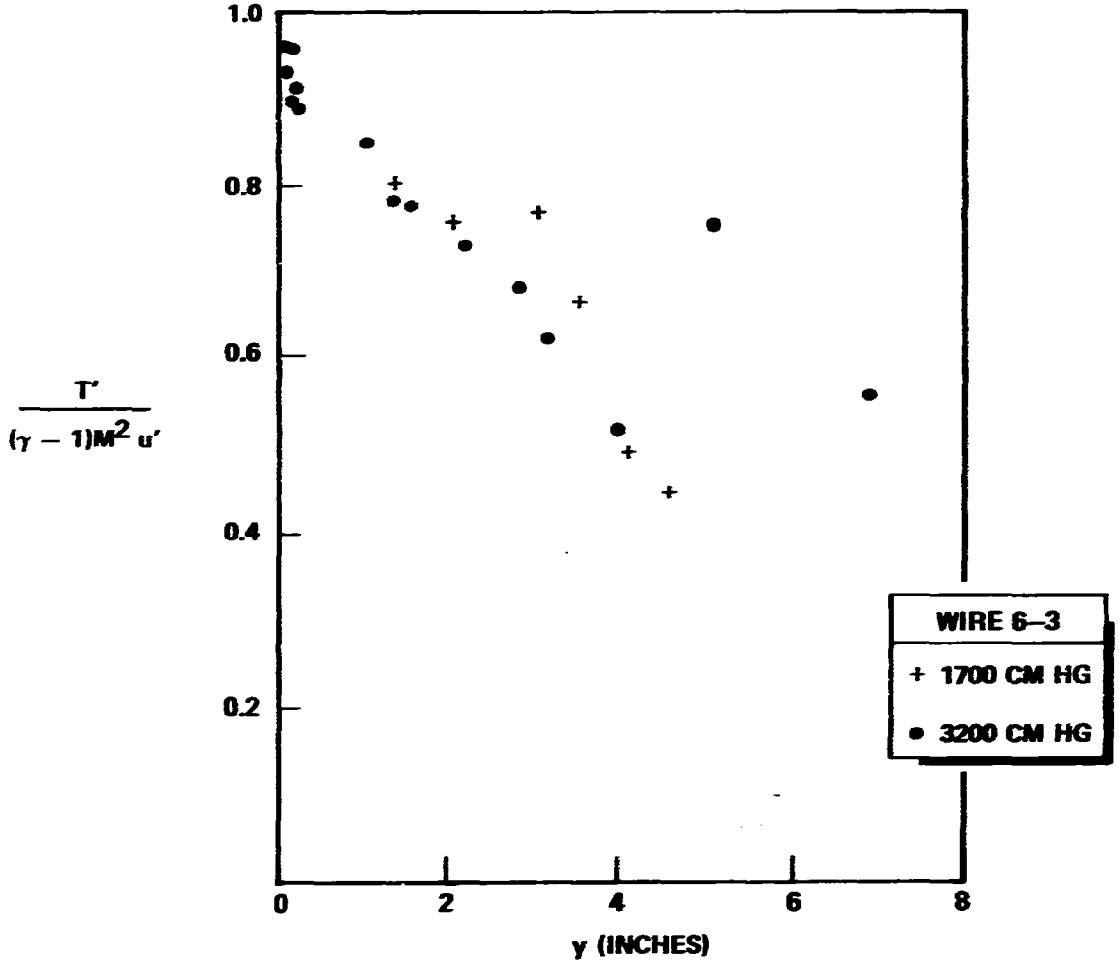

FIGURE 7. COMPARISON OF THE STRONG REYNOLDS ANALOGY IN THE BOUNDARY LAYER FOR 1700 cm Hg AND 3200 cm Hg.

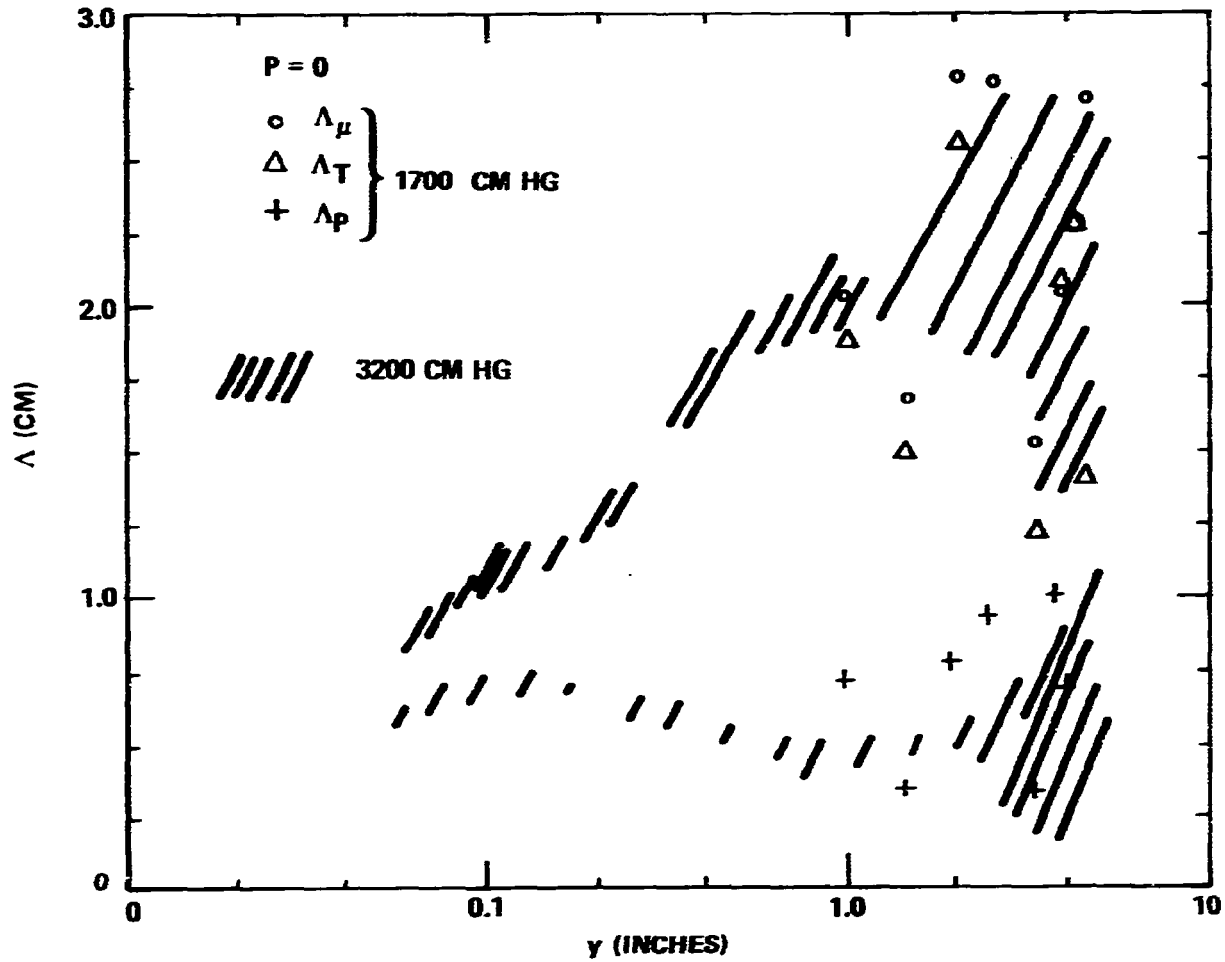

FIGURE 8. COMPARISON OF SCALE LENGTHS FOR THE 1700 cm AND 3200 cm CASE.

SECTION III

HYPERSONIC CONE BOUNDARY-LAYER EXPERIMENT

3.1 OBJECTIVE

The purpose of this experiment is to determine the mean and fluctuating characteristics of a hypersonic turbulent boundary-layer on a slender porous cone. The test was conducted at the Arnold Engineering and Development Center (AEDC), Von Karman Facility, using Tunnel-B at Mach 8. This experiment represents a joint effort between the General Electric Re-Entry and Environmental Systems Division and the Aeronutronic Division of Philco-Ford, originally with G.E. responsible for the mean-flow measurements and Philco-Ford for the fluctuation-flow measurements.

3.2 HOT-WIRE SURVIVAL TESTS

Since the AEDC Tunnel B represented a new environment for the Philco-Ford designed hot-wire probes, and because the flow conditions are more severe than those encountered in both the Philco-Ford SWT and the JPL/HWT, a series of tests to examine the survivability and endurance of the probes was carried out over the eight-month period prior to the first Philco-Ford entry. To accelerate the evaluation process, an instrumentation rake with provisions for mounting 8 probes was used, with each probe equipped with an individual current monitoring circuit. The output from each circuit was fed to a strip chart recorder in order to provide a complete time history of the probe during its exposure to the flow. Details of the rake and its operation are described in Reference 5. A photograph of the rake located in the free-stream flow of Tunnel B is shown in Figure 9.

An initial series of tests was carried out on a parasitic basis with the cooperation and assistance of ARO personnel during the period from January - March 1972. On the basis of these initial tests, which are described in Reference 5, it was concluded that:

(1) Survival time of the hot-wires, particularly the 0.000010 inch diameter probes, was too short to be of practical value for acquisition of turbulence data.

(2) Survivability improves with increasing wire diameter and decreasing aspect ratio.

(3) Shielding of the hot-wire is essential during tunnel start and during changes in stagnation pressure.

(4) The stagnation temperature must be maintained above the condensation threshold when the wire is exposed to the flow.

Based on these and subsequent test results it was decided to qualify all hot-wires in the Philco-Ford SWT prior to use in Tunnel B in order to eliminate

FIGURE 9. INSTRUMENTATION RAKE USED FOR HOT-WIRE SURVIVAL TESTS LOCATED IN FREE-STREAM OF AEDC TUNNEL B.

structurally weak probes. In addition, during the qualifying test, the probe output was monitored and those which exhibited erratic or abrupt variations in output signal were discarded.

A second series of survivability tests was carried out in May 1972 during the Phase I entry of the G.E/Philco-Ford experiment. The Phase I test, representing the first installation of the cone model in Tunnel B, was conducted by G.E. to check-out the test hardware and obtain preliminary mean-flow measurements. On the first hot-wire test, eight probes consisting of four 10 μinch, two 20 μinch and two 50 μinch diameter wires were installed in the tunnel,* and tested in the free-stream flow at supply pressures, P_o, of 200, 400, 600, and 850 psia. The supply pressure was initially established at 200 psia and after a suitable interval increased approximately 200 psia until a P_o of 850 psia was reached. At each P_o the supply temperature was maintained sufficiently high (760 - 890°F) to avoid condensation in the flow and during tunnel start and change in supply conditions the probes were retracted into the recess in the ceiling of the tunnel for protection. At a supply pressure of 200 and 400 psia all the wires survived exposure to the flow for a duration of approximately 45 minutes at each condition. With P_o = 600 psia, two 10 μinch and both 20 μinch diameter wires failed after 10-17 minutes, while the remaining wires survived for 64 minutes. The supply pressure was then increased to 850 psia, where the remaining 10 μinch wires failed after 4 to 19 minutes, while the 50 μinch wires survived for approximately one hour before failure occurred.

On a second hot-wire test, four 10 μinch and four 20 μinch diameter wires were installed in the tunnel and the test was conducted at a P_o of 850 psia. While the 10 μinch wires failed after durations ranging from 3 to 9 minutes, greater success was obtained with the 20 μinch wires, with one probe surviving for as long as 100 minutes. During this entry, heat transfer tests of the G.E. cone model were carried out and it was discovered that the model could be inserted into and retracted from the tunnel without causing either mechanical or electrical damage to the hot-wire probes. This finding was of practical importance for the conduct of the final tests since it minimized the precautions needed to protect the hot-wire probe during insertion of the cone model.

A final survivability test, conducted on a parasitic basis one week after the Phase I entry used four 10 μinch and four 50 μinch diameter wires. Two of the small wires were lost prior to the tunnel start, apparently due to burn-out caused by pickup of a transient voltage pulse, and one 50 μinch wire was lost when inserted into the flow. The remaining wires were successfully inserted into the flow on two occasions and survived a total of 70 minutes at tunnel supply conditions of 800 psia and 875°F. Although these wires were intact at the end of the test and survived retraction into the top recess of the tunnel, the two 10 μinch wires failed during or immediately following tunnel shut-down.

---

* Initial difficulties are best understood when one considers that the least delicate wires listed here, of 50 μinch diameter, generally represented the forefront of the state-of-the-art at the beginning of this work.

On the basis of these tests, summarized in Table I, the 10 μinch diameter wires, as well as the 20 and 50 μinch wires, demonstrated excellent survivability and endurance at a tunnel supply pressure of 400 psia, the lowest P_o of the final test matrix. On the other hand, at 850 psia, the highest P_o to be used in the final tests, only the 50 μinch wires showed acceptable survivability and endurance while the smaller wires indicated improved but still questionable performance. It was concluded, therefore, that the final turbulence measurements could be carried out using wires as small as 10 μ at the 400 psia condition and with 50 and possibly 20 μinch wires at 850 psia. In all cases it was considered desirable to restrict the aspect ratio of the wire to less than 200.

A final series of parasite tests of 10, 20 and 50 μinch diameter hot-wires was conducted in AEDC Tunnel B during the last week in July 1972. The tunnel was operated at Mach 8 with stagnation conditions of 800 psia and 875°F and with the probes located in the free-stream. The purpose of these tests was to determine experimentally the overheat current at which hot-wire failure occurred as a function of hot-wire diameter. The burn-out currents were converted to wire temperatures and indicated that burn-out occurred when the hot-wire was heated to 1000-1100°K. This result is slightly less than that observed during the JPL tests although the dynamic pressure, and consequently the structural load on the hot-wire, is larger in the AEDC facility. Consequently the observed burn-out currents were consistent with the JPL findings.

During this last test the hot-wire rake was modified to accommodate four total temperature probes of different construction which had been designed by G.E. Previous designs used by G.E. had been found to have recover factors significantly less than unity which increased the number of iterations required to find the true total temperature. The new T_o probes were tested, therefore, to determine the effect of probe geometry on its recovery factor characteristic. The tests were successful in clearly identifying a probe with superior characteristics, and on this basis, a T_o probe to be used by both Philco-Ford and G.E. during the final tests was selected.

3.3 FINAL EXPERIMENT DESIGN

3.3.1 TEST FACILITY

The present investigation was conducted at the Arnold Engineering Development Center (AEDC), Von Karman Facility, Tunnel B at Mach 8. This facility is a continuous flow, hypersonic wind tunnel with a 50-inch diameter test section. Interchangeable axisymmetric contoured nozzles provided flow at either Mach 6 or 8. The tunnel is a closed-circuit type which operates with air supplied by a central compressor system over stagnation pressures ranging from 50 to 850 psia. The corresponding flow conditions provide free-stream Reynolds numbers from 0.30×10^6 to 3.8×10^6 per foot at Mach 8 with a total temperature of 1350°F. The entire tunnel is cooled by integral, external water jackets. Complete specification[illegible] the facility are described in Reference 6, while the tunnel is shown sche[illegible]ly in Figure 10.

TABLE I

RESULTS OF HOT-WIRE ENDURANCE TESTS - MAY 18-23

Log of Time (in minutes) Exposed to Flow

WIRE NUMBER	WIRE DIAMETER (μinches)	ASPECT RATIO	SUPPLY PRESSURE, P_o, PSIA 200	400	600	850(a)	TOTAL TIME
23	50	220	45	48	64	60*	217
22	50	210	45	48	64	63*	210
15	20	190	45	48	17*		110
19	20	290	45	48	10*		103
9	10	180	45	48	64	19*	176
4	10	260	45	48	17*		110
6	10	280	45	48	64	4*	161
7	10	420	45	48	14*		107
3	10	265				3*	3
21	10	245				9*	9
10	10	220				6*	6
30	10	260				7*	7
17	20	215				4*	4
16	20	190				20*	20
28	20	260				58*	58
29	20	205				100*	100
11	10	285				+	
14	10	255				+	
13	10	175				70	70**
31	10	350				70	70**
24	50	180				70	70**
25	50	240				ǂ	
26	50	165				70	70**
27	50	155				70	70**

* Denotes time of failure after exposure at indicated P_o.

** Wire intact at end of test.

ǂ Lost during insertion into flow.

\+ Lost prior to tunnel start.

(a) P_o = 800 for last 8 wires.

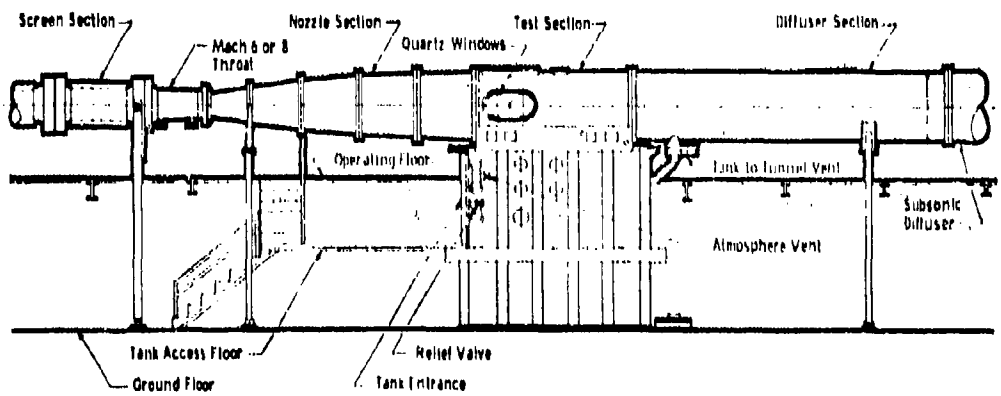

General Assembly, Tunnel B

FIGURE 10. SCHEMATIC OF AEDC TUNNEL B.

In order to provide quick access to the model without interrupting the tunnel operation, a vacuum sealed tank is located immediately below the test section Figure 10, into which the model and its support can be retracted. When the model is retracted the test section is sealed from the tank which can then be vented to atmosphere. After the tank entrance door is closed, the tank is vented to the test section pressure, the door between the tank and section is opened, and the model is injected into the airstream.

Because of a similar need to provide quick access to the hot-wire probe, it was necessary, prior to the fluctuation measurements, to construct a vacuum sealed tank into which the probe traversing mechanism could be retracted. This tank was located above the test section over an existing port used for observation and photography of the model (see Figure 10). The tank, shown in its operating position in Figure 11a, is raised approximately 6 feet above the top of the test section by means of an overhead hoist to permit access to the probe and its traversing and retraction mechanism, Figure 11b.

3.3.2 TEST HARDWARE

The model used in this investigation, which was supplied by G.E., is a 5° half-angle cone, 60 inches long (10.46 inch base diameter). It consists of an impervious sharp nose which is 10 inches long, and a porous frustum which is 50 inches long. The porous section of the model is subdivided into four independent compartments, each with separate gas supply tubes which are 1/4" O.D. stainless steel tubing. The forward two chambers each have one supply tube, the rear two chambers each have two supply tubes. A photograph of the model assembly located in the tank below the test section is shown in Figure 12.

The porous frustums of the model, which were fabricated at Mott Metallurgical Corp., Farmington, Conn., are made of 316 sintered stainless steel which is approximately 60% dense. The wall is approximately 1/4" thick. These porous elements are supported by a stainless steel substructure which contains all of the necessary internal plumbing and instrumentation routing ports. The cone is instrumented with 26 heat transfer gages and 34 pressure orifices, the locations of which are indicated in Figure 13. The surface heat transfer measurements were made with a copper-constantan Gardon type heat gage which provided an indication of both the heat transfer rate and the local surface temperature.

Calibration of both the gross porosity of each chamber of the model and of the local mass flux variation have been made at G.E. prior to the test program. These measurements indicate that the local variations do not exceed the ± 10% design specification. In addition, the gross porosity of each chamber was verified at AEDC before and after each entry, thereby indicating that the porosity of the chambers remained constant during the test. The gas metering systems provided by AEDC for each chamber were accurate to within several percent of the desired test condition.

A detailed description of the model and the surface instrumentation can be found in Reference 7.

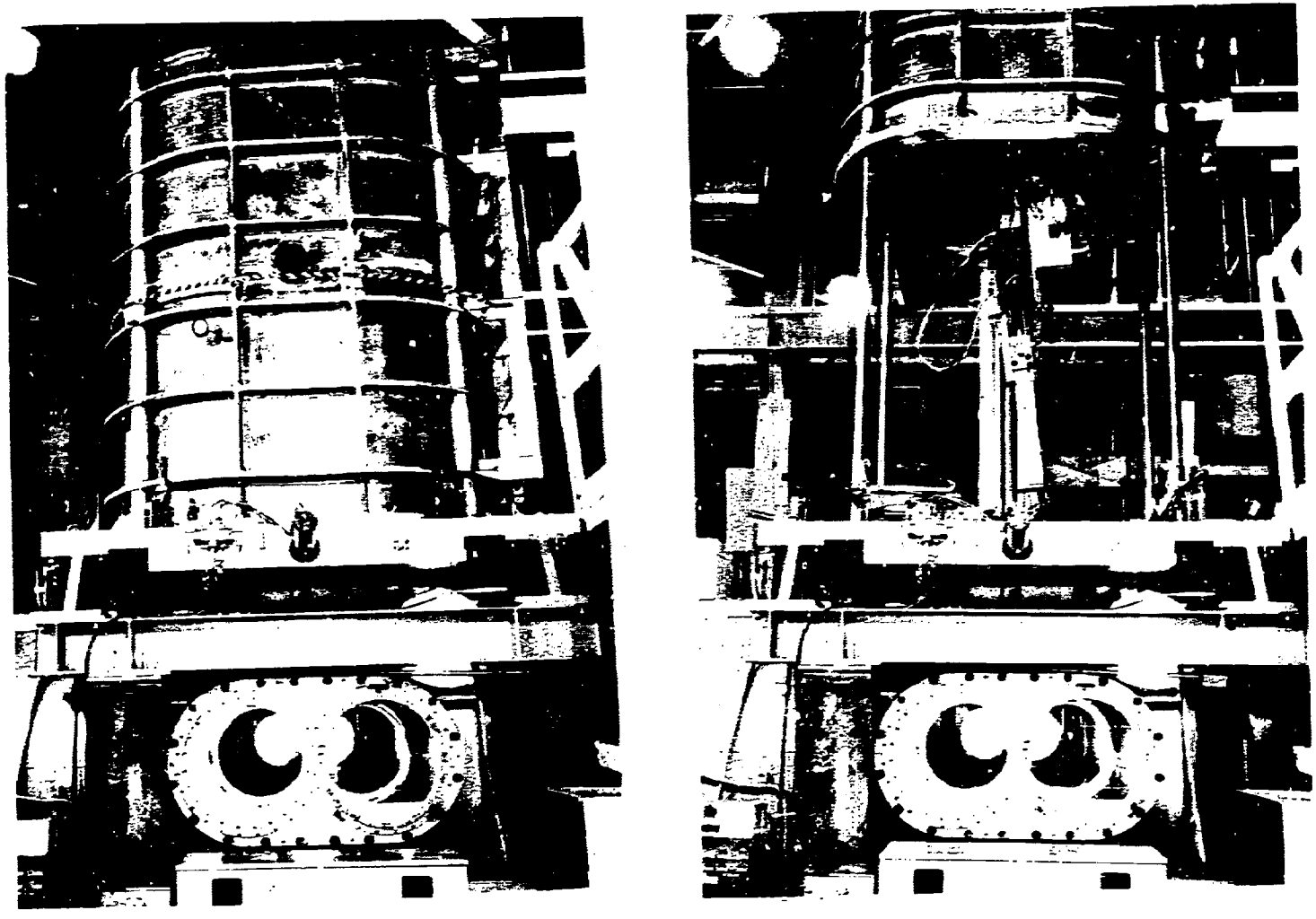

(a) OPERATING POSITION

(b) RAISED POSITION

FIGURE 11. VACUUM ENCLOSURE USED TO PROVIDE ACCESS TO HOT-WIRE

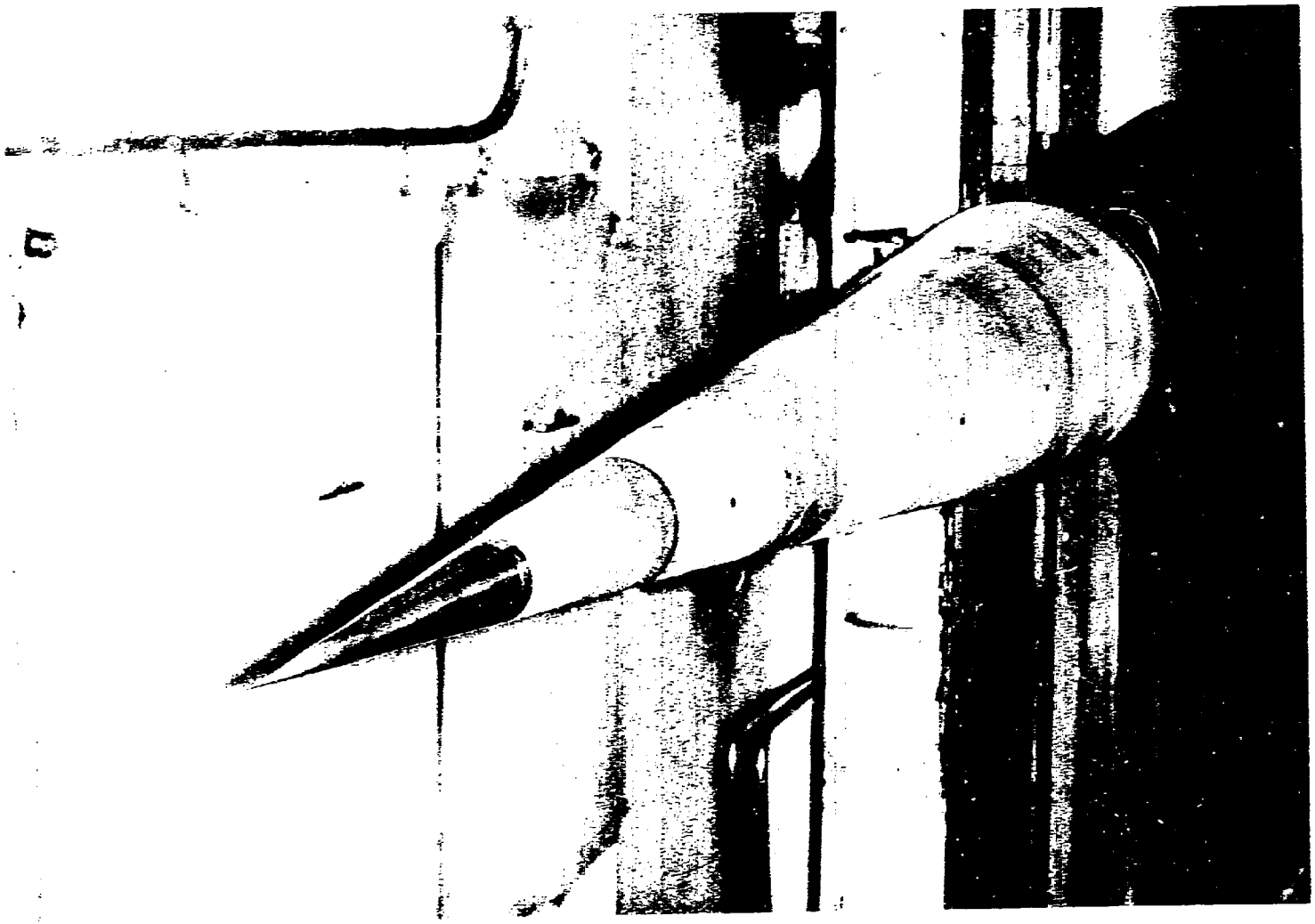

FIGURE 12. PHOTOGRAPH OF GE CONE MODEL LOCATED IN ACCESS TANK.

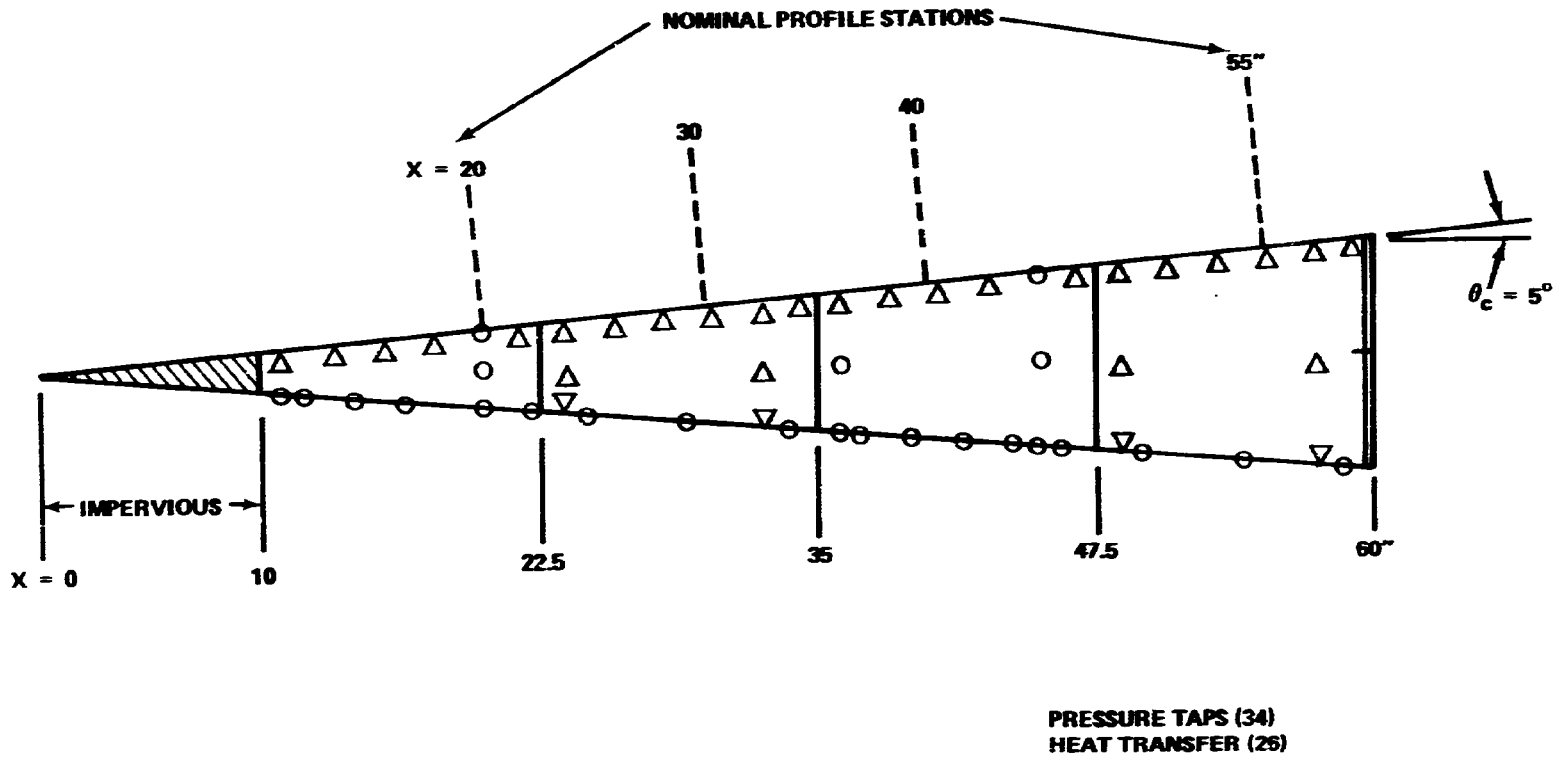

FIGURE 13. LOCATION OF CONE SURFACE PRESSURE AND TEMPERATURE GAUGES.

3.3.3 INSTRUMENTATION

Although G.E. was responsible for characterizing the mean boundary-layer flow, it was decided to make and tape-record mean-flow measurements during the Philco-Ford entry in order to provide:

(1) A check on the more detailed G.E. measurements, thereby verifying the constancy of the boundary-layer flow, and

(2) A complete permanent set of boundary-layer data at all conditions of the Philco-Ford test matrix.

The latter was particularly crucial since, in spite of initial intentions to carry out the mean and fluctuating flow measurements at identical test conditions, the final G.E. and Philco-Ford tests were in fact performed under different conditions.

a. Instrumentation Rake. The Philco-Ford instrumentation rake, shown in Figure 14, consisted of four 1/8 inch O.D. x 3 inch long stainless steel tubes aligned in a row and silver soldered to each other and to a single wedge shaped sting which mounted to the AEDC probe traversing mechanism. The probes were installed on the rake by insertion through the 1/8 inch diameter tubes, with a pitot probe and total temperature probe occupying the outboard positions and a hot-wire probe and surface sense probe located in the inboard positions. The probes were aligned with their sensing tips essentially the same distance from the cone tip, but with the pitot, total temperature and hot-wire probes displaced from 0.005 to 0.040 inches vertically above the surface sensor in order to avoid contact with the cone surface. The lateral and vertical displacement of each probe (relative to the surface sense probe) and the effect of surface curvature were taken into account to convert the indicated probe position into its true height above the surface along a line passing through the center of the cone. This procedure is described in Appendix A.

b. Probe Design. The hot-wire anemometer consisted of a Pt-10% Rh wire mounted across the tips of two sharp-pointed prongs and bonded to the supports with a commercial gold paint. For the present experiments wires of 10, 20 and 50 μinch diameter were used and during the week prior to the test approximately one dozen probes of each size were fabricated. The wires were mounted with sufficient slack to eliminate spurious signals due to "strain gage" effects and the wire aspect ratio was restricted to the range from 150 to 250.

The probe body consisted of a 3/32 inch diameter x 1-1/4 inch long alumina cylinder cemented at one end to a 1/32 inch diameter x 1/4 inch long alumina cylinder used to support the hot-wire prongs. Both cylinders were provided with two holes along their length through which the hot-wire leads were inserted. The leads were 30 gage copper wire encased in high temperature fiberglass insulation. Three-mil nickel wire, used for the hot-wire prongs, was silver-soldered to one end of the copper leads. The prongs, leads, and alumina tubes were held together with Corning Glass Company Pyroceram cement. Details of the probe construction are presented in Reference 8. A photograph of the assembled probe is shown in Figure [illegible] an enlargement of the probe tip, showing a 20 μinch diameter wire mounted on the prongs, is presented in Figure 15b.

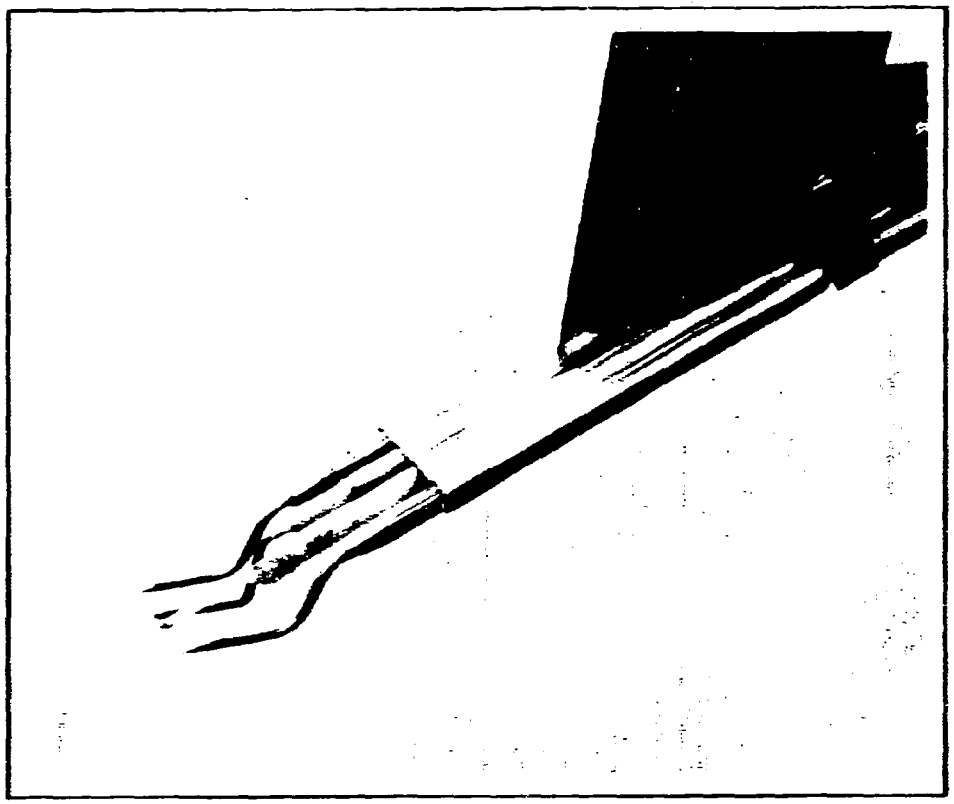

FIGURE 14. PHILCO-FORD INSTRUMENTATION RAKE WITH PROBES INSTALLED. FROM FRONT TO BACK: PITOT PROBE, HOT-WIRE, SURFACE SENSOR, TOTAL TEMPERATURE PROBE.

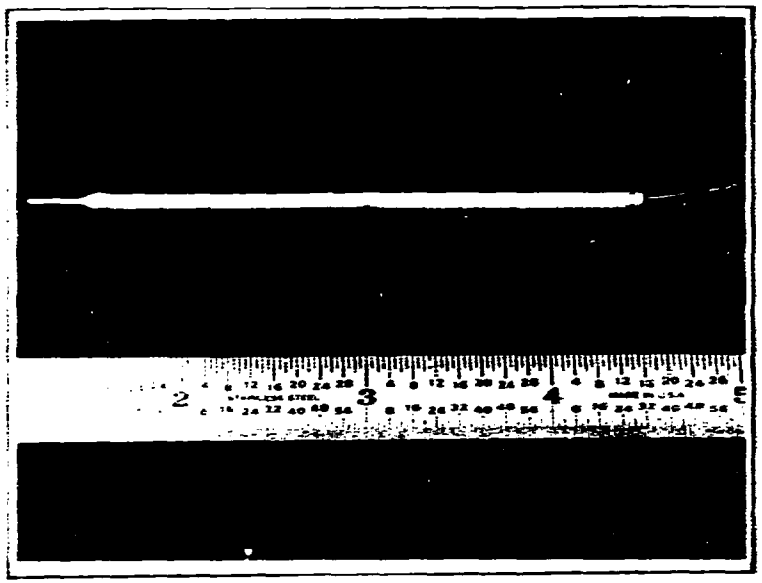

a) ASSEMBLED PROBE

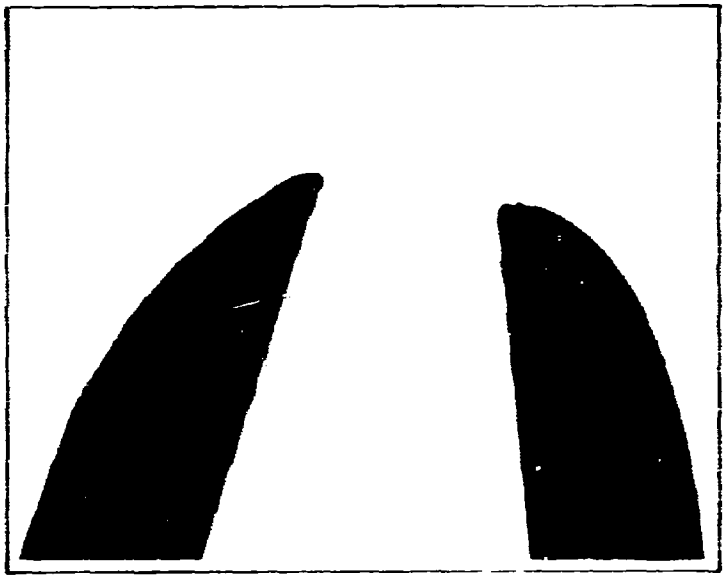

b) 300X MAGNIFICATION OF TIP SHOWING 0.00002 INCH DIAMETER PT-% RH WIRE MOUNTED ON 3 MIL NI PRONGS

FIGURE 15. HOT-WIRE ANEMOMETER.

After the probe was assembled and qualified in the Philco-Ford SWT, the hot-wire was oven calibrated to determine its temperature-resistance characteristics. Following the oven calibration, the wire resistance was checked daily prior to its use in Tunnel B to ensure that the wire characteristics remained unchanged.

The total temperature probe consisted of a chromel-alumel thermocouple, sheathed within a 0.020 inch O.D. stainless steel tube, which was inserted within a 0.030 inch O.D. tube for rigidity. The 0.030 inch tube in turn was silver soldered within a 0.093 inch O.D. tube for insertion into the rake. The sensing end of the probe was shielded by a 0.050 inch O.D. tube as shown in Figure 16.

The pitot probe was constructed in a similar fashion with a 0.030 inch O.D. tube transitioning to a 0.093 inch O.D. tube for installation in the instrumentation rake. The sensing end of this probe was flattened to an outside height of 0.020 inches as indicated in Figure 16.

Finally, the surface sense probe, also shown in Figure 16, consisted of a 0.015 inch diameter hardened steel wire held in place with Sauereisan cement, to provide electrical isolation, within a 0.093 inch O.D. tube. The sense probe was connected in series with a low voltage battery and a lamp, which was turned on when the probe contacted the cone to complete the circuit.

c. Probe Traverse Mechanism. The probe traversing mechanism constructed for the fluctuating flow measurements was designed to permit retraction out of the flow and allow access to the probes without interrupting the tunnel operation. In addition, the traverse mechanism provided for remote drive in the direction parallel to the tunnel axis (x) and in the direction normal to the cone surface (y). The axial location of the probes was defined by locating the sense probe adjacent to the cone at the junction between two chambers to establish an x reference immediately after inserting the probes into the flow. The probe could then be located at a desired x station by driving the traverse mechanism in the required distance from the known reference position. The axial station could be determined within an accuracy of ± 0.05 inches and a repeatability of ± 0.10 inches. The vertical height above the model was determined by driving the probe toward the cone surface and establishing a y = 0 position with the surface sense probe. All boundary-layer surveys were made driving away from the surface after the y = 0 location was identified. The y station could be determined within ± 0.001 inches and was repeatable within ± 0.005 inches.

In order to protect the hot-wire probe during insertion into the tunnel, change of tunnel conditions, etc., the traverse mechanism was provided with a pneumatically actuated shield which covered the entire front portion of the instrumentation rake. Figure 17 shows the probe traverse mechanism located atop the tunnel test section with the shield in both its lowered and raised positions. Figure 18 shows the probes located within the cone boundary-layer and indicates the clearance between the cone and the shield when the latter is in its retracted position.

3.3.4 TEST PROCEDURE

a. Test Matrix. Several discrete entries in Tunnel B were required for completion of both the mean and fluctuating flow measurements. The measurements were carried out in accordance with the following schedule:

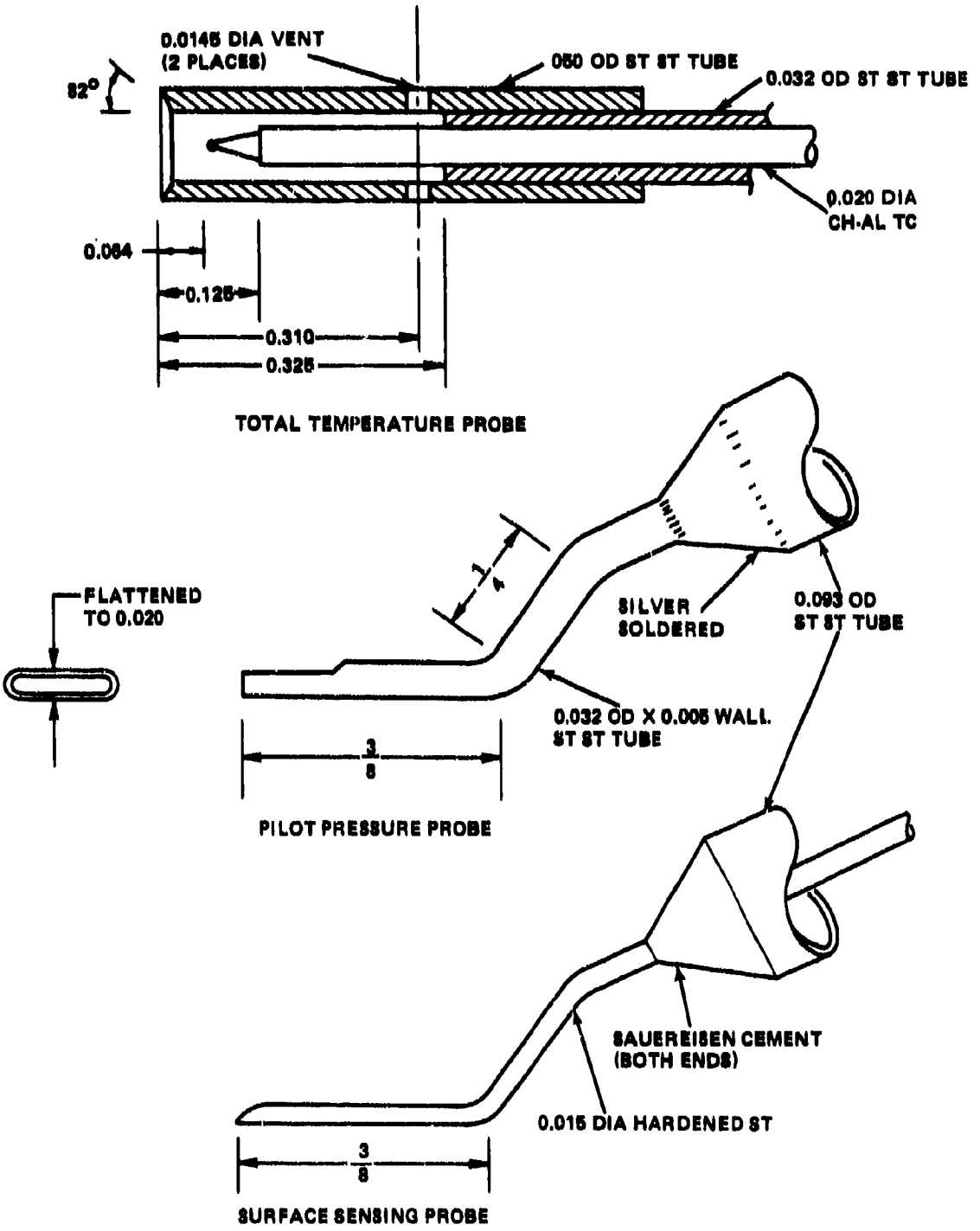

FIGURE 16. DETAILS OF MEAN FLOW PROBES.

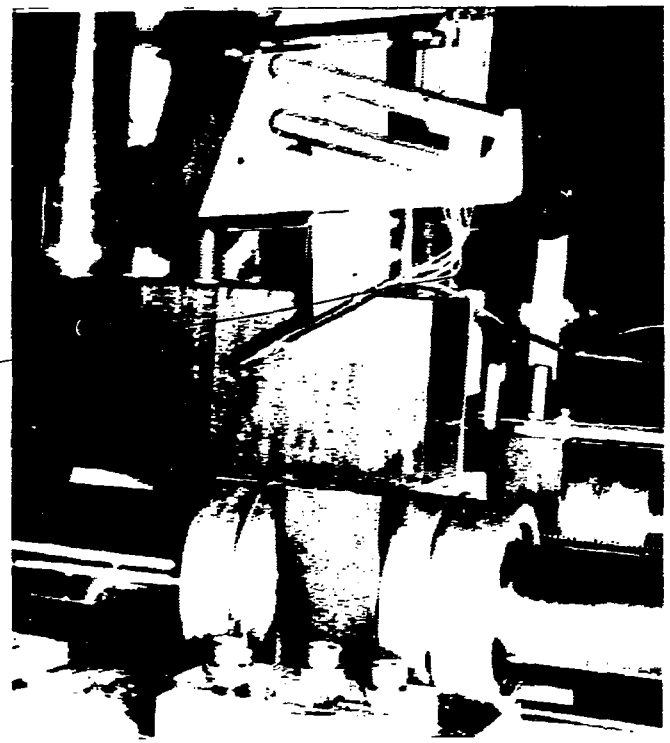

SHIELD UP

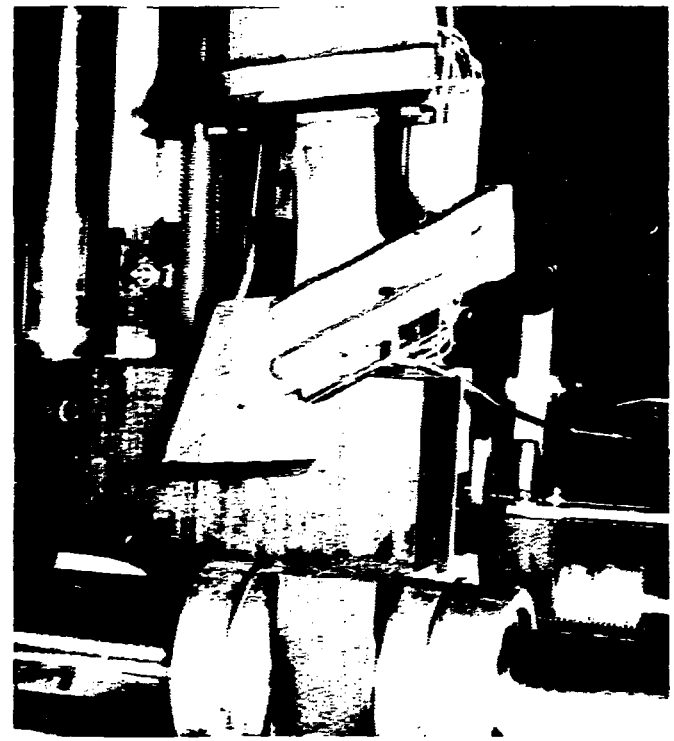

SHIELD DOWN

FIGURE 17. PHOTOGRAPH OF PROBE TRAVERSING MECHANISM LOCATED ON TOP OF TEST SECTION SHOWING HOT-WIRE SHIELD IN RAISED AND LOWERED POSITIONS.

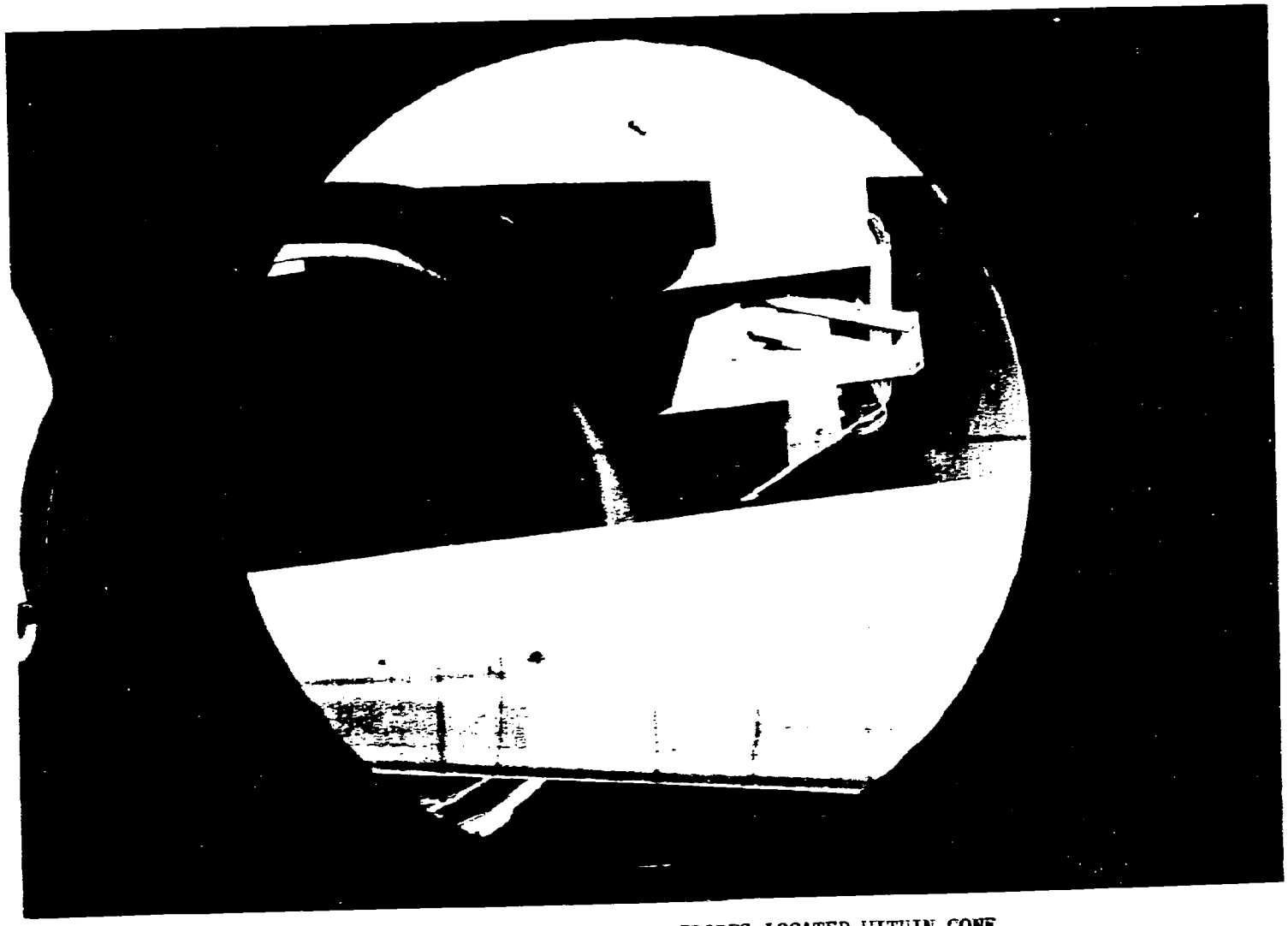

FIGURE 18. PHOTOGRAPH OF PHILCO-FORD PROBES LOCATED WITHIN CONE BOUNDARY LAYER AT $x \approx 37$ INCH STATION.

ENTRY	PURPOSE
Phase I	Heat transfer measurements, hardware check-out and hot-wire survivability.
Phase II	Mean flow profiles.
Phase III	Fluctuating flow and mean flow profiles.
Phase IV	Fluctuating flow and mean flow profiles.

Originally the turbulence measurements were to be carried out for the conditions listed in Table II, which corresponded to the baseline conditions of the G.E. mean flow measurements. However, because of difficulties encountered with the hot-wire at 850 psia, this condition was relaxed and final tests performed at 600 psia. The completed test matrix is summarized in Table III. Since the G.E. program was carried out only at 850 psia (omitting the originally planned 350 psia tests), the mean flow data acquired by Philco-Ford during the hot-wire tests represents a necessary ingredient for the successful completion of this task.

b. Measurement Techniques. Although the mean flow measurements, probe positions, and tunnel conditions were recorded and processed by the AEDC Data Acquisition System, the probe data was also tape-recorded by Philco-Ford in order to provide, with the hot-wire measurements, a complete magnetic tape data file. Block diagrams of the Philco-Ford data recording schemes are shown in Figures 19 and 20. These schemes, called configurations A and B, differ only in the manner in which the hot-wire signal was processed. In both cases the pitot pressure, total temperature and surface sense probe positions were monitored by DVM's and converted to frequency signals for tape recording by the Honeywell 7620 recorder. The hot-wire current and mean voltage were also monitored by DVM's and the latter converted to a frequency signal for tape recording.

The fluctuating voltage output from the hot-wire was monitored by a Hewlett-Packard wave analyzer and Tektronix Oscilloscope in order to observe the frequency content and quality of the signal. With configuration A the signal was then directly recorded, while with configuration B the signal was fed to an RMS meter and converted into a wideband signal prior to tape recording.* The purpose of the two recording schemes is described below.

---

* The hot-wire amplifier was operated typically at a high frequency cut-off of 500 kHz. Since the FM channel cuts off at 400 kHz when the recorder is operated at 120 ips, the signal was also recorded on a direct channel which extends to 1.5 MHz. Thus, although, the direct recording is of poorer quality than the FM recording, this procedure allows the complete amplifier output to be recorded.

TABLE II

ORIGINAL TEST MATRIX FOR TURBULENCE MEASUREMENTS

AEDC CONE TESTS

Free stream Mach Number	8
Angle of Attack	0
Nose Radius	0
Wall temperature	Equilibrium
Cone Half Angle	5 degrees

CASE NO.	TUNNEL STAG. PRESS. (psia)	$Re_\infty/Ft \times 10^{-6}$	INJECT GAS	BLOWING RATE $= \frac{(\rho v)_w}{(\rho u)_e}$		NOMINAL AXIAL STATION, (in)			
				0	0.0015	20	30	40	55
PF1	850	3.7	-	X		X	X	X	X
PF2	850	3.7	Air		X	X	X	X	X
PF3	350	1.7	-	X		X	X	X	X
PF4	350	1.7	Air		X	X	X	X	X

TABLE III

FINAL TEST MATRIX FOR TURBULENCE MEASUREMENTS

AEDC CONE TESTS

Free Stream Mach Number	8
Angle of Attack	0
Nose Radius	0
Wall Temperature	Equilibrium
Cone Half Angle	5 degrees

CASE NO.	TUNNEL STAG. PRESS. (psia)	$Re_\infty/Ft \times 10^{-6}$	INJECT GAS	BLOWING RATE $= \frac{(\rho v)_w}{(\rho u)_e}$		NOMINAL AXIAL STATION, (in)			
				0	0.0015	20	30	40	55
PF3	350	1.7	-	X		X	X	X	X
PF4	350	1.7	Air		X	X	X	X	X
PF5	600	2.6	-	X		X	X	X	X
PF6	600	2.6	Air		x	X	X	X	X

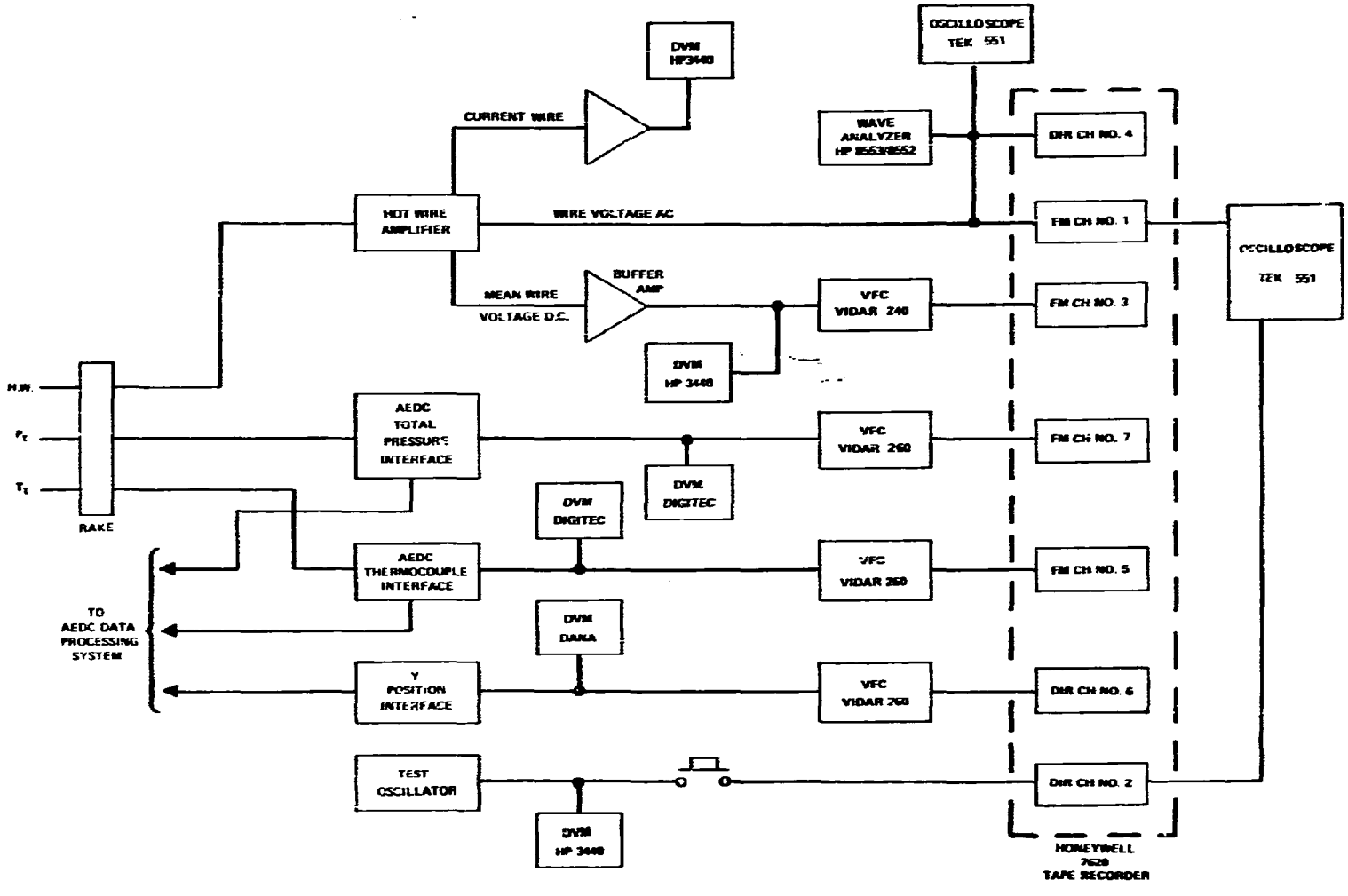

FIGURE 19. BLOCK DIAGRAM OF TURBULENCE MEASUREMENT INSTRUMENTATION IN CONFIGURATION A.

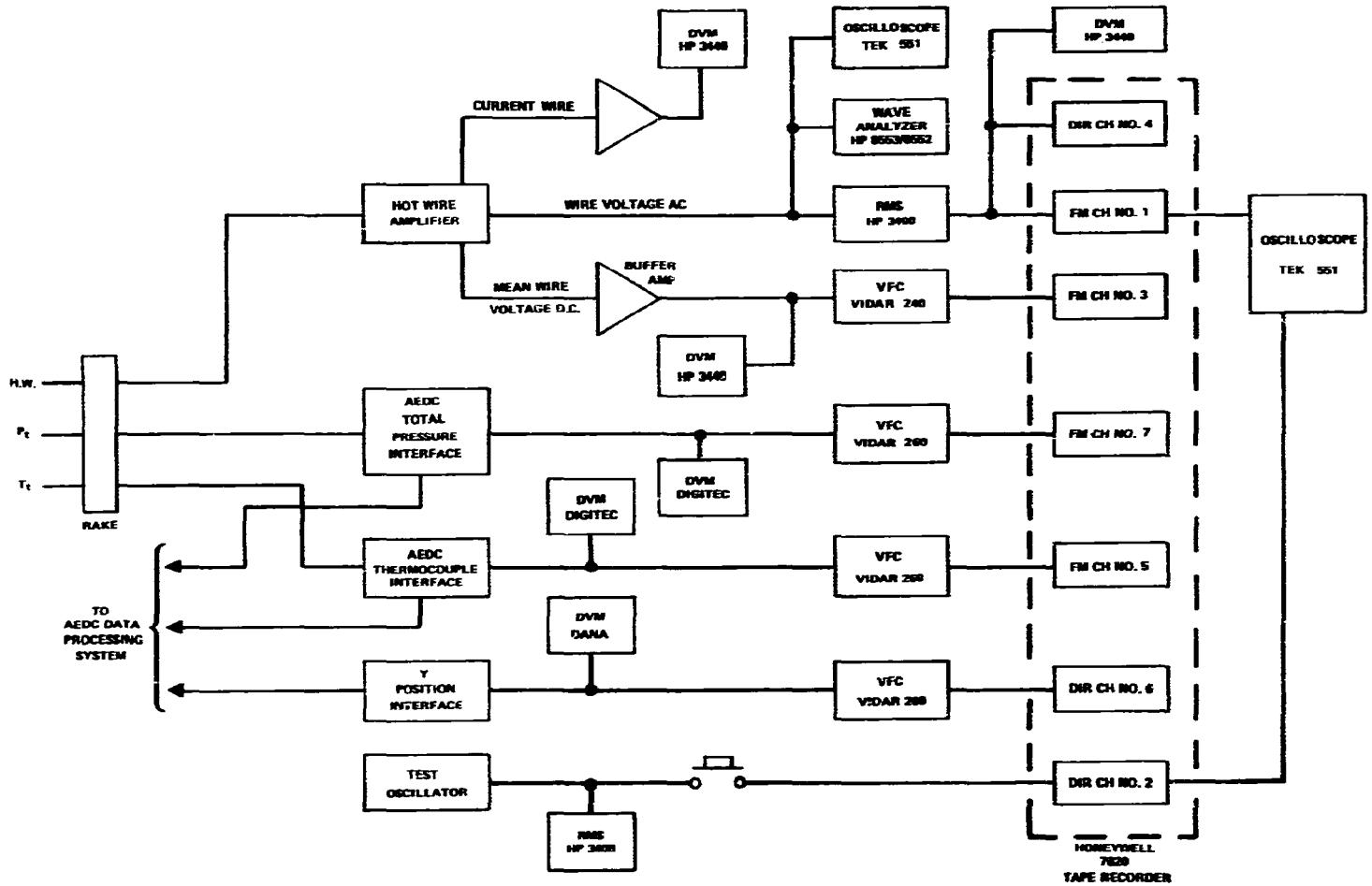

FIGURE 20. BLOCK DIAGRAM OF TURBULENCE MEASUREMENT INSTRUMENTATION IN CONFIGURATION B.

Prior to the Phase III tests, it was decided to cover that part of the test matrix which ensured maximum survivability of the hot-wires. For this reason, the "safest" combination of wire diameters (0.00005inches) and tunnel pressures (P_0 = 350 psia) were used. For this same reason, it was also decided to initially operate the wires using configuration B. This configuration involves traversing the hot-wire across the boundary-layer continuously at constant current and recording at 7½ ips, so that the wideband fluctuation intensity distribution with vertical distance could be extracted from the data. With configuration A, the preferred recording scheme, the hot-wire is located at several pre-selected distances above the surface and its output recorded at 120 ips as the heating current is changed in discrete steps. The latter has the advantage over configuration B in that it can yield spectral information and thus more accurate fluctuation data; but, on the other hand, it involves greater risk than configuration B because it takes data at a slower rate.

This approach was initiated during the Phase III tests. It was further planned that when data acquisition using configuration B was completed for a given test condition, the test would be repeated using configuration A in order to provide the more accurate fluctuation data. However, for reasons discussed later, little quantity information was collected during the Phase III entry. In addition, on the basis of the experience acquired with the hot-wires during this entry, it was believed that the wires would survive for significant periods of time. Therefore, configuration B was deleted for the Phase IV tests, and the test matrix outlined in Table III was completed using configuration A. Figure 21 shows the layout of the Philco-Ford electronics located just downstream of the tunnel test section.

3.4 TEST RESULTS

3.4.1 PHASE III TESTS

A summary of the Phase III tests is shown in Table IV. Because of the indicated difficulties, quantitative data was acquired only at the PF3 condition. The TVA shutdowns, caused by electrical power shortages in the AEDC area due to prevailing weather conditions, were particularly serious. Since the tunnel shift started at 9:00 a.m., and approximately 3 hours were required to bring the tunnel to test condition, equilibrate the model, and prepare the hot-wire for data taking, the early afternoon shutdowns precluded the acquisition of any quantitative data during the last three days of this entry.

The difficulties encountered with the probe actuator and its vacuum enclosure were not unexpected since this device had not been operated with air-on prior to the Phase III test. Although the problems associated with the actuator were eventually corrected, the lost time slowed the progress of the tests. It should be pointed out, however, that the experience acquired with the actuator during this entry led to essentially trouble-free operation during the Phase IV entry.

The data collected at the PF3 condition was of relatively poor quality. In particular, the hot-wire signal was obscured by a large noise signal which would appear suddenly as high amplitude "bursts" or spikes. It was originally suggested that the noisy signal was caused by vibration of the hot-wire probe or by variations

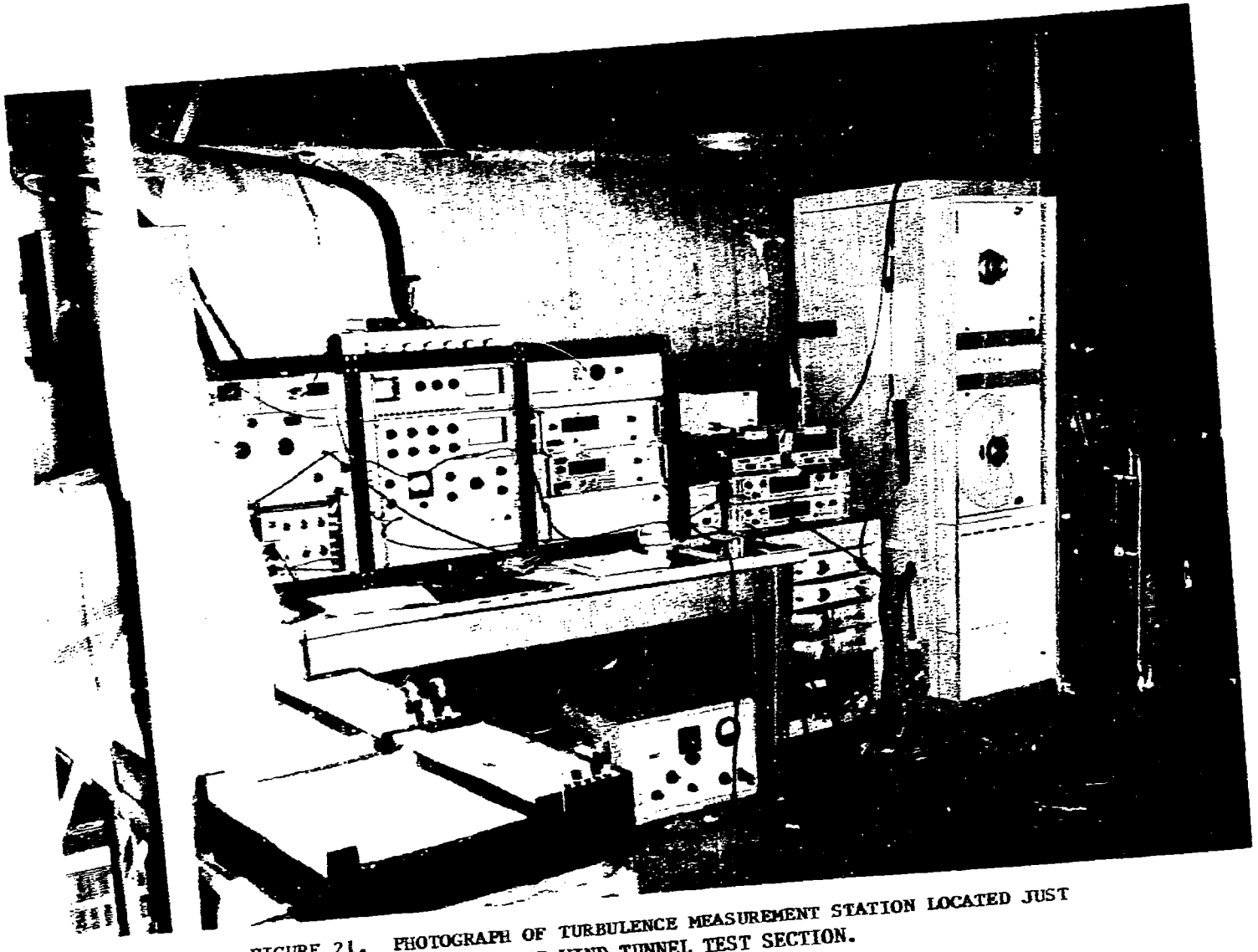

FIGURE 21. PHOTOGRAPH OF TURBULENCE MEASUREMENT STATION LOCATED JUST DOWNSTREAM OF WIND TUNNEL TEST SECTION.

TABLE IV

AEDC CONE BOUNDARY-LAYER EXPERIMENT

DATE	NO.	HOT-WIRE DIAMETER (μinch)	COMMENT	DATA ACQUIRED
9/7	58 54	50 50	Difficulty with evacuating can.	(1) Continuous rms traverse at 3 currents at pF 3, x = 39. (2) Continuous p_T, T_T traverse at pF 3, x = 29, 39. (3) Shadowgraph at pF 3.
9/8	53 55	50 50	Difficulty with shield actuation.	(1) Continuous rms traverse at fixed current for pF 2, 3, 4 and x = 19, 29, 39. (2) Model survey at pF 2, 3, 4.
9/11	61 60 57	50 50 50		Hot-Wire Flow calibrations.
9/12	59	50	TVA shutdown at 3:30	(1) Flow calibration. (2) Fluctuation measurements at pF 3, x = 19, 29, 39. (3) Model survey at pF 3.
9/13	59	50	TVA shutdown at 2:00	(1) Mean flow boundary-layer traverse at pF 3, x = 19, 29, 39. (2) Model survey at pF 3. (3) Shadowgraphs at pF 4.
9/14	59 56 52	50 50 50	TVA shutdown at 1:20	Hot-wire flow calibration
9/15	52 63 62 46	50 20 20 20	Wire failures due to shield actuation	(1) Hot-wire flow calibrations. (2) Shadowgraphs at pF 4.

in the flow associated with streamwise shifting of the transition region. During the Phase IV entry the noisy signal was traced to a defective or dirty switch and a short length of unshielded cable. Measurements at the PF3 condition were repeated, therefore, during the Phase IV tests. However, in order to obtain an estimate of the fluctuation intensities, the PF3 uncorrected wideband data at the x = 29 inch station, where the signal was relatively well-behaved, was subjected to a modal analysis which indicated peak temperature fluctuations of approximately 30%. During the analysis it was found that the hot-wire was operated over a very limited range of overheat currents which introduced large uncertainties in the results. Nevertheless, the result was consistent with those of Kistler (Reference 9) extrapolated to the present test condition, and of Fischer, et al. (Reference 10) obtained in adiabatic helium flows at Mach 20, and later justified by the measurements made during the Phase IV entry.

In addition to the above data, a considerable amount of information was obtained in the form of shadowgraph photographs and qualitative hot-wire traverses. This latter information, which was extremely helpful in planning the Phase IV entry, was used to:

(1) Establish the relative nature of the boundary-layer flow as a function of Reynolds number, blowing rate, and x-station.

(2) Delineate regions of transition flow.

(3) Define the boundary-layer thickness and its x-dependence as a function of test conditions.

(4) Indicate the relative effect of blowing on the boundary-layer flow.

(5) Provide an indication of turbulent activity across the boundary-layer.

Shadowgraphs of the flow over the cone at a free-stream Reynolds number of 1.7 x 10^6/ft are shown in Figure 22 for blowing rates of λ = 0 and 0.0015. The left-hand window shows the forward portion of the cone extending over the region from x = 4 inches to x = 21 inches while the right-hand window indicates the region from x = 29 to x = 41 inches. The grid spacing in Figure 22 is 4½ inches with the left-hand vertical grid line located at x = 29.2 inches and the right-hand vertical grid line at x = 38.2 inches. With λ = 0 a laminar-like boundary flow extends to an x-station in excess of 30 inches. With blowing the boundary thickens by a factor of 2 or 3 with the transition zone shifting forward 6-8 inches. In both cases a high-frequency wave structure which was also detected by the hot-wire is apparent at the outer edge of the layer in the region of laminar flow. A similar structure has been observed by several other investigators (References 11 and 12), although neither its origin nor its effect on transition has been identified. The scale of the wavefront is about twice the boundary-layer thickness so that the corresponding frequency can be given approximately by $u/2\delta$, which is in agreement with other findings. The present hot-wire measurements reveal the additional fact that the wavefront gives rise to strong localized fluctuations which are similar in magnitude to the peak fluctuation intensities observed in the turbulent portion of the boundary-layer.

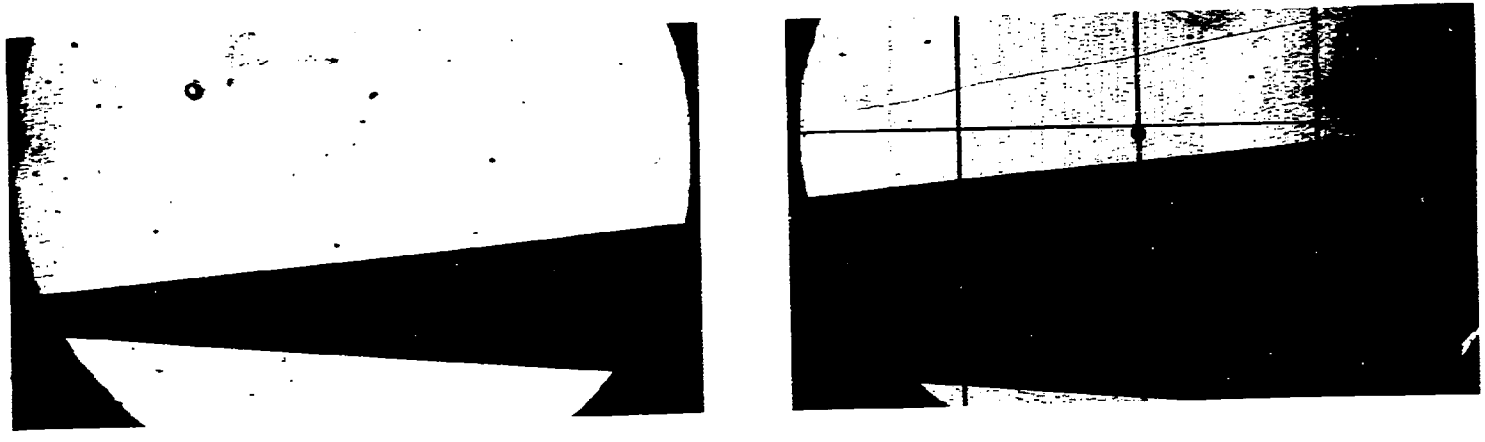

$Re_{\infty}/FT = 1.7 \times 10^6$, $\lambda = 0.0015$

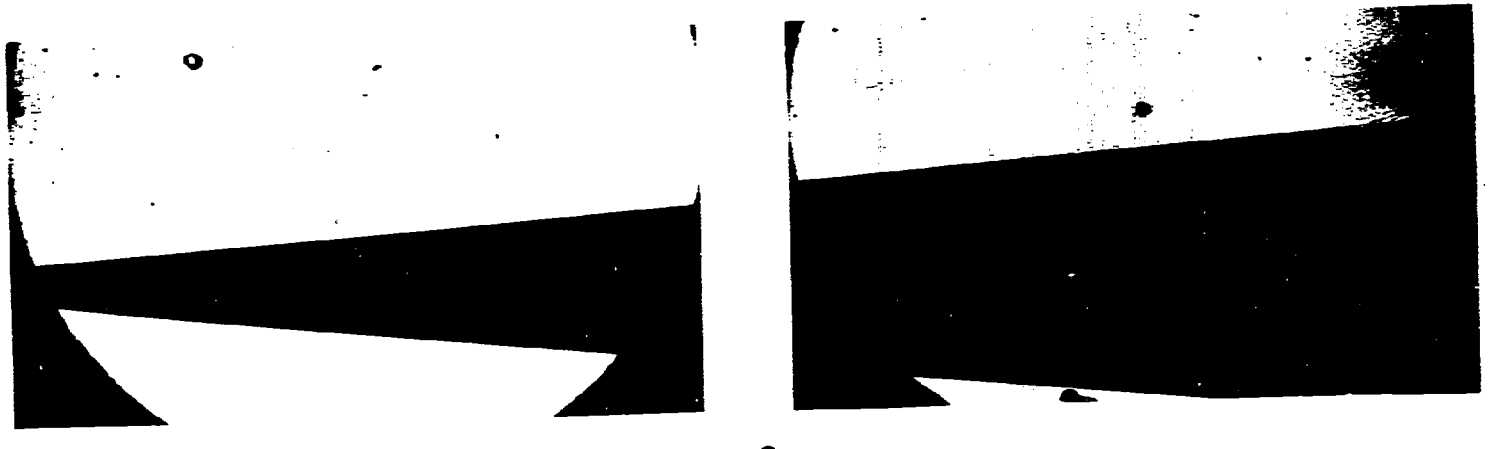

$Re_{\infty}/FT = 1.7 \times 10^6$, NO BLOWING

FIGURE 22. SHADOWGRAPH OF CONE BOUNDARY LAYER FOR $Re/ft = 1.7 \times 10^6$ and $P_o = 350$ psi. (A) $\lambda = 0$, (B) $\lambda = 0.0015$.

In order to provide a complete picture of the relative nature of the boundary-layer flow as a function of test condition, shadowgraphs obtained during the Phase IV entry are included here. Shadowgraphs obtained at a free-stream Reynolds number of 2.6×10^6/ft (P_o = 600 psia) and shown in Figure 23 for $\lambda = 0$ and $\lambda = 0.0015$, while those obtained at a Reynolds number of 3.7×10^6/ft (P_o = 850 psia) for the same blowing rates are shown in Figure 24. These photographs reveal similar features as those observed at the low Reynolds number condition and indicate, in addition, a thinning of the boundary-layer and a forward shift of the transition region as the Reynolds number is increased. Furthermore the high-frequency wave structure occurring at the edge of the laminar boundary-layer persists over the entire Reynolds number range.

The relative effect of the free-stream Reynolds number and blowing and the boundary-layer turbulence is indicated in Figure 25 which shows continuous traces of the rms hot-wire output obtained at x = 29 inches for a constant moderate overheat current and several test conditions. At a Reynolds number of 1.7×10^6/ft the boundary-layer flow at x = 29 inches is laminar and the hot-wire signal is localized at the outer edge of the layer in the vicinity of the high-frequency wave structure observed in the shadowgraphs. There is no apparent turbulent activity within the layer where the hot-wire signal drops to its free-stream value. At a blowing rate of $\lambda = 0.0015$, the boundary layer remains laminar but is appreciably thickened and, according to pitot pressure measurements, moved physically away from the cone. Again the peak hot-wire signal is localized at the edge of the boundary-layer and there is no apparent "turbulence" within the layer, particularly near the wall. When the free-stream Reynolds number is increased to 3.7×10^6/ft, the boundary-layer, with $\lambda = 0.0015$, is now fully turbulent. The peak hot-wire signal occurs at approximately the mid-point of the boundary-layer and fluctuations persist to the cone surface where the raw wire output is still well above its free-stream level.

3.4.2 PHASE IV TESTS

The Phase IV Philco-Ford entry in Tunnel B was successfully completed with quantitative boundary-layer turbulence surveys made at all of the conditions listed in Table III except the x = 55 inch station for PF6. A 50 micro-inch diameter hot-wire was used for the measurements at 350 psia with x stations of 19, 29 and 39 inches. All other turbulence measurements were made using a 20 μinch diameter wire. After the difficulties causing the "noisy" hot-wire signals described in Section 3.4.1 were corrected, the noise was reduced to a low level and signal quality was significantly improved.

Although it was originally intended to carry out the initial tests of this entry at 850 psia, excessive hot-wire breakage was encountered at this condition. Consequently, the maximum tunnel pressure was restricted to 600 psia which, nevertheless, should provide data at the rearward x stations that is representative of highly developed turbulent boundary-layers. It is now believed that the unusually high failure rate can be attributed to the semi-annual two-week down-time which preceded the test entry. During this period the nozzle was recoated and the interior of the test section was cleaned and repainted. Since the tunnel was not operated prior to the test entry, there was no opportunity to eliminate the particulate material which accumulated during the down-time or was eroded

$Re_{\infty}/FT = 2.6 \times 10^6$, $\lambda = 0.0015$

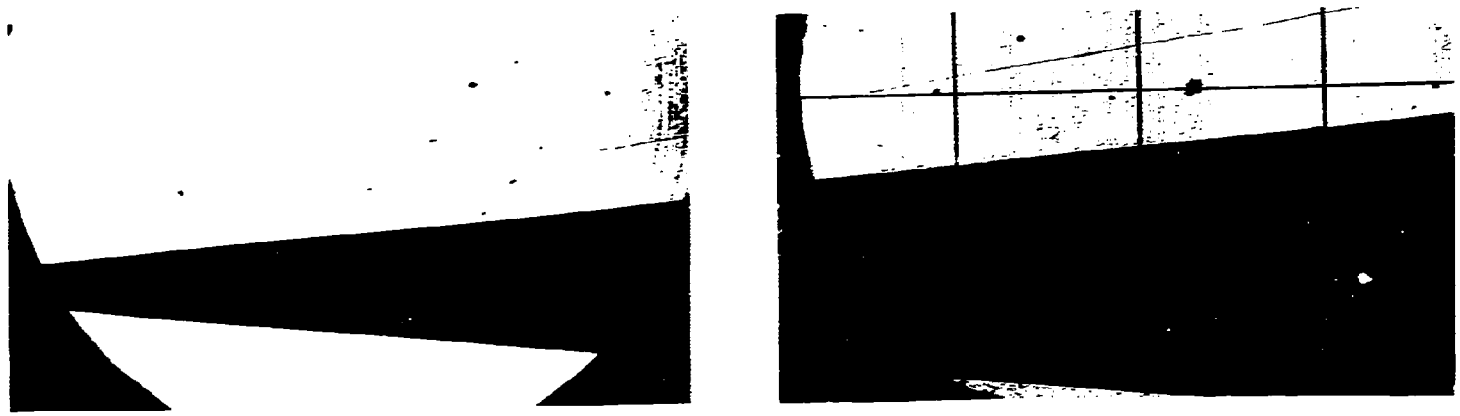

$Re_{\infty}/FT = 2.6 \times 10^6$, $\lambda = 0$

FIGURE 23. SHADOWGRAPH OF CONE BOUNDARY LAYER FOR Re/ft = 2.6×10^6 AND P_o = 600 psi. (A) $\lambda = 0$, (B) $\lambda = 0.0015$.

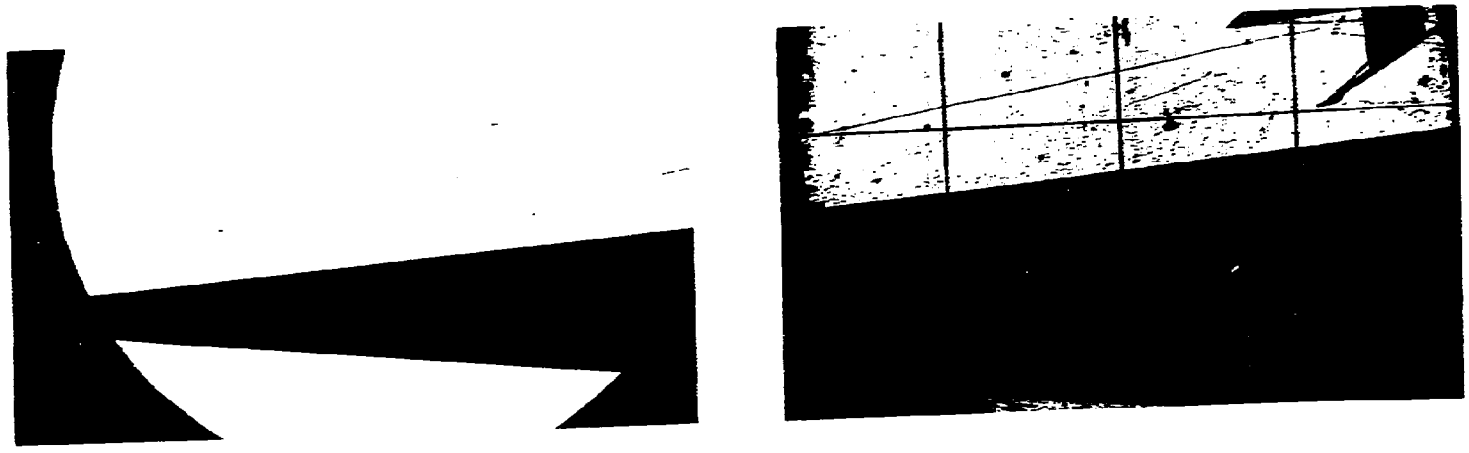

$Re_{\infty}/FT = 3.7 \times 10^6$, $\lambda = 0.0015$

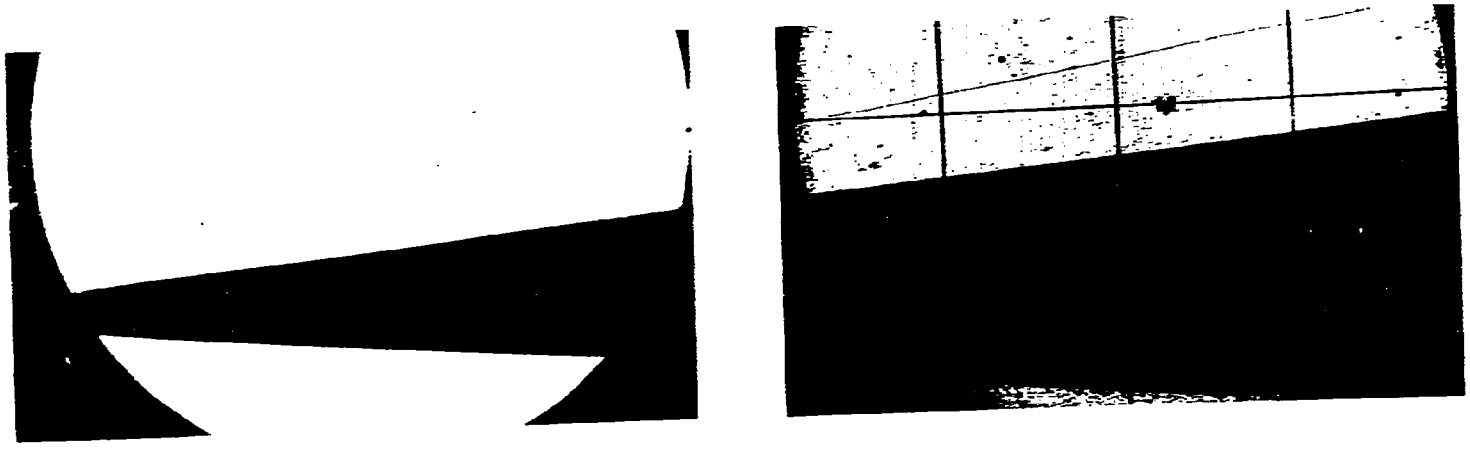

$Re_{\infty}/FT = 3.7 \times 10^6$, $\lambda = 0$

FIGURE 24. SHADOWGRAPH OF CONE BOUNDARY LAYER FOR Re/ft = 3.7×10^6 AND P_o = 850 psi. (A) λ = 0, (B) λ = 0.0015.

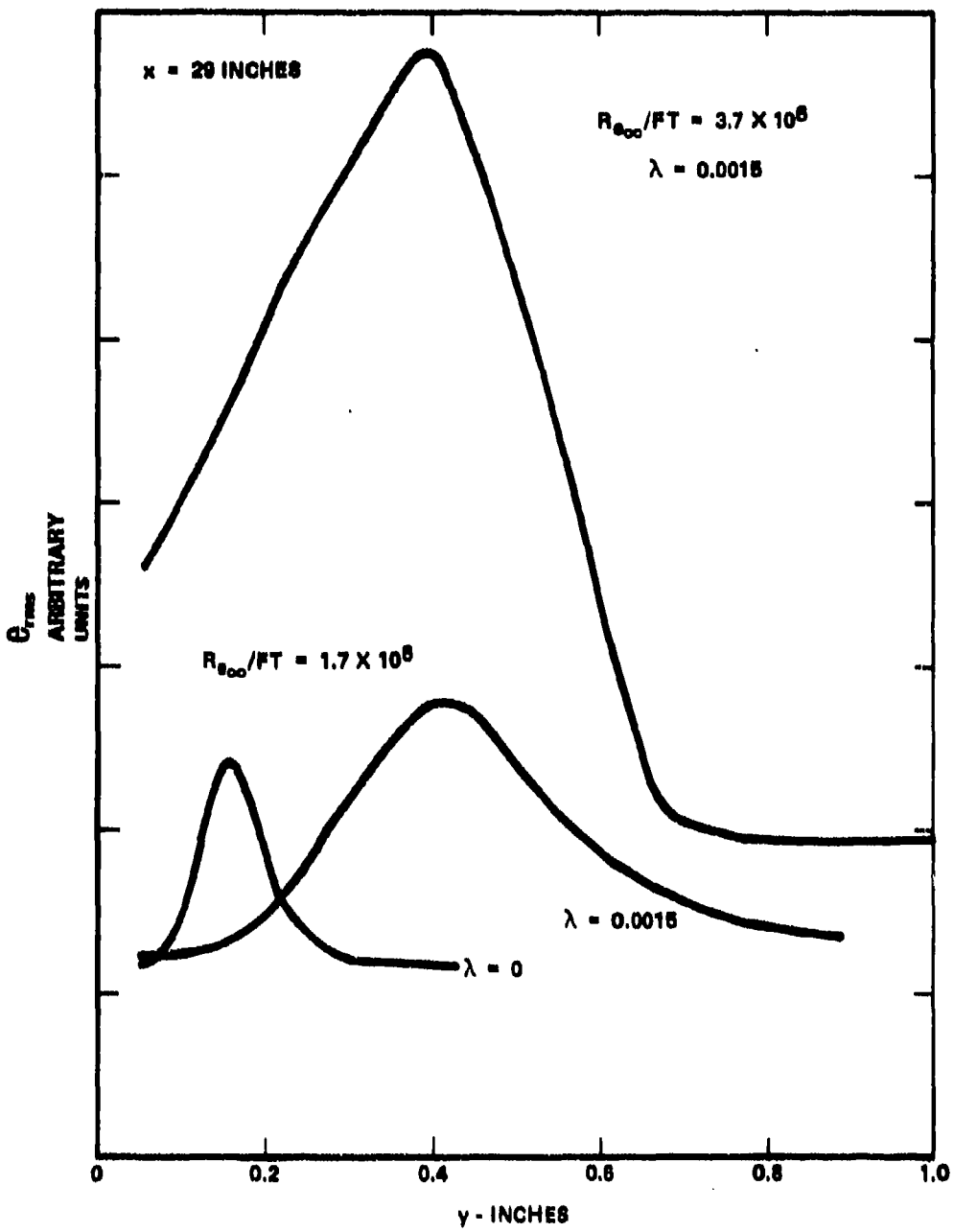

FIGURE 25. TYPICAL VARIATION OF WIDEBAND HOT-WIRE SIGNAL AT FIXED OVERHEAT CURRENT ACROSS THE BOUNDARY LAYER SHOWING EFFECT OF REYNOLDS NUMBER AND BLOWING RATE.

from the newly treated surfaces. It is recommended, therefore, that subsequent hot-wire tests should not be scheduled to immediately follow a tunnel down-time.

During these tests it was also observed that wires with a large aspect ratio (i.e., $\ell/d > 200$) have poor survival times in the flow. This accounts for the lack of turbulence data with blowing at the x = 55 inch station. These tests were performed at the end of the entry when the short aspect ratio wires were no longer available. Subsequent hot-wire tests should be carried out, therefore, using wires with aspect ratios in the range from 150 to 180. The present test results confirm that in spite of the large end loss effects associated with short aspect ratios, the unit Reynolds number in Tunnel B is sufficiently large that such wires have an adequate sensitivity for turbulence measurements.

It should be pointed out that the probe retraction and traversing mechanism operated in a satisfactory manner and was effectively utilized in the installation of the fifteen hot-wires used during the experiment. Most important, the interest and cooperation of the ARO personnel assigned to this task was instrumental in the success of the test program.

An example of the spectral content of the turbulent fluctuations, as well as an indication of the exceptional quality of the signals, is presented in Figure 26 which was obtained by playback of the hot-wire output recorded at x = 19 and 29 inches for the PF5 condition through the wave analyzer and to an x-y plotter. This figure shows the frequency resolved signals corresponding to the noise and the ten overheat currents for selected positions within the boundary-layer. At x = 19 inches, the maximum signal occurs at $y/\delta \approx 0.6$ where it is dominated by a 175 kc component which corresponds closely to the 160 kc frequency characteristic of the wave structure observed near the edge of the laminar-like boundary-layer. The hot-wire signal quickly diminishes to near zero as both the wall and the free-stream are approached. In contrast, at x = 29 inches, the boundary-layer is fully turbulent and relatively large fluctuations occur throughout the entire boundary-layer with a peak occurring at $y/\delta \approx 0.25$.

As an assist in validating the recorded data, the AEDC computer was programmed to carry out a wideband modal analysis using e_{rms} values uncorrected for the frequency response of the electronics. The method of analysis was based on the HOTWIRE programs described in Reference 1 which were developed for reduction of similar boundary-layer data acquired in the JPL/HWT. This on-site capability permitted the calculation of the y distribution of modally resolved fluctuation intensities for boundary-layer surveys performed at five x stations prior to the end of the Phase IV entry. In addition, results for three more surveys were available within several days following the termination of the test. The results of the modal analysis, which at this stage must be considered a preliminary estimate, yielded fluctuation intensities consistent with expectations based on other experiments, verified that the hot-wires were operated with an adequate overheat range, and indicated in most cases the exceptional quality of the raw signals. The latter is illustrated in Figure 27, where mode diagrams for eight positions in the boundary-layer at the x = 39 inch station for the PF3 condition have been plotted. There is relatively little scatter in the data, represented by the open circles, and the least squares fit to the theoretical hyperbola, indicated by the solid lines, is extremely good.

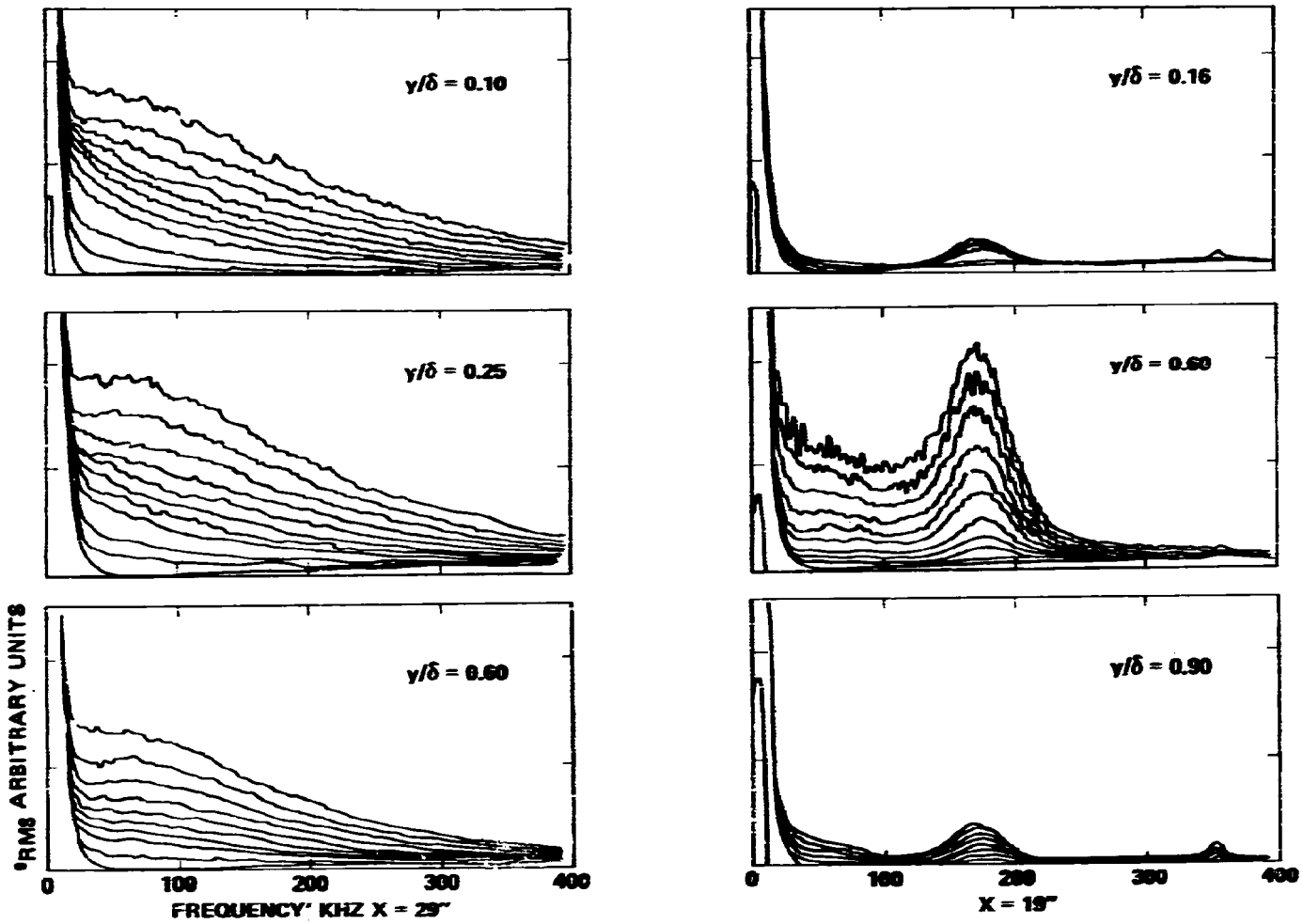

FIGURE 26. TYPICAL SPECTRA OF HOT-WIRE SIGNALS FOR: (A) TURBULENT BOUNDARY LAYER, AND (B) "LAMINAR LIKE" BOUNDARY LAYER. EACH CURVE CORRESPONDS TO FIXED OVERHEAT CURRENT.

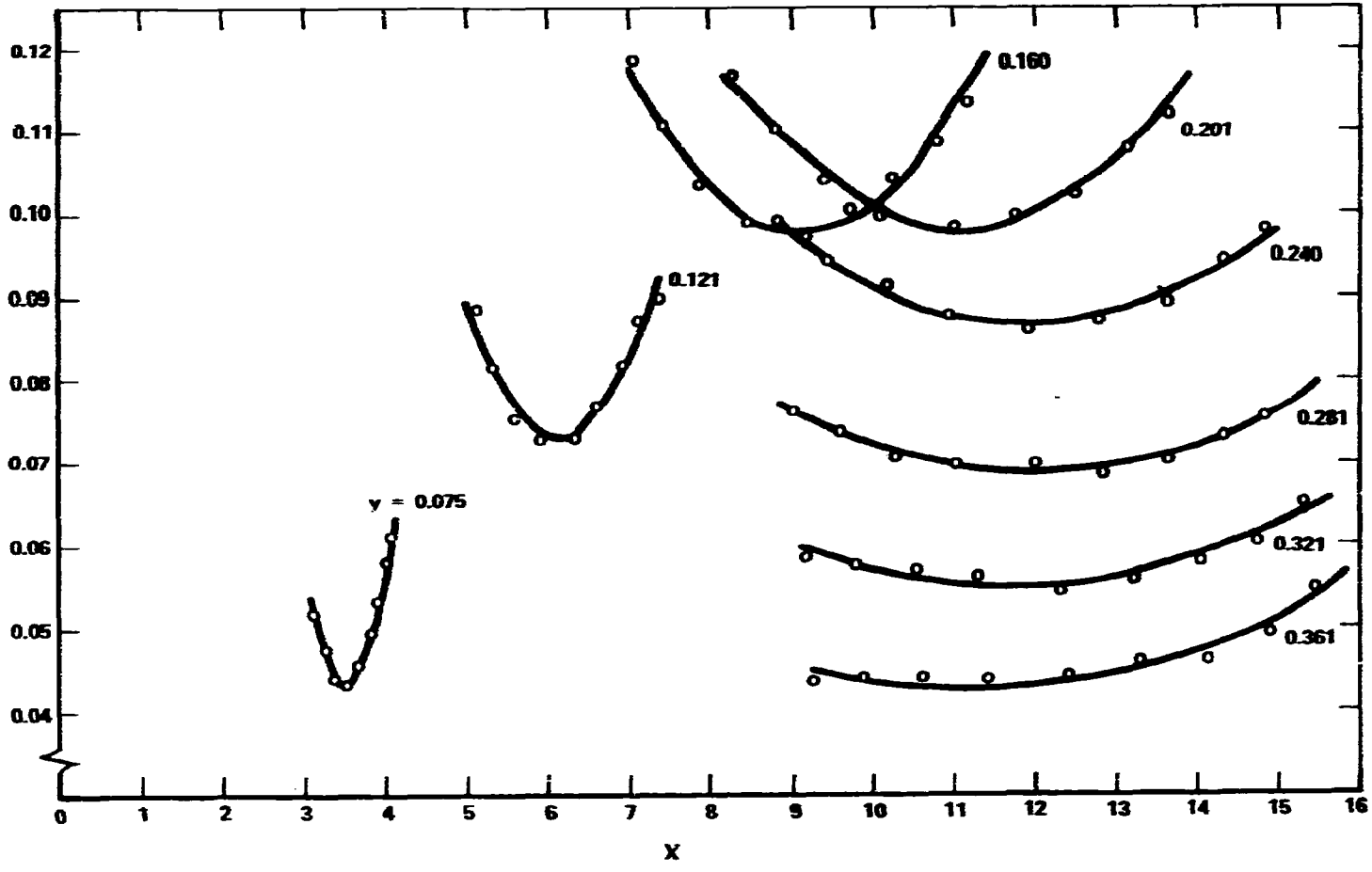

FIGURE 27. TYPICAL MODE DIAGRAMS OF HOT-WIRE DATA FOR P_o = 350 psi, λ = 0, AT x-STATION = 39 INCHES. OPEN CIRCLES INDICATE DATA POINTS AND SOLID LINES REPRESENT CURVE FITS USED TO DEDUCE FLUCTUATION INTENSITIES.

The y-distributions of temperature and velocity fluctuation intensities (for the purpose of data validation, the pressure fluctuations were assumed to be negligible) obtained from the on-site analysis are plotted in Figures 28 and 29 for P_0 = 350 and 600 psia, respectively. For the low tunnel pressure in particular, these figures depict the development of turbulence in the boundary-layer growing over a 5° cone at Mach 8 with an equilibrium wall condition. They indicate further that blowing at λ = 0.0015 increases the peak fluctuations only slightly over the non-blowing case, and more significantly, that the temperature fluctuations in both cases are as large as 30-40%. Clearly, fluctuations of this magnitude cannot be handled by the linear theory which forms the basis of the conventional mode analysis and final reduction of the data will require a reformulation of the basic treatment of the problem.

3.5 STATUS AND PLANS

Final calculation of mean flow profiles by AEDC using mean flow measurements made by Philco-Ford are in progress. The preliminary modal analysis carried out on-site are being checked in order to delineate potential problem areas during the final analysis. Calculation of the hot-wire sensitivity coefficients needed for the computer program DRA2E, described in Reference 1, and digitization of the hot-wire fluctuation signal, which is required for frequency resolved analysis of the data, will be initiated shortly. In view of the large fluctuation intensities discovered so far, the hot-wire theory will be re-examined and methods to account for non-linear disturbances will be sought.

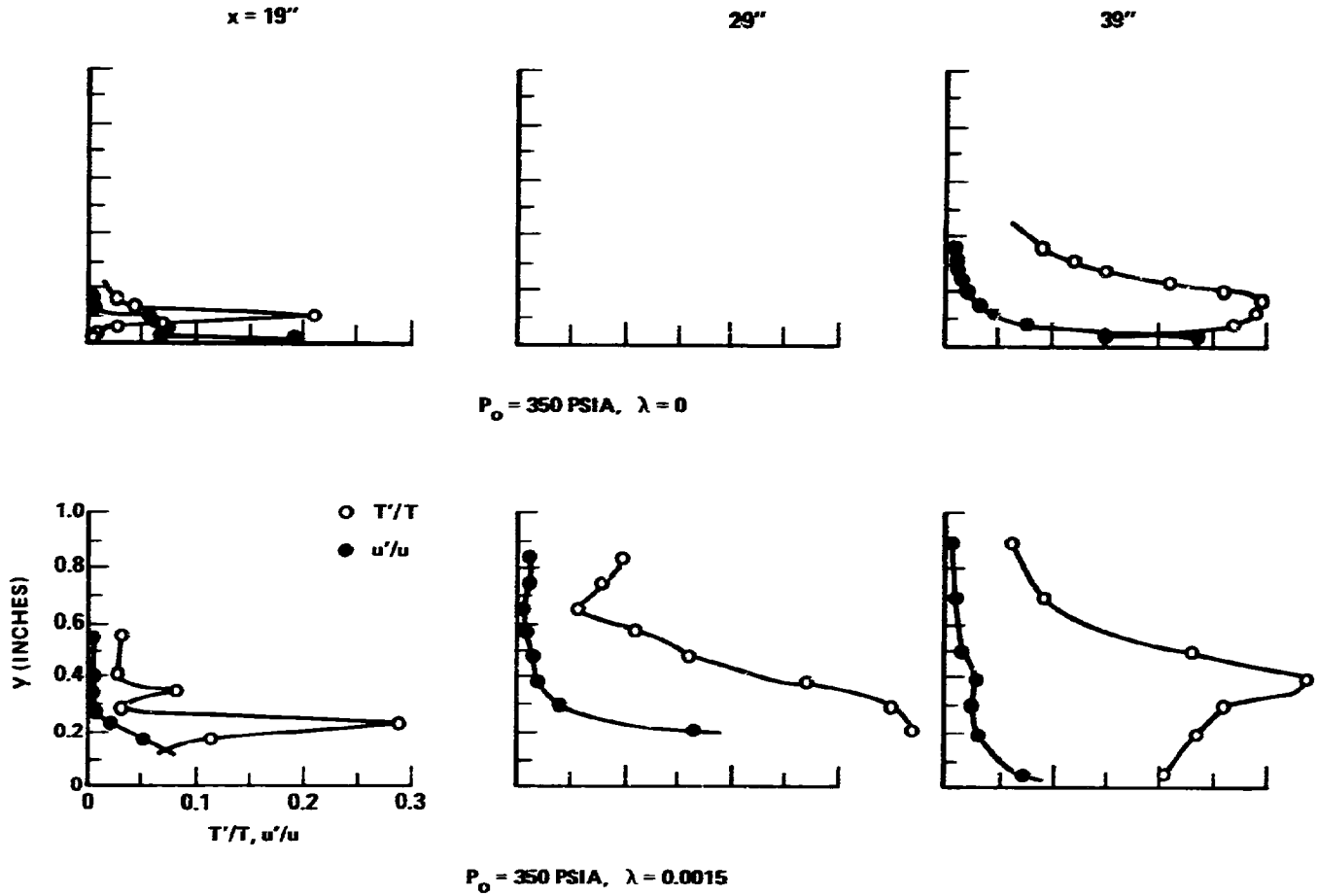

FIGURE 28. RESULTS OF PRELIMINARY ANALYSIS SHOWING VELOCITY AND TEMPERATURE FLUCTUATIONS AT P_o = 350 psi.

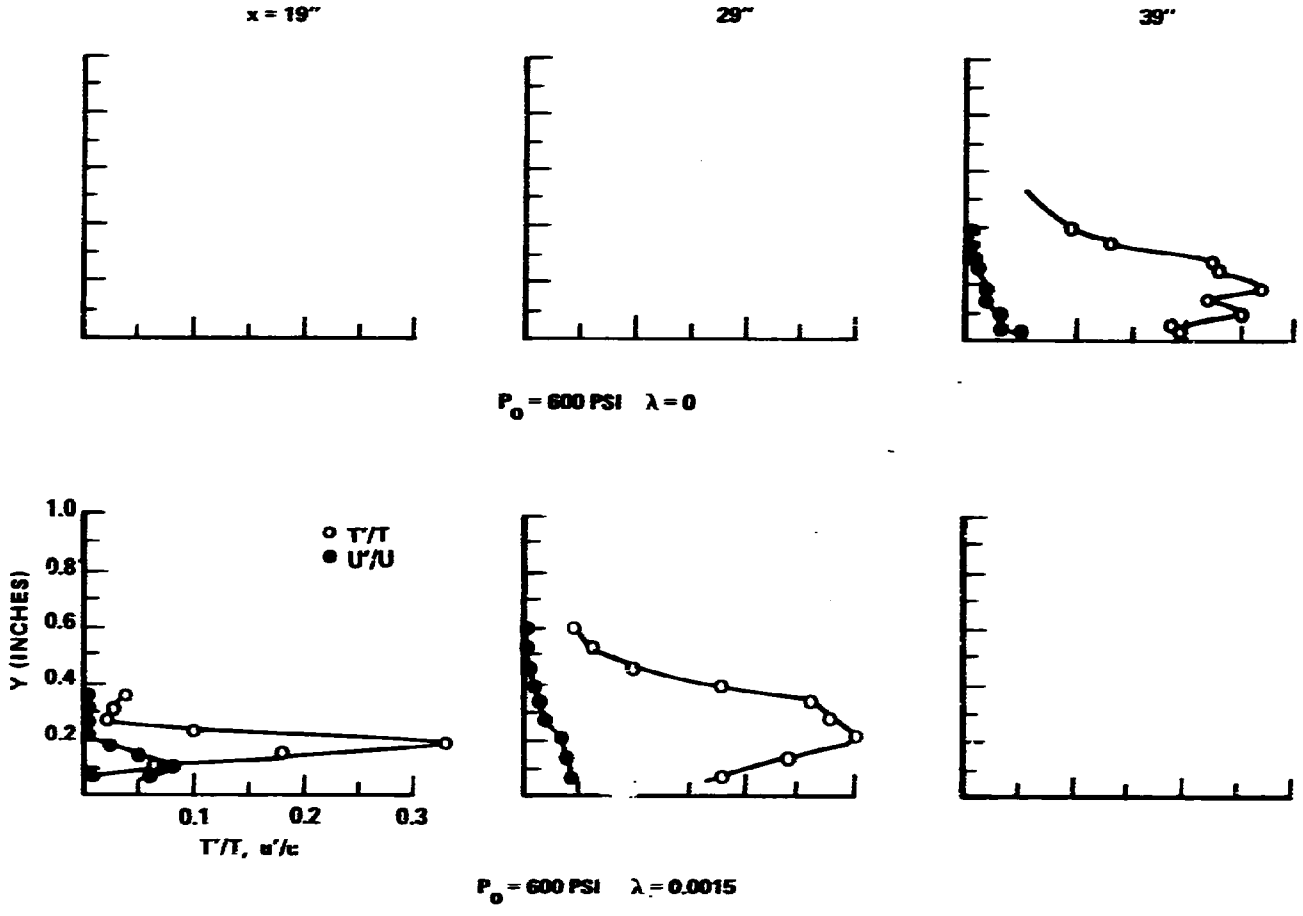

FIGURE 29. RESULTS OF PRELIMINARY ANALYSIS SHOWING VELOCITY AND TEMPERATURE FLUCTUATIONS AT P_o = 600 psi.

SECTION IV

CORRELATION OF BOUNDARY-LAYER FLUCTUATION RESULTS

In various tasks under the present contract results have been obtained on the distribution of turbulence in supersonic and hypersonic boundary-layers. Although the test design for each task aims at simulating specific flight conditions the simulation is always incomplete because of state-of-the-art limitations. In this section we shall attempt to see if a coherent picture emerges from comparison of the available results with each other.

4.1 AVAILABLE EXPERIMENTAL DATA

The available experimental data are shown on Table V. Criteria for selecting data from what is available in the literature were:

(1) The test conditions must be completely controlled.

(2) Sufficient data points must exist to present a coherent picture.

(3) The measuring technique must be reliable.

The data shown cover the range from Mach 0 to nearly 10; the low-speed data are included for purposes of comparison.* The momentum Reynolds number R_θ is also spread widely (from 10^3 to nearly 4×10^4). Most of the data are adiabatic (or nearly so) with no mass injection. The TBL-C results shown are still tentative since the data have not yet been fully reduced; they are taken from Section III of this report. Also, the WEM and TBL-A data are taken from Sections II and VI of this report.

4.2 VELOCITY-FLUCTUATION CORRELATIONS

Since there is no theory available the fluctuation distributions as a function of y/δ can be presented empirically correlated into some sort of a "curve" versus, say, Mach number; or it can be further fortified into a non-dimensional grouping which "collapses the data into one curve" including other parameters such as heat transfer.

Figure 30 shows the simplest non-dimensional correlation $u'/\bar{u}$ vs. y/δ where $\bar{u}$ is the local average flow speed. There is, generally, a tendency to decrease $u'/\bar{u}$ as M_e is increased. When the velocity u_e at the boundary-layer edge is used instead of $\bar{u}$ the decrease in the fluctuation intensity is not obvious (for the

---

* There appear to be several sets of low-speed fluctuation data which fulfill the above criteria. The data of Townsend (Reference 13) and Klebanoff (Reference 14) are typical of these.

TABLE V

EXPERIMENTS SUPPLYING HIGH-SPEED BOUNDARY-LAYER TURBULENCE DATA

DESIGNATION	SOURCE (WORKERS)	TEST SURFACE	M_e	Re_θ	$T_w/T_{o\infty}$	$\dot{m}$
"Low Speed"	Townsend, Klebanoff	Flat Plate	0	$O(10^3 - 10^4)$	1	0
Kistler	Kistler	Flat Plate	1.72 3.56 4.76	3×10^4	1	0
WEM	Demetriades	Cone (5°)	3	10^3	1	0
TBL-A	Laderman Demetriades	Flat Plate	9.4	3.6×10^4 1.9×10^4	0.29	0
TBL-C	Laderman Demetriades	Cone (5°)	7.0	4.3×10^3	0.78	0, 0.0015

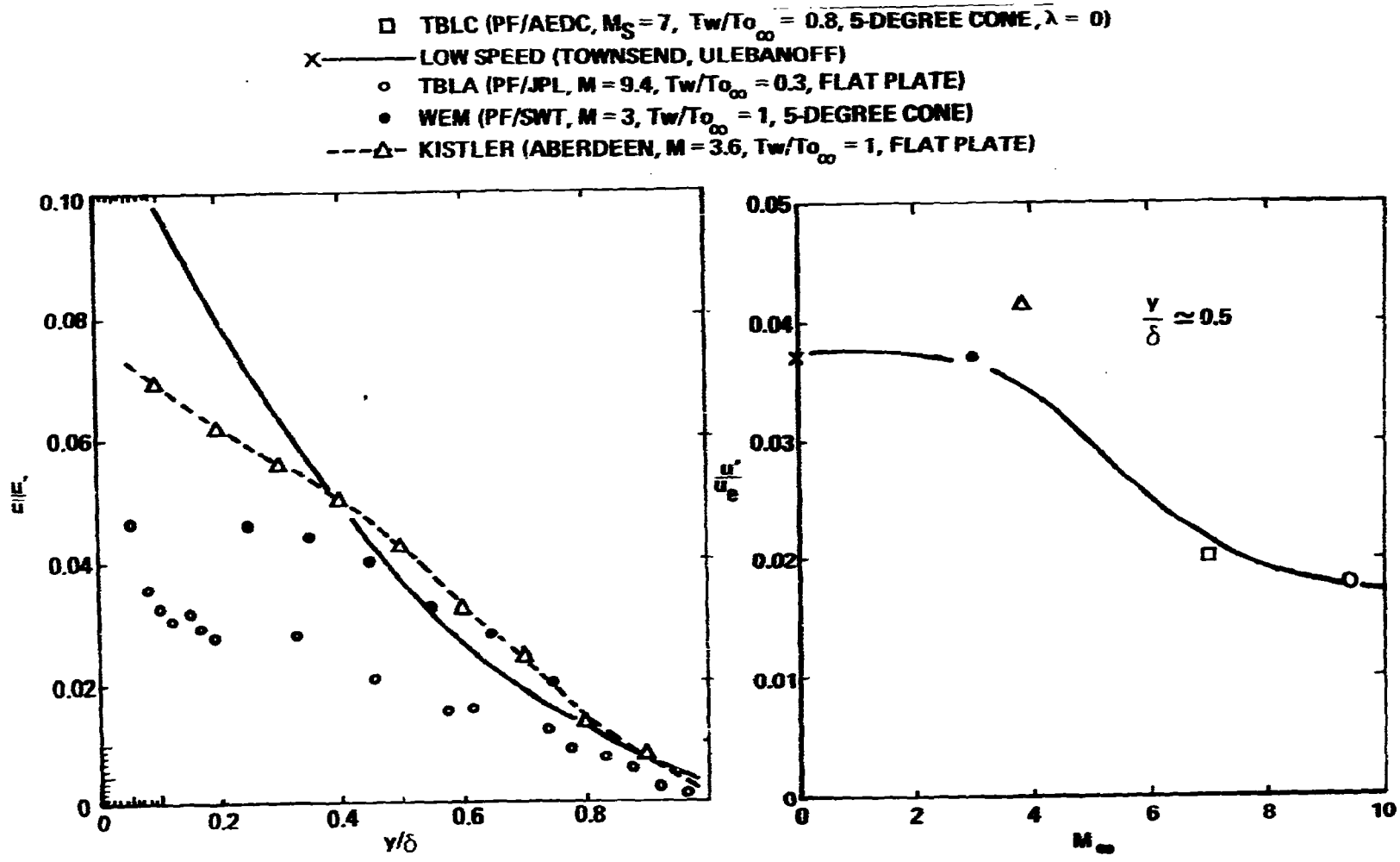

FIGURE 30 LONGITUDINAL WIDEBAND TURBULENCE COMPONENT IN BOUNDARY-LAYERS ($\bar{u}$ AND $\bar{u}_e$ CORRELATIONS).

typical position $y/\delta = 0.5$) until hypersonic Mach numbers are reached, as shown on the right in Figure 30. Nearer the wall, however, the correlation $u'/\bar{u}_e(y/\delta)$ shows a continuous decrease of the fluctuation magnitude as the Mach number departs from zero.

In his paper (Reference 9) Kistler follows the practice of the low-speed experimenters to normalize u' with the "shear velocity"

$$u_\tau = (\tau_w/\rho_w)^{\frac{1}{2}}$$

The u'/u_τ correlation, shown on Figure 31, still shows a strong Mach number dependence, even accounting for differences in R_θ or the temperature ratio T_w/T_o. It remains to be seen if the correlation improves (i.e., if the curves collapse) when the proper distance parameter

$$y^+ = \frac{u_\tau}{\nu_w} \int_0^y \frac{\rho}{\rho_e}\, dy$$

is considered in lieu of the physical distance y/δ shown on Figure 31. The reasoning for using the u'/u_τ vs. y^+ correlation is its well-known validity in collapsing <u>mean</u> flow data for high-speed boundary-layers (Reference 2).

Another possible correlation comes from Morkovin's hypothesis (The "Dynamic Equilibrium Hypothesis", Reference 15) that the "universal" form of the fluctuations is restricted to the turbulent energy $\rho\overline{u'^2}$, as opposed to the turbulence velocity u' alone. The proper parameter to plot, then, is the quantity $(u'/u_\tau).(\rho/\rho_w)^{\frac{1}{2}}$. This has been attempted in Figure 32, for which some data (Reference 16) other than those discussed so far are also shown. There is indeed some improvement over the method of plotting of Figure 31 (where the density factor [illegible] had been omitted) in the outer half of the boundary-layer. Near the wa[illegible] [illegible]ever, this latest plotting method still shows scatter by a factor of more th[illegible] 2 in the data. Also, the turbulent energy is a more complex expression than just $\rho\overline{u'^2}$ which is, in fact, probably smaller numerically than the omitted terms. It is thought necessary to look into this matter further, i.e., to improve on Morkovin's correlation by plotting the complete energy term vs. y^+.

4.3 TEMPERATURE-FLUCTUATION CORRELATIONS

The local wideband temperature fluctuations have been plotted on Figure 33 normalized with the local average temperature $\bar{T}$. The graph on the left does not include the tentative TBL-C data (see Section III), but these results are included in the cross-plot (at $y/\delta = 0.5$) shown on the right. It is seen that the adiabatic or near-adiabatic tests show a very rapid increase of the fluctuation intensities with Mach number. Beginning from $T'/\bar{T} = 0$ at $M = 0$ (by definition) these fluctuations have increased to about 22% at $M = 7$. It must also be noted that the qualitative data of Wagner and his co-workers (Reference 17), excluded

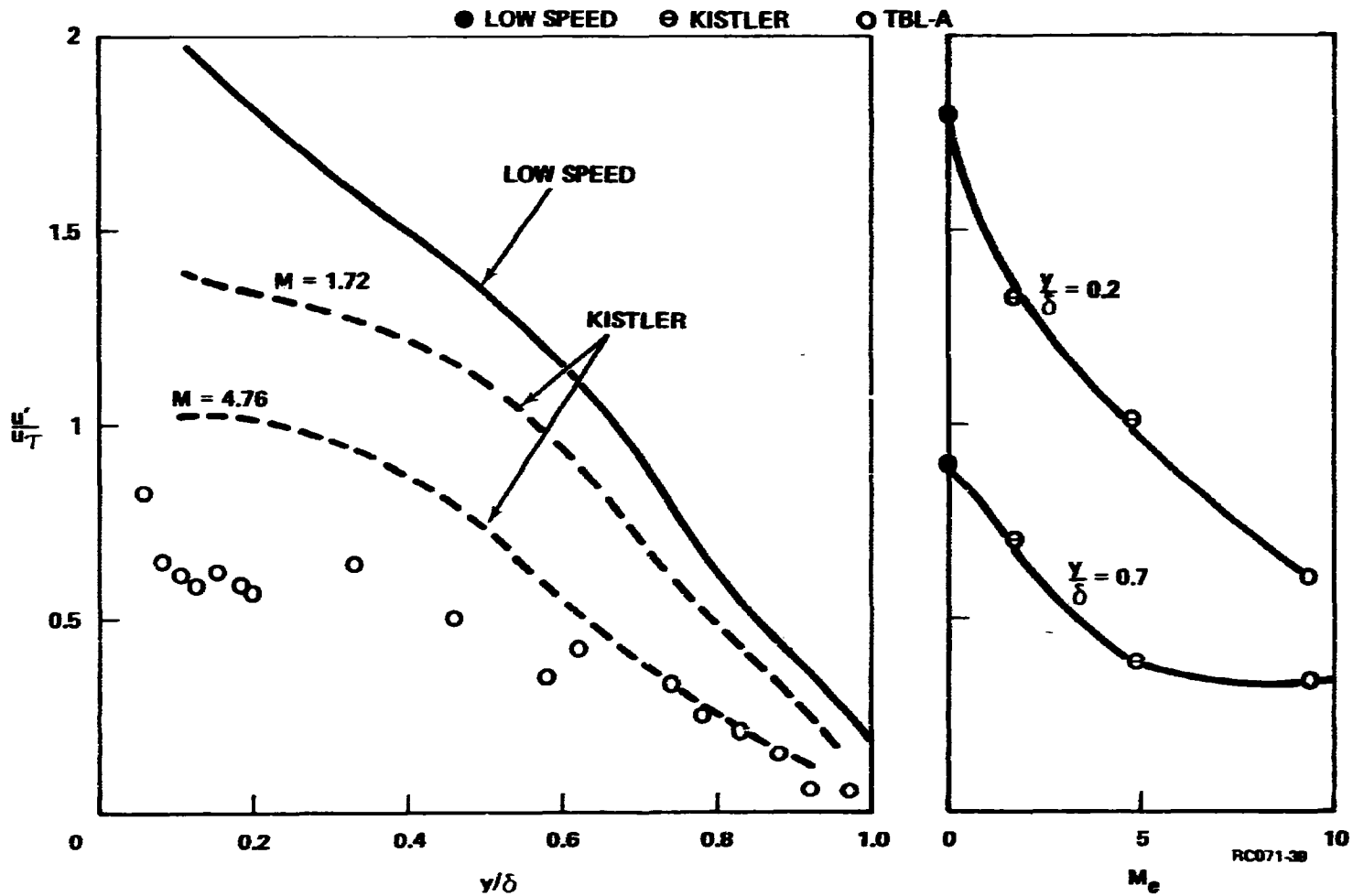

FIGURE 31. LONGITUDINAL WIDEBAND TURBULENCE COMPONENT IN BOUNDARY-LAYERS (u_τ CORRELATIONS).

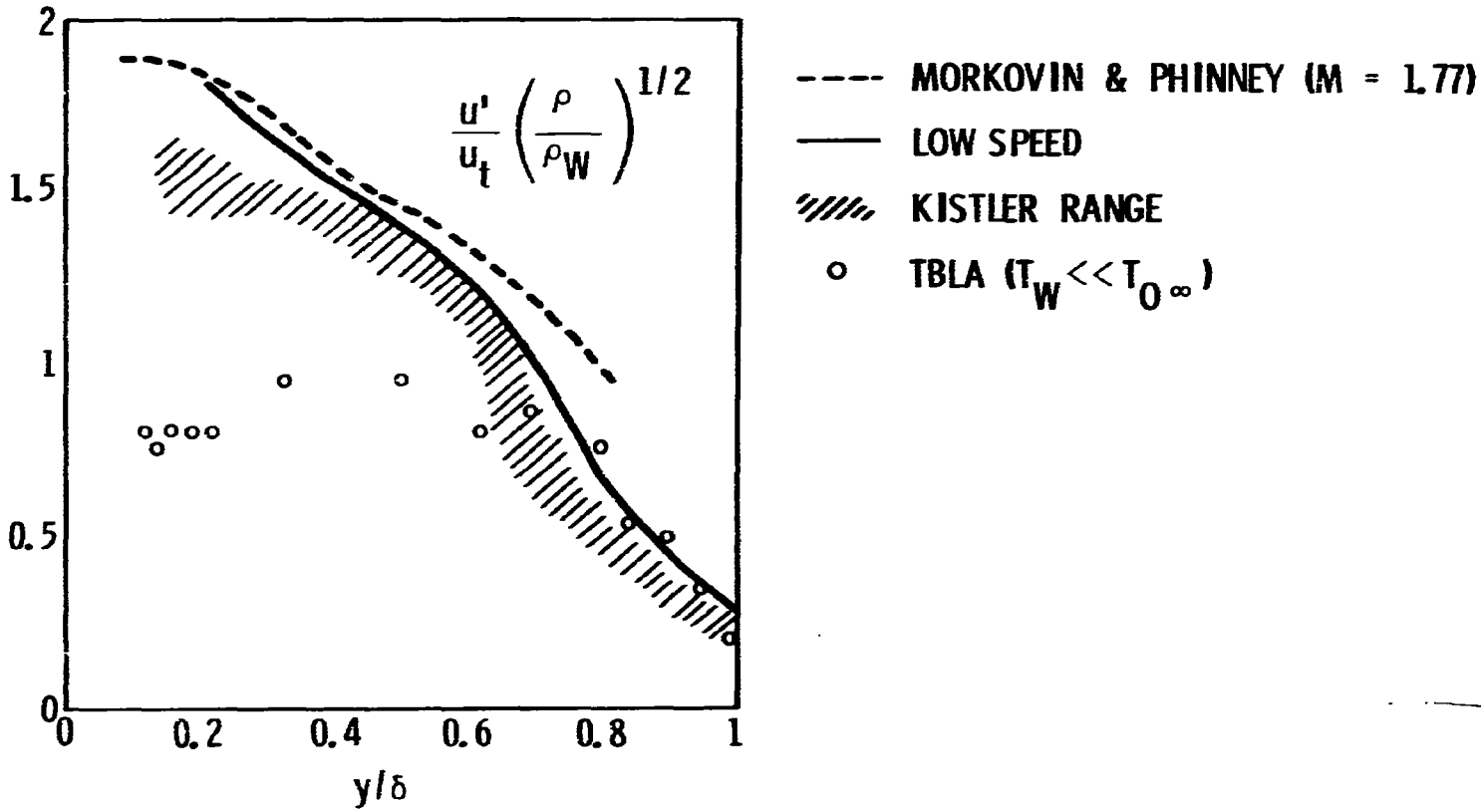

RC071-33

FIGURE 32. CORRELATION OF WIDEBAND LONGITUDINAL VELOCITY FLUCTUATIONS BASED ON FRICTION-VELOCITY SCHEME FOR COMPRESSIBLE FLOW.

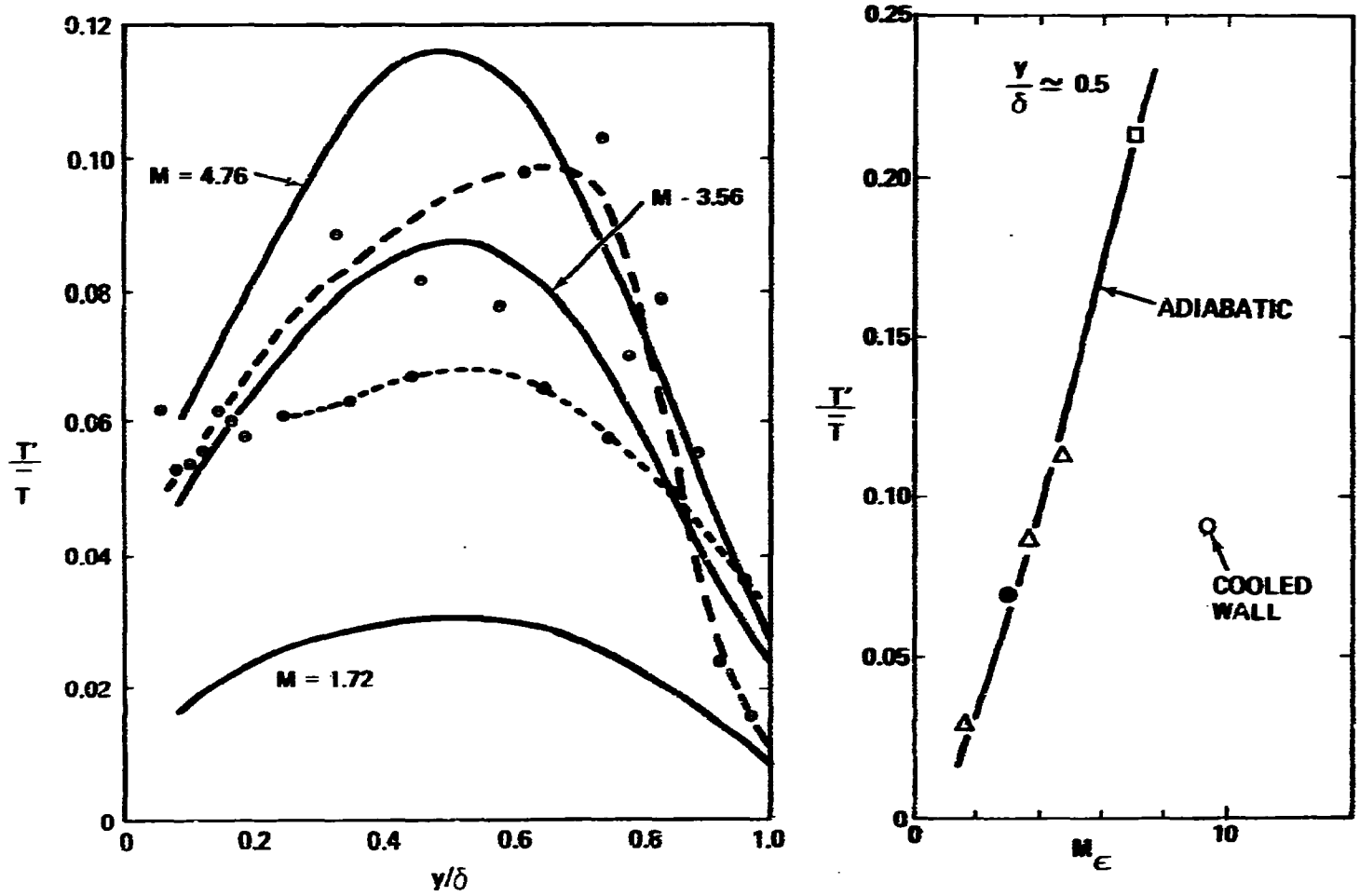

FIGURE 33. WIDEBAND STATIC TEMPERATURE FLUCTUATIONS IN BOUNDARY-LAYER.

here because of the criteria of Section 4.1, have shown $T'/\bar{T}$ of order 100% at $M = 20$. This result of Wagner's had been earlier subject to suspicion because it was obtained with a linearized technique which is invalid for such large fluctuations. Nevertheless, in view of the results of Figure 33, it can at least be stated that at $M = 20$ the $T'/\bar{T}$ must be very large indeed. On the other hand, the "cooled wall" point of Figure 33 (from TBL-A, Reference 2 and Section II of this report) shows a very strong effect of heat transfer on $T'/\bar{T}$.

An attempt to better correlate the results of Figure 33 was made by modifying slightly Kistler's original suggestion (Reference 9). This suggestion is that the fluctuations of a passive scalar such as temperature are "driven" by the temperature difference $T_0 - T_e$, i.e., the total minus the static stream temperature. Actually, the driving force is the temperature drop $T_r - T_e$ across the boundary-layer. In adiabatic flows T_r is very nearly T_0, but with heat transfer T_r is the wall temperature T_w. Also, $\bar{T}$ is itself normalized with the "average" temperature $(T_r + T_e)/2$, so that finally the resulting quantity plotted is

$$\frac{1}{2}\,\frac{T'}{\bar{T}}\,\frac{T_r + T_e}{T_r - T_e} \quad \text{versus} \quad y/\delta,$$

where T_r is actually the wall temperature. The results, less the TBL-C data, are plotted on Figure 34. The scatter from the data of one experiment to the other is considerably reduced in this manner. The TBL-A results are plotted in two different ways, one by assuming $T_r = T_0$ and the other $T_r = T_w$. The latter gives better agreement, implying that the correlation is best when the wall temperature is indeed chosen. The importance of this finding is that cases with heat transfer can be taken care of in this way.

4.4 CONCLUSIONS FROM THE CORRELATION STUDY

On the basis of the experimental data studied so far the following conclusions are drawn:

(a) There is a tendency of increasing Mach number to decrease the longitudinal velocity fluctuations.

(b) The best correlation is obtained by using the "dynamic equilibrium hypothesis" of plotting $(u'/u_\tau)\cdot(\rho/\rho_w)^{\frac{1}{2}}$. However the correlation is good only in the outer half of the layer; it is invalid near the wall if the physical distance y/δ is used.

(c) The static temperature fluctuations $T'/\bar{T}$ appear better correlated if plotted versus $2(T_w - T_e)\ f\ (y/\delta)/(T_w + T_e)$. This scaling formula predicts that $T'/\bar{T}$ increase sharply with M and decrease greatly when the wall is cooled.

(d) Provided that the layer thickness is much smaller than the transverse curvature there is no effect of geometry (flat plate versus

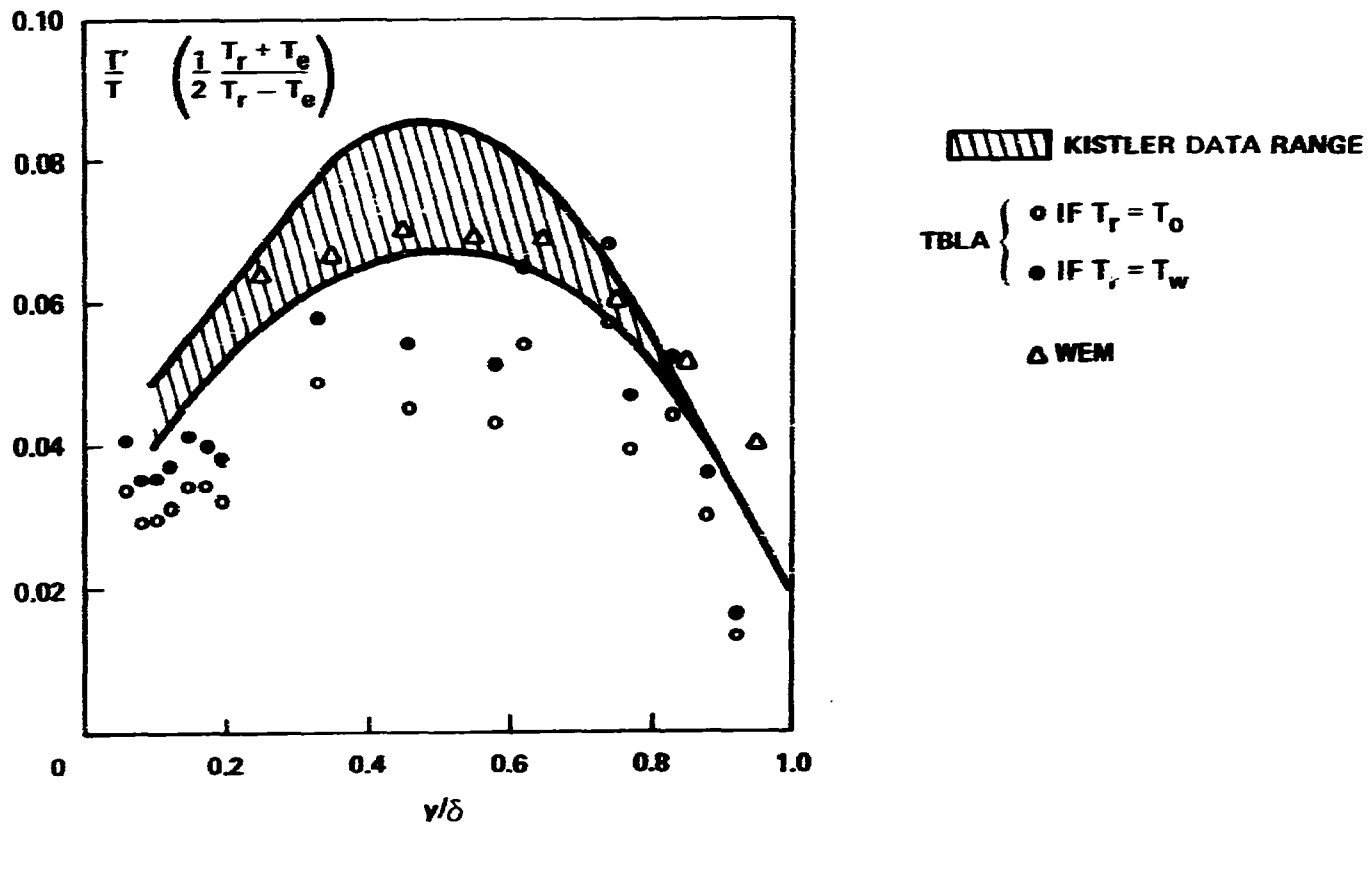

FIGURE 34. CORRELATION OF WIDEBAND TEMPERATURE FLUCTUATIONS IN SUPERSONIC/HYPERSONIC BOUNDARY LAYERS.

cone), and there seems to be no great effect of Reynolds number. The most important influence found is that of the heat transfer on the $T'/\overline{T}$.

4.5 STATUS AND PLANS

From the numerical data presented and from the above conclusions it is now possible to estimate the fluctuation intensity $u'/\overline{u}$ and $T'/\overline{T}$ for boundary-layers in the range $0 < M < 10$. However the conclusions are tentative because the data base is very small; each test discussed involves changes in at least two parameters compared with any other test. Therefore it is not certain which of the two flow parameters create the changes noted between any two experiments. Some parameters (e.g., heat transfer) are present in only one experiment, while some, such as mass addition or pressure gradient, have not as yet been covered.

In the meantime, it is planned to continue the effort to correlate the data along the following lines:

(1) Forthcoming data from the current Philco-Ford experiments will be analyzed and plotted in a manner such as that of Figures 30 through 34. These data include:

   (a) TBL-C data which include wider variations in R_θ (such as obtained by using the profiles at different x-distances from the cone tip) and mass addition to the extent $\dot{m}/\rho_e u_e = 0.0015$.

   (b) WEM data which also include wider variations of R_θ. The profile at the cone shoulder at condition C ($P_o = 530$ mm Hg, see Section VI) will be available shortly.

(2) The velocity fluctuation data of Figure 32 will be re-plotted to change the abscissa to y^+. This will involve modifying other worker's data into this coordinate system.

(3) The velocity fluctuations will be further plotted with coordinates which include the total turbulent kinetic energy.

SECTION V

MEASUREMENT OF SHEAR STRESSES IN A HYPERSONIC BOUNDARY-LAYER

5.1 PURPOSE

The purpose of this task is the measurement of the turbulent shear stress (the so-called "Reynolds stress") in a hypersonic boundary-layer.

5.2 SUMMARY OF PREVIOUS WORK

Work on this problem was initiated in the fall of 1971 with the development of techniques for fabricating and calibrating the X-array hot-wire anemometers used for the shear stress measurements and was temporarily halted in April 1972 following the completion of the experimental program. Tests were performed in the JPL Hypersonic Wind Tunnel under the same conditions used in the TBL-A experiment (References 1 and 2). This provided the advantage of making shear stress measurements in a boundary-layer whose mean and fluctuating flow had already been well-defined. A total of eight 10,000 foot tapes of recorded data were acquired representing about 60 y positions in the boundary-layer. Of these data roughly one-third is suspected to be of inferior quality due to excessive scatter in the measured wire resistance, leaving therefore nearly 40 points of useful information.

In addition to the measurements, equations governing the "general" behavior of X-probes in compressible, turbulent flows were derived (assuming negligible pressure fluctuations) providing the means for deducing the shear stress terms from the hot-wire signals. Preliminary calculations indicated that the fluctuations $\overline{u'^2}$, $\overline{T'^2}$ and $\overline{u'T'}$ are numerically similar to those found with a single wire in the TBL-A experiment; thereby establishing confidence in the validity of the remaining unknowns, $\overline{T'v'}$, $\overline{u'v'}$ and $\overline{v'^2}$. In addition, approximate calculations of the latter parameters were carried out at three positions on the boundary-layer. The $\overline{v'^2}$ was found to lie numerically below $\overline{u'^2}$ as expected, while the correlations $\overline{u'v'}$ and $\overline{v'T'}$ were found to be negative as anticipated near the wall but to change sign near the outer edge. It is not known whether the latter result is real or a consequence of the incompleteness of the preliminary analysis.

5.3 PRESENT STATUS

Since the TBL-A experiments indicated the importance of pressure fluctuations at hypersonic speeds, the X-probe theory developed previously has been extended to include this effect. Details of this formulation are presented in Appendix B. In the case of negligible pressure fluctuations, the X-probe theory leads to six linear simultaneous equations of sufficiently simple form to be solved by hand if necessary. With finite pressure fluctuations, several restrictive assumptions concerning the correlation between the sound and other modes are required and while six governing equations are again obtained, in this case the equations are non-linear and cannot be solved without the aid of a computer. For this reason, and since the results of TBL-A indicated that the magnitude of velocity and temperature fluctuations obtained from a no-sound assumption are increased only slightly above their corresponding values when relatively large pressure

fluctuations are accounted for, it is planned to reduce the X-probe data in two stages. First, a solution will be found by assuming a negligible sound field, thus providing an opportunity to compare $\overline{u'^2}$, $\overline{\theta'^2}$ and $\overline{u'\theta'}$ with the no-sound results of TBL-A and to assess the relative quality of the X-probe data. When this is accomplished the more complex solution allowing finite pressure fluctuations will be carried out.

Calculation of the hot-wire sensitivity coefficients, which are needed to interpret the X-probe data, has also been initiated. This calculation requires a knowledge of the heat transfer characteristics of the wire which is usually acquired from a flow calibration yielding the Nusselt number - Reynolds number and recovery factor - Reynolds number relations of the probe. The flow calibration is generally accomplished by locating the wire in the free stream of the wind-tunnel, and prior to these tests, the calibration data was obtained by hand-recording several i, e pairs in order to find the zero current R and dR/di^2 values used to evaluate Nu and η. From the overheat traverses carried out during the boundary-layer survey, the local Nu can be found and used with the heat transfer calibrations to determine the corresponding derivatives d log Nu/d log Re and d log η/d log Re appearing in the expression of the sensitivity coefficients (see for example Reference 17).

Because of drift in tunnel conditions during the time required for calibration and scatter in the hand-recorded i, e data, significant uncertainty is frequently introduced in the heat transfer calibration. In order to improve the calibration, an analog circuit was designed and first used during the X-probe tests. The circuit receives as input instantaneous i, e values and outputs, directly to an X-Y plotter, the corresponding R and i^2. The calibration, at a given tunnel condition, is obtained in a matter of seconds by increasing the current from zero to a preselected maximum value by means of a single potentiometer acting as a series resistor in the hot-wire circuit.

To check the performance of the analog circuit during its first usage with X-probe No. 4, calibration data was also obtained by hand-recording i, e pairs. The results are shown in Figures 35 and 36 where the analog calibration is indicated as triangles and the hand-recorded data as open circles. The solid lines drawn through the data points represent a least-squares fit to the analog calibration data. A slight but consistent difference is observed for both wires except for the Nu-Re relation for wire 4-2A, where there is a large divergence between the two calibration procedures. This discrepancy was resolved deriving a calibration using local Nusselt numbers determined from the boundary-layer survey and local Reynolds numbers and total temperatures from the mean flow measurements of TBL-A. This "boundary-layer" calibration is depicted as squares in Figures 35 and 36. The resulting Nu-Re relation, Figure 35, is seen to be in excellent agreement with the analog calibration for both wires (except for the high Re data for wire 4-2A). However, the corresponding η-Re relation, Figure 36, shows poor agreement with the free-stream results, particularly for wire 4-2A which exhibits a behavior which cannot be rationalized on physical grounds. The "boundary-layer" calibration demonstrates the superiority of the analog technique for obtaining an accurate Nusselt-Reynolds relation and, until an explanation is evolved for concerning the recovery factor data derived from the boundary-layer measurements, the free-stream calibration of this parameter will be considered to provide a reliable η-Re correlation.

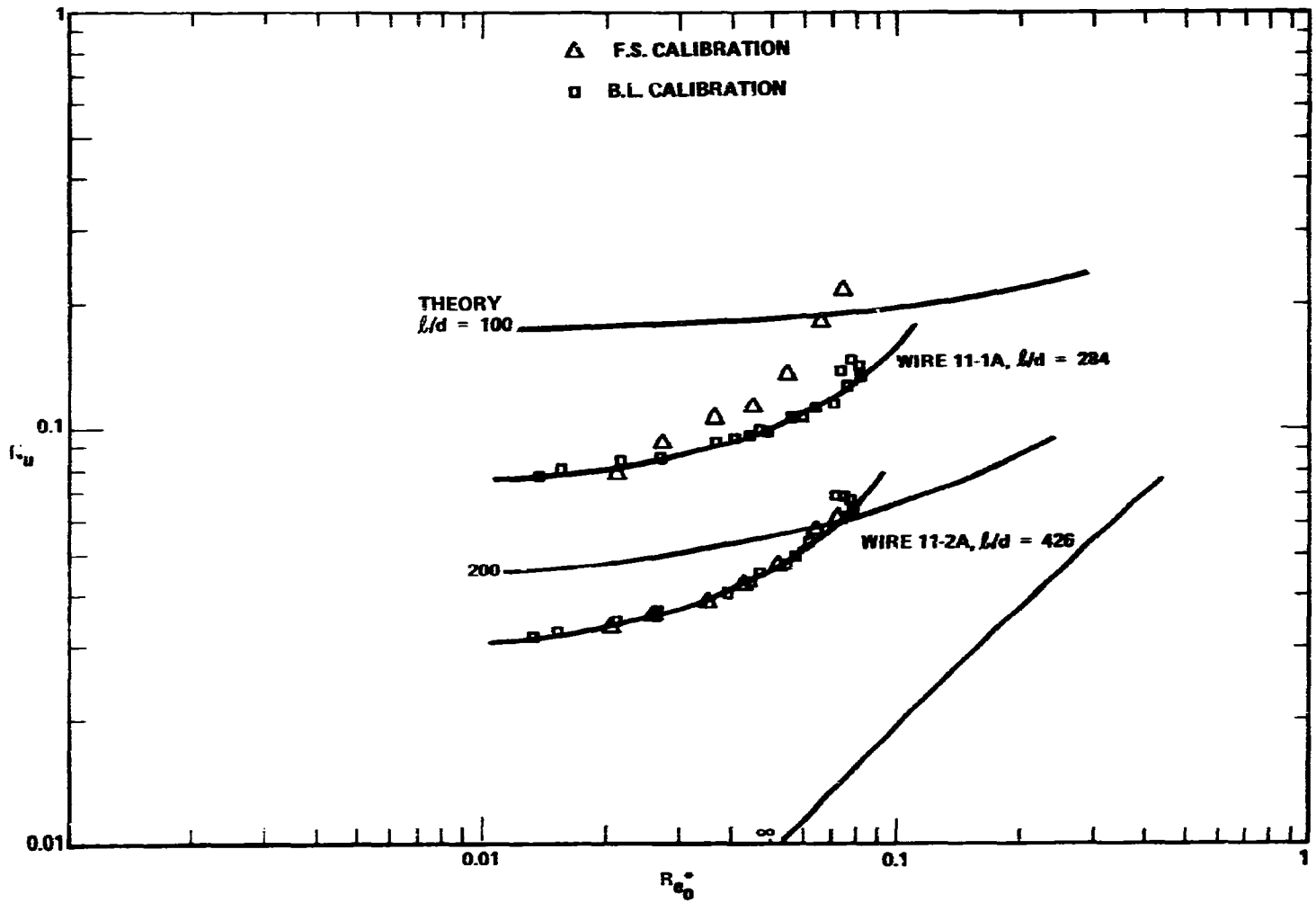

FIGURE 35. NUSSELT NUMBER - REYNOLDS NUMBER CALIBRATION FOR X-PROBE NO. 11.

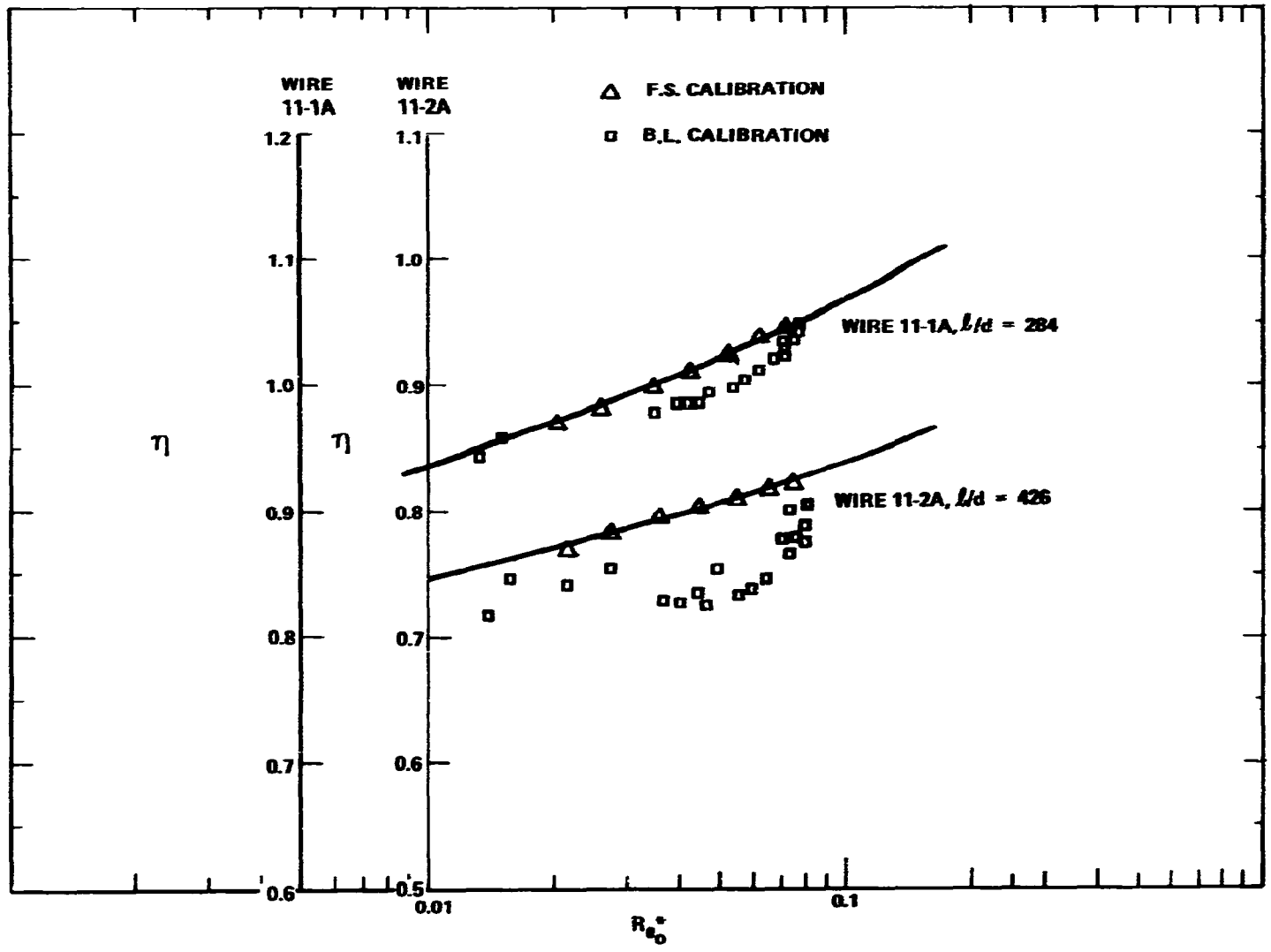

FIGURE 36. RECOVERY FACTOR - REYNOLDS NUMBER CALIBRATION FOR X-PROBE NO. 11.

A similar calibration difficulty was encountered with X-probe No. 11, for which only the analog circuit was used. For wire 11-1A, the current range was insufficient to provide accurate values of dR/di^2 and the resulting Nusselt calibration, shown for both wires 11-1A and 11-2A as the triangles in Figure 37, was suspect. Again a "boundary-layer" calibration was carried out which differed considerably from the analog calibration of wire 11-1A although good agreement with that of wire 11-2A was obtained. This was interpreted again as indicating the validity of the analog calibration technique provided a sufficient current range is used. The η-Re calibration for the two wires, Figure 38, shows the same behavior for the boundary-layer data exhibited by X-probe No. 4, although the data for wire 11-2A approaches much closer the free-stream analog results. This implies that the free-stream calibration of η versus Re is, indeed, a reliable indication of the recovery factor characteristic of the probe.

As a result of the preceding exercise, an alternate method of data reduction was evolved to smooth the small experimental errors in the Nusselt number measurement that are apparent in Figures 35 and 37. In the TBL-A program, the logarithmic derivatives of Nu and η were determined by calculating the zero current R and dR/di^2 from the local overheat traverse, using an iterative technique to find Re, Nu, and η, and evaluating the derivatives from the curve-fitted expressions to the heat transfer calibrations. In the present case, however, it has been decided to use the well-defined mean flow profiles to specify the local Re, so that the derivatives can be calculated directly from the calibration equations, thereby ensuring a smooth monatomic increase (or decrease) in the value of these quantities. This should lead to a substantial improvement in the accuracy of the sensitivity coefficients and, eventually, of the modal analysis.

The following tasks remain before final analysis of the X-probe data can be carried out:

(1) Complete calculation of sensitivity coefficients.

(2) Digitize hot-wire signals for computer processing.

(3) Modify and extend computer program DRA2E to accommodate equations and logic required for X-probe analysis.

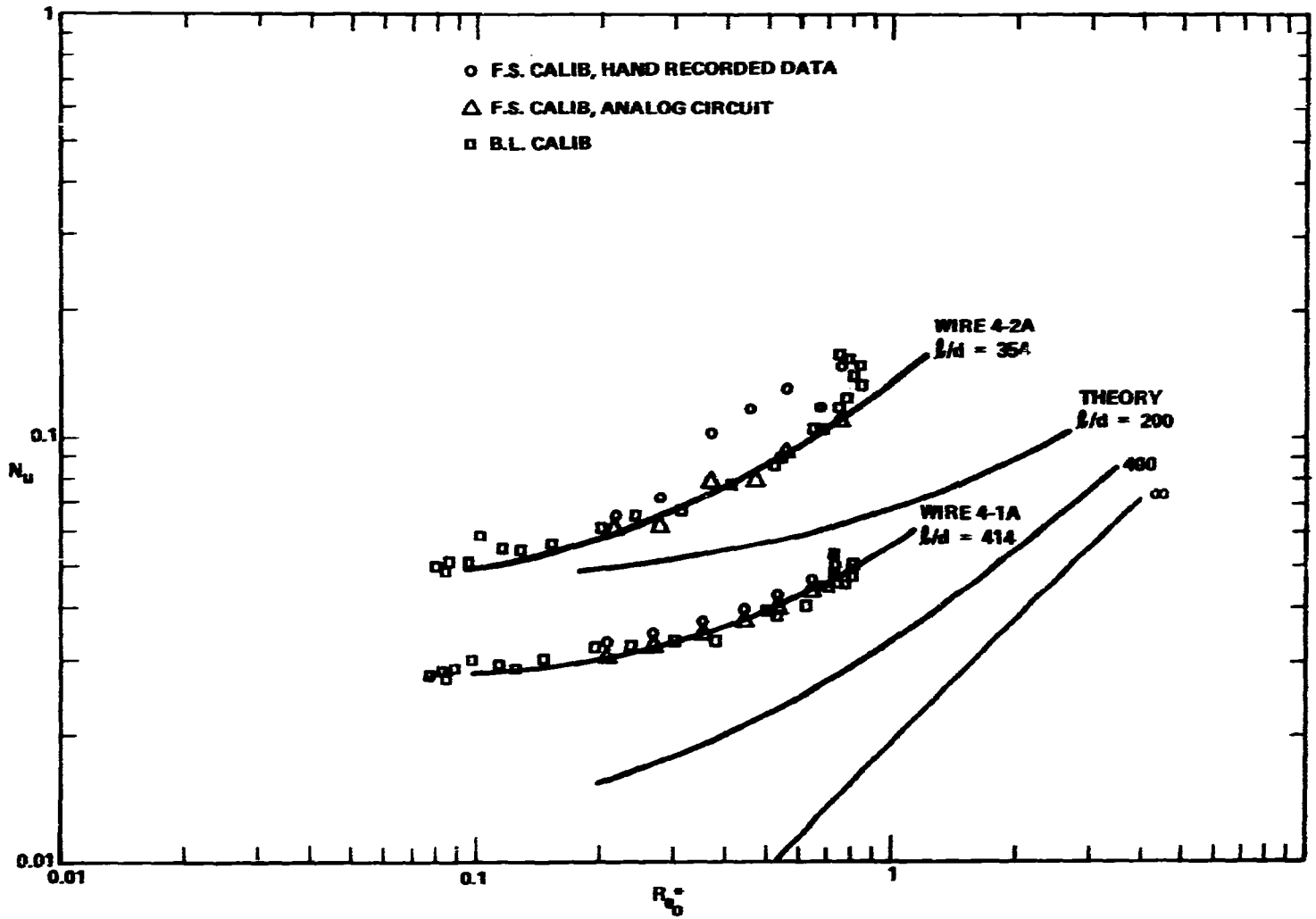

FIGURE 37. NUSSELT NUMBER - REYNOLDS NUMBER CALIBRATION FOR X-PROBE NO. 4.

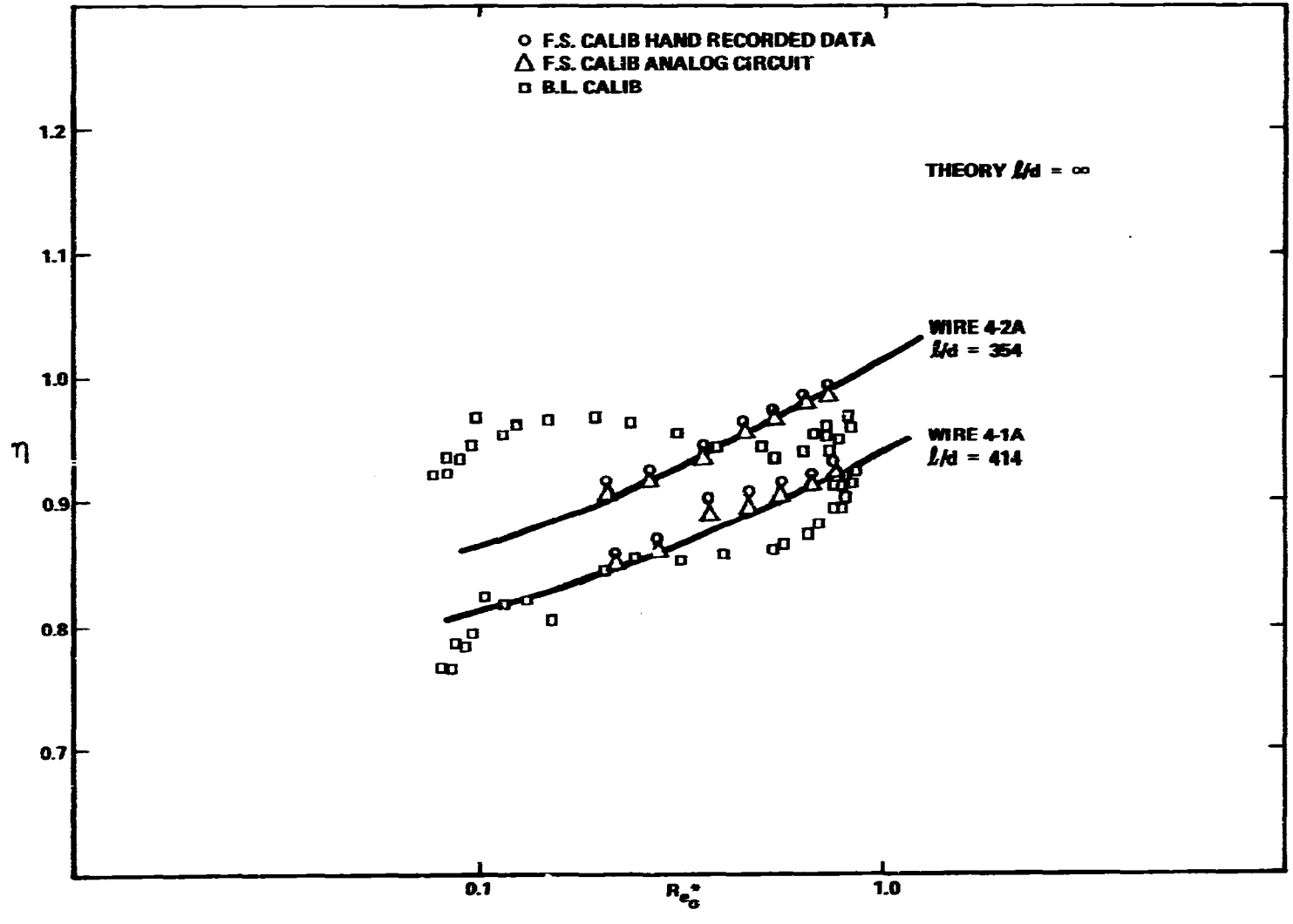

FIGURE 38. RECOVERY FACTOR - REYNOLDS NUMBER CALIBRATION FOR X-PROBE NO. 4.

SECTION VI

THE NEAR WAKE OF A CONE

6.1 SUMMARY OF PREVIOUS WORK

The motivation, experiment design and test results on the mean flow for the near-wake experiments have already been reported in Reference 5 (pp 3-44). A summary of these will be given in the present section.

The near-wake study requires the measurement of the mean and turbulent flow in the near-wake of a slender cone. Since theory (Reference 18) expects the major effects to depend on Reynolds, rather than on Mach number, the experiment is done in the Mach 3.0 flow of the Philco-Ford Supersonic Wind-Tunnel. Accordingly, after examination of various model-suspension schemes, a 5-degree half-angle cone with a one-inch base diameter was suspended in the test section by wires. A "trip" consisting of a O-ring provides early transition in the model boundary-layer, at the same time giving an acceptably thin layer at the shoulder ($\delta/D \simeq 0.08$). It was found that the tripped boundary-layer profiles were very similar to those of a naturally-turbulent (untripped) layer, so that the trip can be considered equivalent to a Reynolds number increase.

Much effort was devoted to the choice of number, size and location of the wire supports. A total of seven wires were finally used in a way allowing their added use for pitch and yaw control. Although the presence of each wire could be detected by a sensor in its wake, the effect of the supports on the cone wake itself was judged minimal. This conclusion was arrived at by first making measurements of the cone base pressure P_b, the location x_n of the "neck" and the wake thickness d_w. The magnitude of P_b, x_n and d_w so found agrees very well with those of tests done elsewhere, including tests with magnetically-suspended bodies.

Special pitot and static-pressure probes were constructed and were satisfactorily checked for insensitivity to pitch and yaw effects. A complete "matrix" of mean-flow data were taken with these probes for the conditions of Figure 39. The data were collected by an automated system producing IBM cards in real time, and were reduced to give the local mean velocity, temperature, pressure, density, total temperature and Mach number at each point; the relevant computer programs are called WEM-I and WEM-II. A limited-distribution report (Reference 19) has been issued which contains plots of all the mean quantities for the conditions of Figure 39. Examples of these are also shown in Figures 16, 21 and 22 of Reference 5. The major conclusions drawn from the work of the preceding period, as described just above, were:

(1) The experiment design goals were met: the test conditions ranged from the so-called "pre-BLT" condition (laminar boundary-layer, at $Re_{\infty,D} = 69{,}000$) to the "post-BLT" conditions (turbulent layer, $Re_{\infty,D} > 100{,}000$).

(2) The initial conditions (i.e., the boundary-layer profiles) at $x = 0$ were normal.

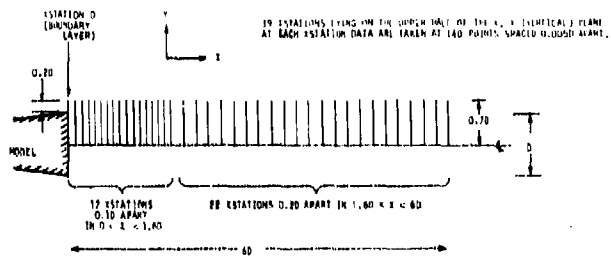

2. CONDITIONS: $M_\infty = 3$, REYNOLDS NUMBERS AS FOLLOWS:

EXPERIMENT NO.	$Re_\infty \cdot D$
A	176,000
B	152,000
C	127,000
D	106,000
E	81,000
F	69,000

3. TYPES OF MEASUREMENTS: MEAN FLOW: PITOT TUBE
STATIC PRESSURE PROBE
HOT-WIRE ANEMOMETER
TURBULENCE: HOT-WIRE ANEMOMETER

FIGURE 39. EXPERIMENT MATRIX FOR THE WEM (NEAR WAKE) TESTS.

(3) The wake velocity and temperature showed distinct changes from the pre-BLT to the post-BLT conditions.

(4) There were substantial pressure gradients in $x < 6D$; the peak pressure is encountered beyond the neck.

(5) The wake diameter increases with x for pre-BLt but is constant for post-BLt.

6.2 FURTHER REDUCTION OF THE MEAN-FLOW DATA

In the present reporting period the mean-flow data reported in last period's report (Reference 5) were further put into a form suitable for comparison with theories and other experiments and for use as generalized "rules" in flight applications. This was done by computer program DRB3E(WEM-III). An outline of these operations will be given below.

To test whether the wake approached gasdynamic equilibrium the wake radial coordinate y was transformed into the Howarth distance

$$\tilde{y} = \left[2 \int_{y=0}^{y} \frac{\rho}{\rho_e} y \, dy\right]^{\frac{1}{2}} \tag{6.1}$$

where ρ is the local density and ρ_e the density just external to the wake, at a distance y_e from the axis; the y_e was determined by inspection of the radial profiles from Reference 19. Using the velocity u_e and temperature T_e at y_e, the velocity and temperature "defects"

$$w \equiv \frac{u_e - u(y = 0)}{u_e}, \qquad \theta \equiv \frac{T(y = 0) - T_e}{T_e} \tag{6.2}$$

were also computed. Next, the wake drag was computed from the data as follows. It is known that the drag integral at each fixed distance x behind the cone is given (Reference 20, p. 93) by

$$S \equiv \text{wake drag} = S_1 + S_2 = \text{viscous drag} + \text{pressure drag}$$

$$S_1 = 4\pi \int \frac{\rho u}{\rho_e u_e} \left(1 - \frac{u}{u_e}\right) y \, dy = S_1(x) \tag{6.3}$$

$$S_2 = \frac{4\pi}{\gamma M_e^2} \int \left[\frac{P}{P_e} - 1\right] y \, yd = S_2(x) \tag{6.4}$$

The integration limits for the viscous drag S_1 are, obviously, $y = 0$ and y_e. The choice of limits is not so clear for the pressure drag S_2. If the upper limit extends beyond the cone's bow shock then S is bound by the total drag of the cone rather than the wake drag. On the other hand, S_2 cannot be completely ignored since $P \neq P_e$, i.e., substantial pressure gradients exist, as shown on Figure 21 of Reference 5. A reasonable compromise was chosen by computing the pressure drag only within the wake boundary y_e; therefore, the limits $y = 0$ and $y = y_e$ were also chosen for the S_2 integral. (Actually, both S_1 and S_2 are separately computed and displayed in the program.)

With the defects w and θ and the drag S(x) known at each x, the wake characteristic length L (the "traverse" scale) was computed:

$$L(x) = \left[\frac{S}{4\pi w} \right]^{\frac{1}{2}} \tag{6.5}$$

The similarity parameter $\eta \equiv \tilde{y}/L$ (i.e., the non-dimensional, "compressible" radial distance) was also computed as well as the non-dimensional velocity and temperature:

$$\tilde{u}(x,y) = \frac{u_e - u}{u_e - u(y = 0)}, \qquad \tilde{T}(x,y) = \frac{T - T_e}{T(y = 0) - T_e} \tag{6.6}$$

The corresponding non-dimensional axial distance is

$$\bar{x} = \frac{x}{\sqrt{S}} \tag{6.7}$$

Finally the DRB3E program computes the usual transport coefficients:

"Turbulent Reynolds Number" $\quad R_T = 6\pi^{1/2} w^{3/2} \bar{x}$ (6.8)

"Turbulent Prandtl Number" $\quad \sigma_T = \dfrac{\hat{\theta}}{0.4 M_e^2 w}$ (6.9)

as well as the Reynolds number $\quad Re_w = \dfrac{(u_e - u(y = 0))L}{\nu_e}$ (6.10)

where M_e and ν_e are the Mach number and laminar kinematic viscosity just outside the wake.

In addition, calculations of the cone drag budget (see Appendix C) and of the integral thicknesses of the boundary-layer were made in order to characterize the wake for proper placement in the evolving matrix of laboratory and flight data.

6.3 RESULTS OF THE MEAN FLOW MEASUREMENTS

6.3.1 CHARACTERIZING PARAMETERS

The significance of the present tests lies heavily on the ability to demonstrate the regularity of the wake initial conditions and the capacity of these conditions to generate meaningful turbulent near-wake phenomena. Furthermore, parameters such as the cone drag, the momentum Reynolds Number R_θ, etc., must be known in order to match them with the observed turbulent behavior. The following measurements are important in this respect:

(a) As already mentioned in Subsection 6.1 and demonstrated in p. 37 of Reference 5, the boundary-layer profiles conform to the expectations for all test conditions (e.g., both for pre- and post-BLT conditions).

(b) The boundary-layer momentum thicknesses R_θ were computed from the measured profiles at the cone base as follows:

EXPERIMENT DESIGNATION	TUNNEL PRESSURE P_o (mm Hg abs.)	CONE REYNOLDS NO. ($Re_{D,\infty}$)	θ (inch)	R_θ	δ^* (inch)
A	730	178,000	0.0064	1,140	0.0322
B	630	152,000	0.006	910	0.0325
C	530	127,000	0.0069	875	0.0314
D	430	106,000	0.0069	730	0.0296
E	330	81,000	0.0045	365	0.017
F	280	69,000	0.0042	290	0.015

In this table we see that the computed R_θ's confirm a posteriori the transition threshold observed: that is, the A-D experiments (P_o > 330 mm Hg abs.) were observed to have a clearly turbulent (post-BLT) boundary-layer, which could have been predicted also because their R_θ's are greater than a few hundred. Note, also, that the "most turbulent" test condition produced (Experiment A, P_o = 730 mm Hg abs.) involves an R_θ = 1,140, which is probably much smaller than the R_θ encountered in flight. This point is important, because R_θ is a measure of the "maturity" of the boundary-layer. The present thinking is that above a certain R_θ most boundary-layer properties are Reynolds-number-independent.

(c) Another useful "benchmark" in the present tests is that, beyond a certain distance behind the cone the wake properties should tend toward the familiar "far wake" behavior:

$$w \sim \theta \sim \bar{x}^{-2/3} \tag{6.11}$$

Also, we expect the radical variations $\tilde{u}$ and $\tilde{T}$ (i.e., Eqns. (6.6) to fall into a Gaussian shape, that is

$$\tilde{u} \sim e^{-k\eta^2} \; ; \quad \eta \equiv \tilde{y}/L \quad ; \quad k = \text{const.} \tag{6.12}$$

with corresponding asymptotic formulas for the turbulence properties. These relations are expected to hold not only on theoretical grounds (Reference 21) but also because they were found valid during the earlier, ARPA-sponsored studies at Philco-Ford of the axisymmetric, far-wake behavior at Mach 3 (References 22 and 23 for example). We therefore shall be especially careful to recognize in the presentation of results below (Subsection 6.3.3.b) the relaxation process which will turn the near-wake behavior into the far-wake behavior. Naturally, since the present results stop at $x/D = 6$, this asymptotic behavior may not be fully attained. Any semblance of a trend, however, will reinforce the conviction that the present flow field begins (as discussed in Subsection 6.3.3 referring to the boundary-layer) and ends with familiar flow profiles.

6.3.2 EXPECTATIONS FROM INTUITION AND FINSON'S THEORY

Before the mean-flow results are presented, the expectations of the near-wake behavior, especially as enunciated by Finson (Reference 18) will be discussed briefly. Such a discussion is needed for comparison with the present experimental results to see if the present basic ideas for near-wake formation are valid. In this section Finson's predictions will be simply referred to as the "theory".

The theory is basically an extension of intuitive thinking about the relaxation process connecting the boundary-layer at the shoulder and the far wake. It says that the small-scale turbulence shed by the body boundary-layer persists for some dozens, perhaps hundreds, of (drag) diameters behind the vehicle without deterioration provided that its "turbulence Reynolds Number"

$$Re_{\Lambda} = \frac{u'\Lambda}{\nu} \tag{6.13}$$

is much higher than about 40 in the near wake. With small scales dominating, the large-scale motion characteristic of a typical turbulent wake cannot develop. Thus the familiar "eddy viscosity" is also smaller, the spreading of the wake is inhibited and the "wake velocity" decays very slowly. This creates a "plateau" in the w versus $\bar{x}$ plot, whereby the wake velocity is nearly constant for as long as the small scales persist.* Support for this theory comes mainly from ballistic

* Finson's theory provides some targets for the present research but is neither a precise nor a unique explanation of the "velocity plateau".

range photographs which show clearly the predominance of the small scale in the post-BLT condition.

Some features of the theory which the present research is in a position to prove or disprove are as follows:

(a) Velocity "plateaus" occur only past boundary-layer transition.

(b) The dominant turbulence in the near wake comes from the vehicle boundary-layer (provided that the Re_Λ is not greatly decreased at the shoulder expansion so that "anti-transition" occurs).

(c) The near-wake turbulence consists of scales smaller than the wake itself would generate.

(d) The bulk viscosity of the small-scale near-wake is decreased below the turbulent value, although it is still much higher than the molecular viscosity.

(e) "Regular" wake behavior sets in only after dissipation or diffusion of the small-scale structure (presumably at large x/D).

(f) The above effects are accentuated as the flight Reynolds number $Re_{\infty,D}$ increases.

(g) The above effects can occur at virtually any Mach number.

6.3.3 THE MEAN-FLOW PROPERTIES

a. Wake Drag Variation. As explained in Section 6.2, the non-dimensional distance $\bar{x}$ behind the model requires knowledge of the viscous drag. In Appendix C a detailed theoretical estimate of the cone drag is made, using textbook rules for laminar and turbulent skin friction. The result is a relation between the "effective drag diameter" $(C_DA)^{\frac{1}{2}}$ and the actual cone base diameter D. If the total (viscous and inviscid) drag is considered, then

$$(C_DA)^{\frac{1}{2}}/D = 0.34 \tag{6.14}$$

However, the theoretical rules of wake behavior demand the usage of the "viscous" (or "wake") drag diameter which is estimated in the Appendix to give

$$(C_DA)_w^{\frac{1}{2}} = 0.15D \tag{6.15}$$

in the turbulent (post-BLT) case of P_o = 730 mm Hg and

$$(C_DA)_w^{\frac{1}{2}} = 0.14D \tag{6.16}$$

for the laminar case.

These estimates can be now compared directly with the experimental data on Figure 40. The points on this figure are computed from the data according to Eqns. (613) and (614). Indeed, despite the scatter, the points clearly tend toward the viscour drag estimates. As for the initially higher values of $(C_DA)_w^{\frac{1}{2}}$, it is likely that this is simply an initial misjudgement of the integration limits in Eqns. (613) and (614).

b. Wake Centerline Variation. The wake centerline velocity is given by w defined in Eqn. (612), and the data on this quantity are shown on Figure 41. At the lowest pressure (F experiment, P_0 = 280 mm Hg) for which the boundary-layer on the model is laminar but where transition occurs at $x/D \simeq 3$, $w(\bar{x})$ has definitely began following the far-wake data at $\bar{x} \simeq 30$ (i.e., at 6 cone base diameter, which is about 3D downstream of wake transition). As one proceeds towards the post-BLT condition (towards the A conditions) $w(\bar{x})$ departs from the far-wake behavior systematically. In the A condition the $w(\bar{x})$ at $\bar{x} = 35$ is nearly twice as large as in the pre-BLT condition. Furthermore, if one notes carefully the WEM-A, WEM-B and WEM-C data (top three plots on Figure 41) one can detect a continuing increase of w as the pressure increases. Therefore it appears that an increase in $Re_{D,\infty}$ increases w (at fixed $\bar{x}$) first because it causes transition in the body layer, and subsequently by an additional mechamism. One may say that the "more mature" the turbulent boundary layer, the higher the $w(\bar{x})$. Also, note that w is unity at $\bar{x}$ = 3 and decreases abruptly shortly afterwards. This happens because of the drag-swallowing immediately after the neck. The above conclusions verify the theoretical points (a) and (f) (Subsection 6.3.2). Of course, a persistent, flat "plateau" is not observed, perhaps because the Reynolds number is not high enough.

c. Viscosity Variation. The theory predicts that in the post-BLT condition the fluid viscosity is reduced considerably below the turbulent level, although it remains equally superior to the laminar (molecular) level. Figure 41 already constitutes one indirect piece of evidence that this is so, by showing the expected increase in $w(\bar{x})$ in the post-BLT case. Furthermore, according to the far-wake similarity analysis (e.g., Reference 23) the velocity defect $w(\bar{x})$ can be expressed in terms of the eddy viscosity $\bar{\nu}_T$ as follows:

$$w(\bar{x}) = \frac{1}{\pi^{1/3}} (R_T/6)^{2/3} \bar{x}^{-2/3} \tag{6.17}$$

where R_T turbulent Reynolds number $(u_e - u(0))L/\bar{\nu}_T$.

Since $(u_e - u(0))$ and L can be expressed in terms of $(C_DA)^{\frac{1}{2}}$ (see Eqns. (615) and (6.7)), it follows from Eqn. (6.17) that

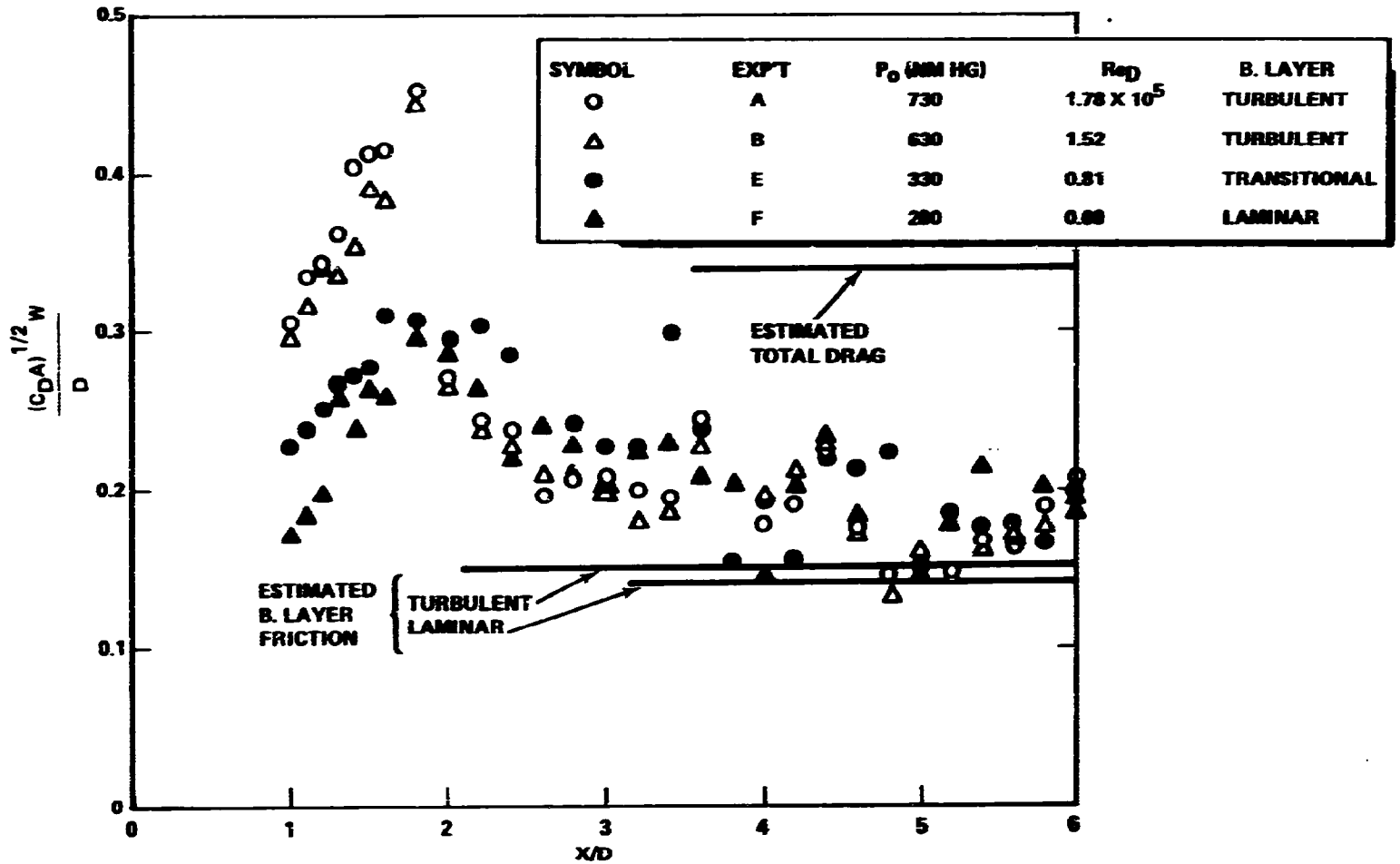

FIGURE 40. MEASURED DRAG OF THE NEAR WAKE.

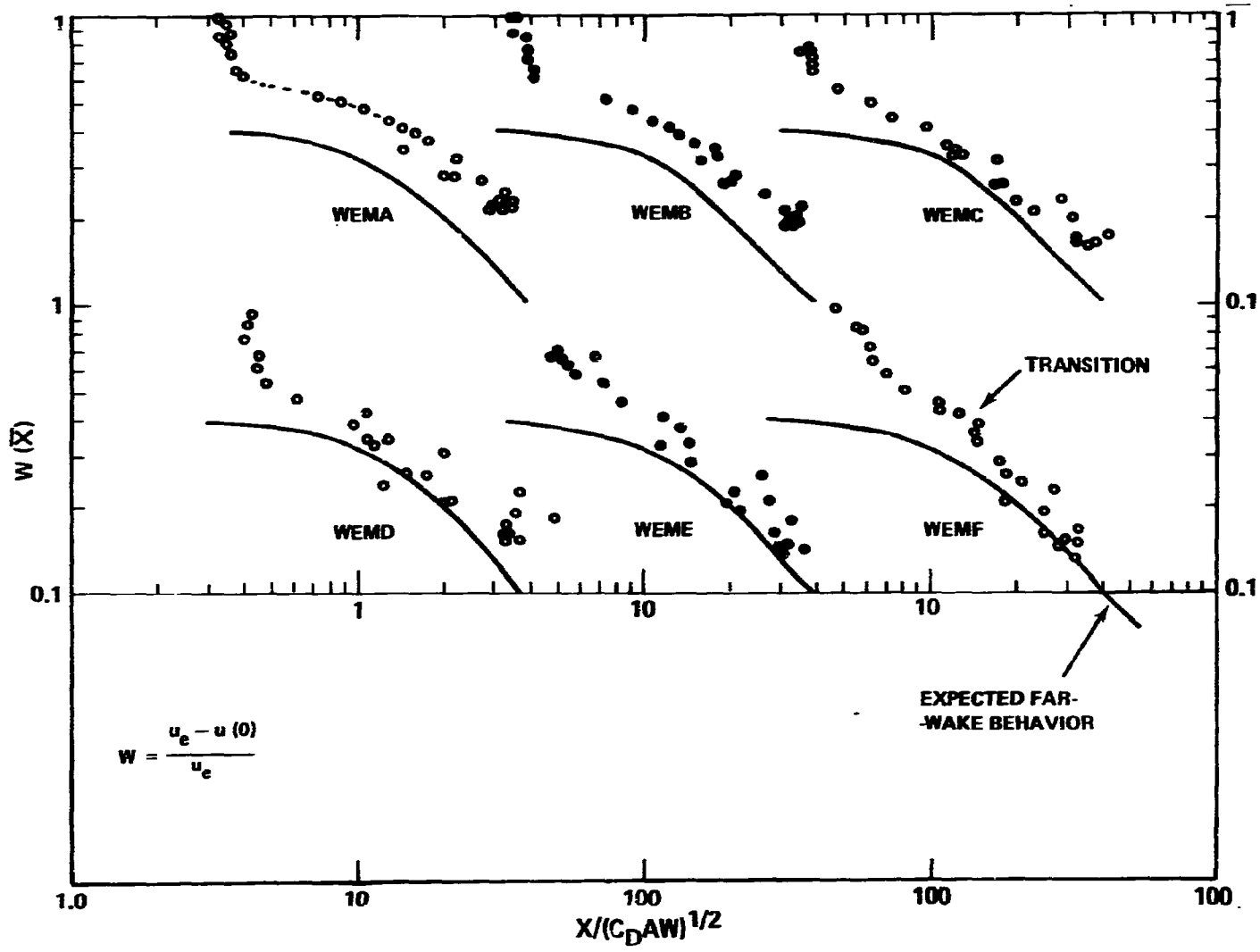

FIGURE 41. VARIATION OF WAKE VELOCITY DEFECT ON NEAR-WAKE AXIS WITH Re_D SOLID CURVE IS FROM FAR-WAKE EXPERIMENT.

$$\bar{\nu}_T = \text{const.} \frac{1}{w\bar{x}} (C_D A)_w^{\frac{1}{2}} \tag{6.18}$$

A calculation of $\bar{\nu}_T$ has been made using the experimental data of w, $\bar{x}$ and $(C_D A)_w^{\frac{1}{2}}$, the latter as shown on Figure 40. The results are shown on Figure 42. It is abundantly clear that the bulk kinematic viscosity $\bar{\nu}_T$ decreases substantially from the pre-BLT to the post-BLT case, in the farther end of the wake. Since the pre-BLT wake becomes turbulent (and presumably coarse-scaled) beyond about 3D, this implies that the presence of shed boundary-layer turbulence has produced the decreased viscosity, as theory would have it.

Figure 42 shows that whereas the "regular" ν_T is of the order 150-200 c.g.s. units, the decreased level due to the small-scale structure is of order 50-100 c.g.s. units. A rough calculation of the expected laminar value gives 1-10 c.g.s. units. Thus the small-scale turbulence brings $\bar{\nu}_T$ down but still keeps it substantially higher than the laminar level. Finally, the relation among these various levels can be checked by additional existing data. From the computation performed of the "wake Reynolds number" $Re_w = (u_e - u(0))L/\nu_e$ (see Eqn. (6.10)) we typically find $Re_w \simeq 1000$ for the pre-BLT case. Thus the ratio of molecular-to-eddy viscosities $\nu/\bar{\nu}_T$ is

$$\frac{\nu}{\bar{\nu}_T} = \frac{R_T}{Re_w} \simeq \frac{15}{750} \simeq \frac{1}{50} \tag{6.19}$$

which compares well with the number quoted above in c.g.s. units.

d. <u>The Turbulent Prandtl Number</u>. Although not of direct importance to the theory insofar as the type of wake structure is involved, the Prandtl number σ_T controls the predicted fluid temperature θ in the wake through the familiar formula

$$\theta = \sigma_T(\gamma - 1) M_e^2 w \tag{6.20}$$

The σ_T has been computed from the data and is shown on Figure 43. It tends asymptotically in all cases to the well-established level of about 0.85 characteristic of axisymmetric flow (Reference 23).

e. <u>Radial Profiles of Velocity and Temperature</u>. Eventually, any predictive theory of the near wake will either assume or predict the radial velocity $\tilde{u}$ and temperature $\tilde{T}$ variations. It is usually expected that the post-BLT wake will have rather novel variations of this type. The data, as computed from Eqn. (6.6) and presented on Figures 44 and 45, however, show that $\tilde{u}$ and $\tilde{T}$ are, in fact, quite "Gaussian". The solid lines shown are the self-similar variations

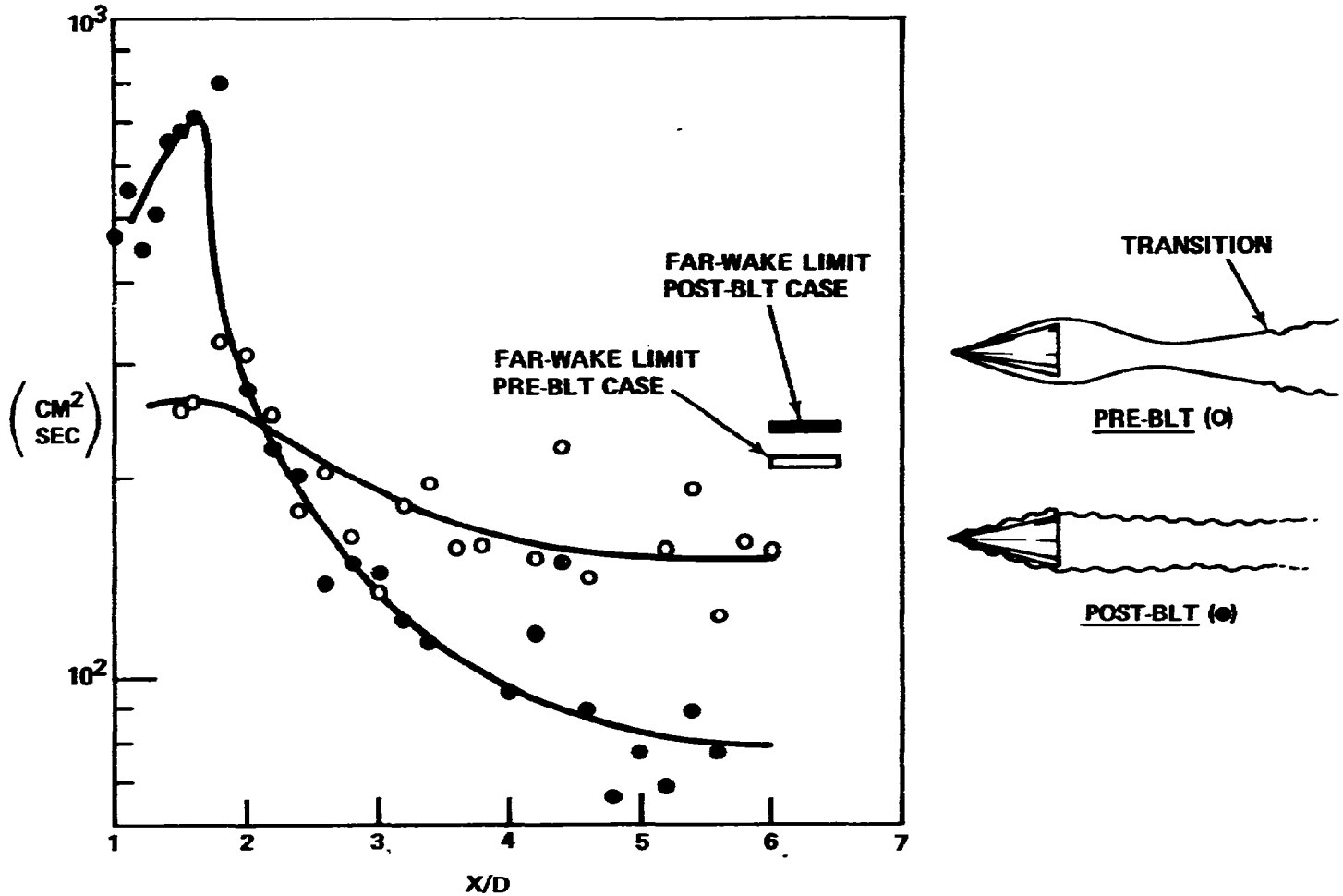

FIGURE 42. EDDY KINEMATIC VISCOSITY MEASURED IN THE NEAR WAKE.

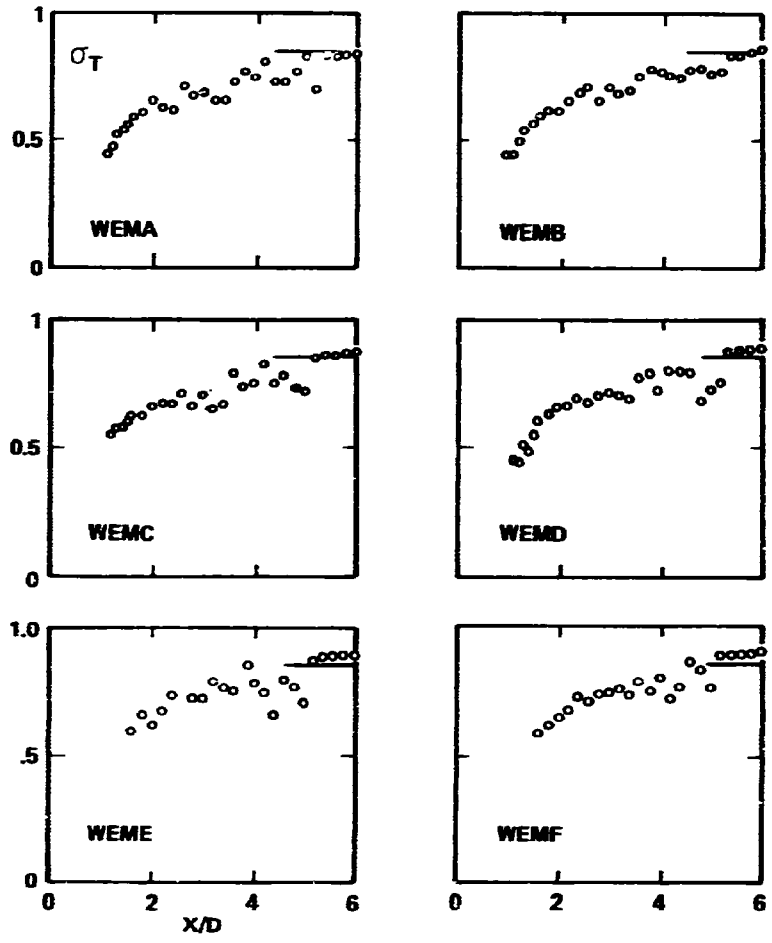

FIGURE 43. VARIATION OF THE TURBULENT PRANDTL NO. σ_T ALONG NEAR WAKE AXIS FOR EACH Re_D. STRAIGHT LINE IN EACH GRAPH IS THE FULLY-TURBULENT WAKE EXPECTATION (σ_T = 0.84).

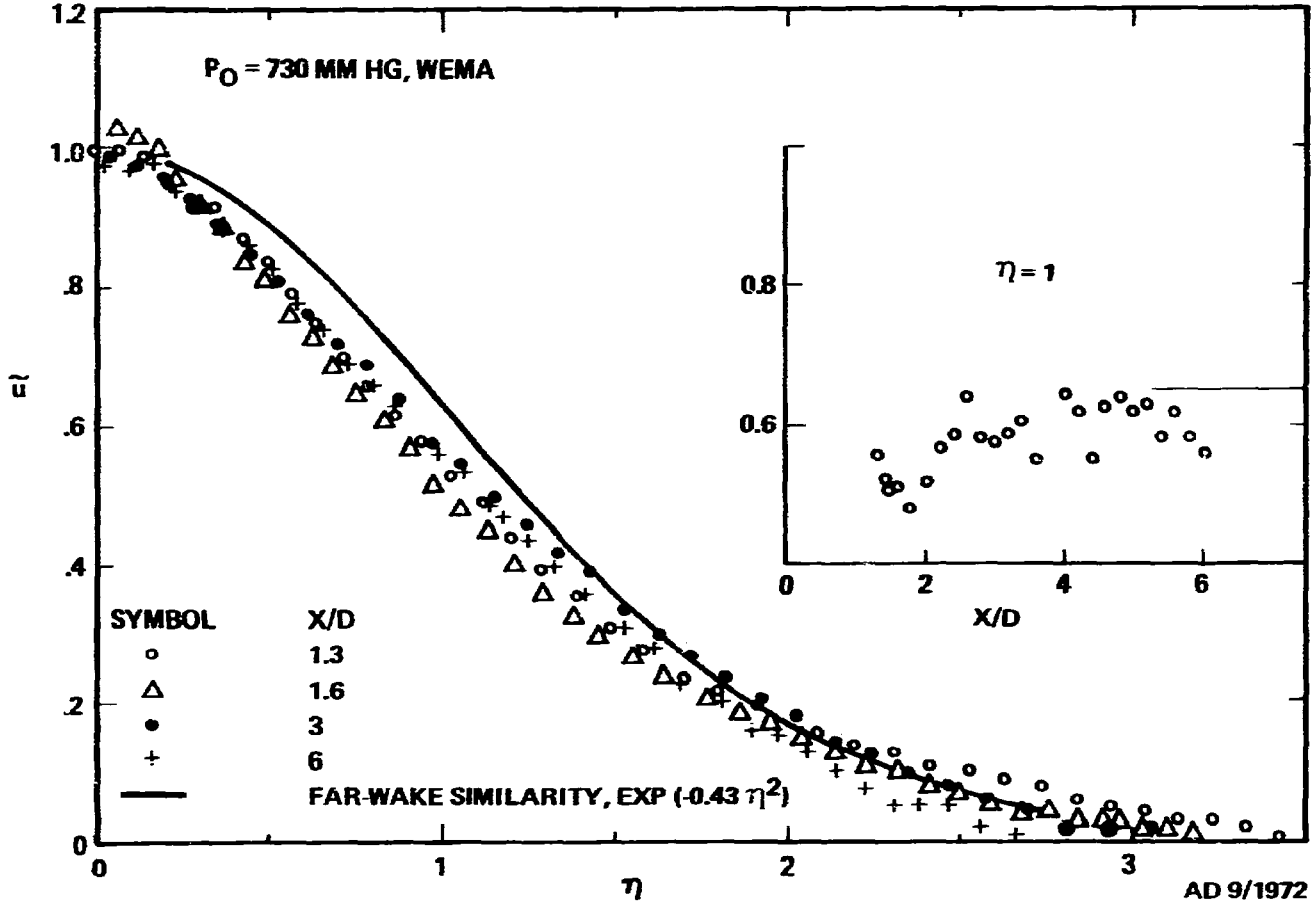

FIGURE 44. RADIAL VARIATION OF NON-DIMENSIONAL LONGITUDINAL VELOCITY IN THE NEAR WAKE (HIGHEST-Re_D TURBULENT BOUNDARY LAYER).

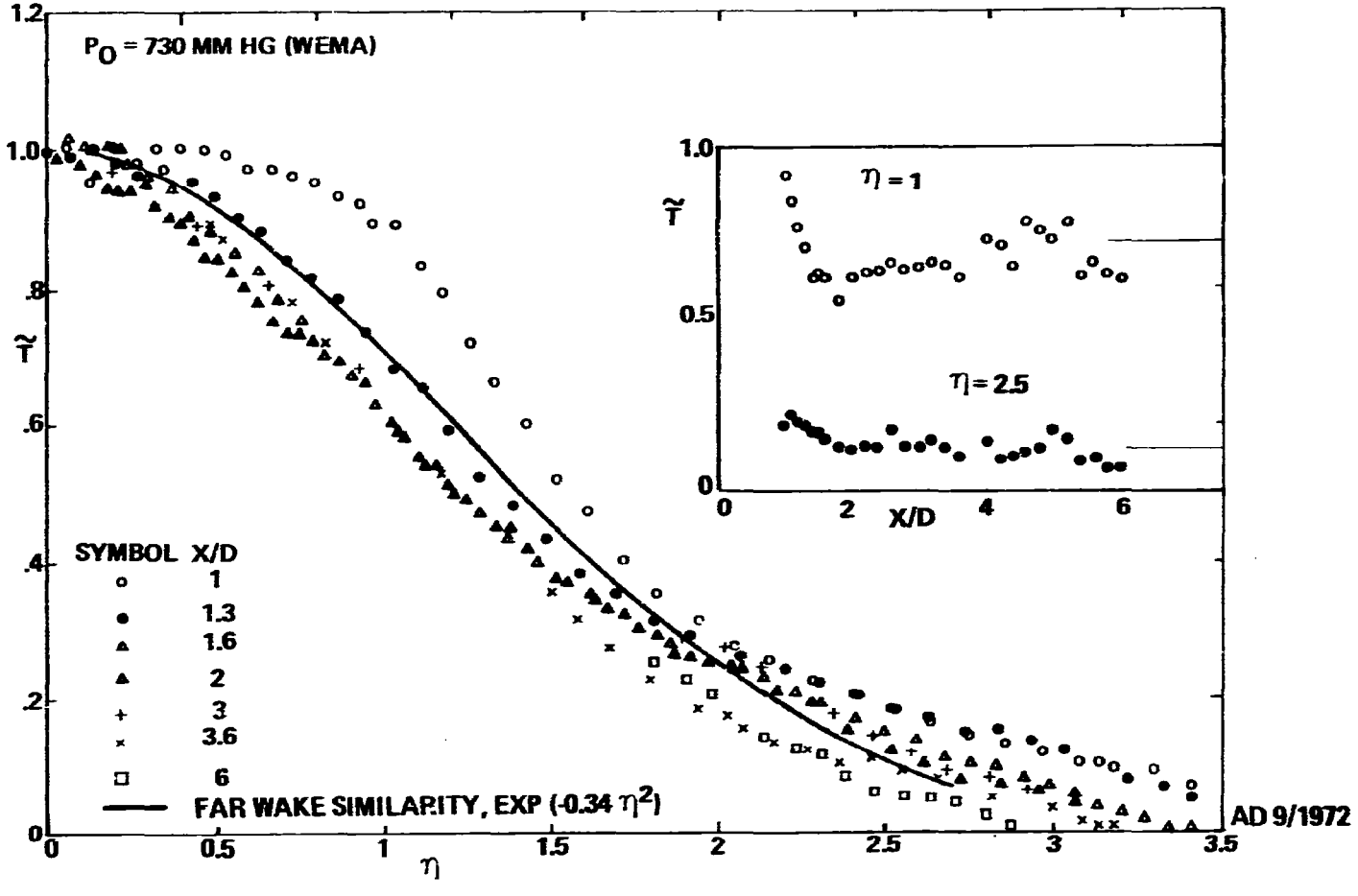

FIGURE 45. RADIAL VARIATION OF NON-DIMENSIONAL STATIC TEMPERATURE IN THE NEAR-WAKE (HIGHEST-Re_D TURBULENT BOUNDARY LAYER

$$\tilde{u} = e^{-0.43\,\eta^2}, \qquad \tilde{T} = e^{-0.34\,\eta^2} \tag{6.21}$$

which were found by Philco-Ford in the far wake (Reference 23). It is quite surprising that the data actually reaches this behavior almost immediately after the "neck" (e.g., at $x = 2D$); the "bulge" at $\eta > 2$ is due to the shed boundary-layer.

6.4 TURBULENCE PROPERTIES

6.4.1 METHOD OF COLLECTING THE DATA

a. Principle. We are interested in mapping, first, the axial and radial distribution of the velocity and temperature/density fluctuations, and secondly, the distributions of the integral scales of the longitudinal velocity and temperature fluctuations. The principle of measuring the fluctuation intensities is as follows. The hot-wire is positioned at the desired point in the wake and its wideband rms output e and mean voltage drop V are measured at each of a number of electrical heating currents i. The shape factors of the curve defined by the plot e/V versus i gives the desired fluctuation magnitudes. For the scale measurement, one invokes Taylor's hypothesis that the scale can be extracted from the measurement of the power spectrum $e^2(f)$:

$$\Lambda \sim \frac{e^2(f = 0)}{e^2} \tag{6.22}$$

where $e^2(f = 0)$ is the spectral density at zero (or very low) frequency and e is the wideband fluctuation already measured above. Therefore one can simply measure $e^2(f = 0)$ at that point and combine it with the e already measured to come up with the scale length. We shall now give a somewhat more detailed description of how this is done in the laboratory.

b. Description of Measurement (Refer to Figure 46). At each pressure a number of positions (x stations) are chosen for study. Normally these positions are in increments of 0.2D starting at $x = 0$ (that is 0, 0.2, 0.4,.....1.4, 1.6) up to $x = 1.6D$; then, in increments of 0.4D from 2D to 6D (i.e., 2, 2.4,.....5.6, 6). At each x data are then taken in the radial direction at points spaced 0.005D apart, beginning with point y_o and ending with point y_e. Typically for $x/D > 1.4$, $y_o = 0$ (i.e., the first point is read on the wake axis) and $y_e = 0.395$ D. Nearer the body y_o and y_e are chosen to bracket the active portions of the flow. For example, at $x = 0$ (i.e., at the plane of the cone base) the measurement starts at $y_o = 0.525D$ (i.e., 0.025D above the cone surface) and continues to $y_e = 0.695D$, i.e., 0.195D above the cone surface.

Data are punched on IBM cards in real time. The hot-wire probe current i is first fixed at the desired value. As the wind-tunnel runs the probe is first located at the desired starting position (say at $x = 2D$, $y/D = 0$) and then a switch is thrown which begins traversing the probe in the radial position at constant speed. Every 0.005D of probe travel a pulse automatically triggers the data-acquisition system

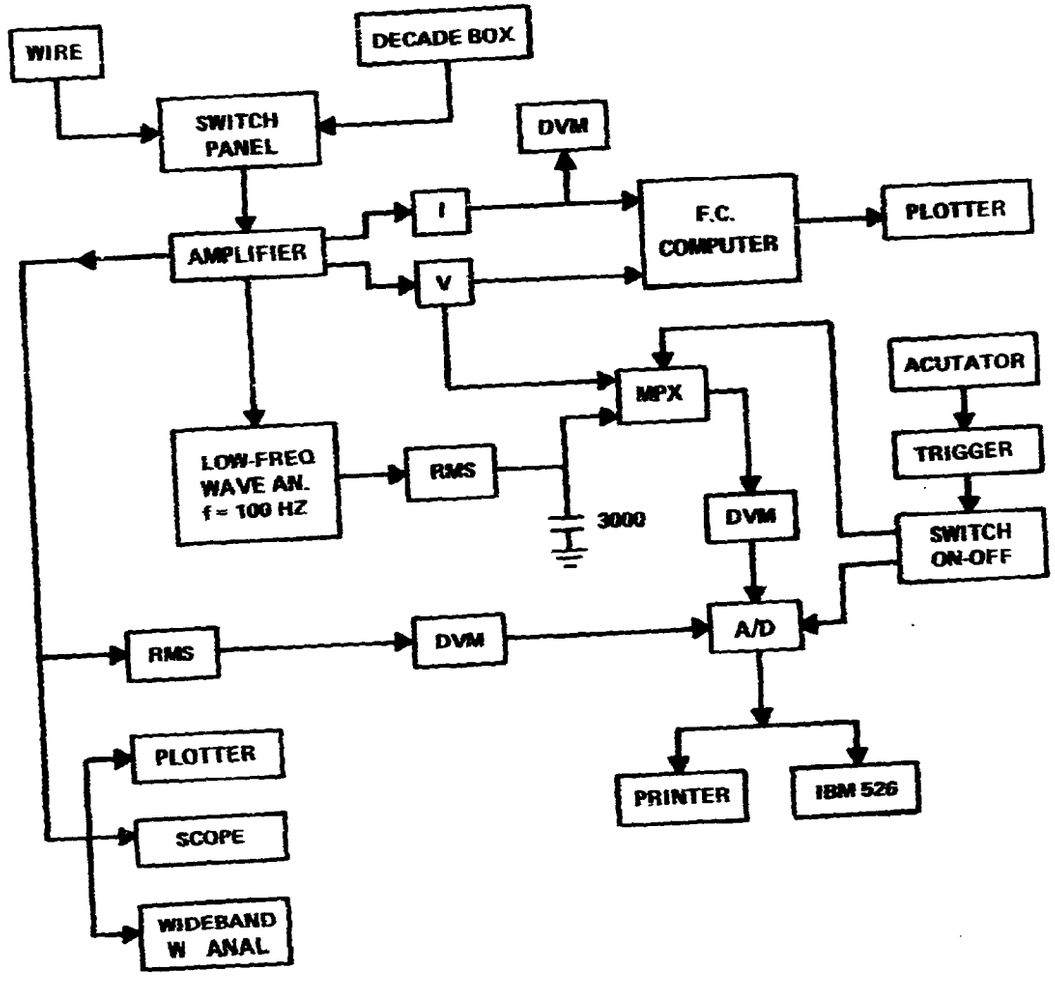

FIGURE 46. DIAGRAM OF ELECTRONIC COMPONENTS USED IN MEASURING THE NEAR-WAKE TURBULENCE.

and a pair of numbers is recorded on IBM cards. At the end of travel (that is, when the data at the end point y_e have been punched) the probe is returned to its starting point y_o, the wire heating current i changed to the next desired level, and the traverse is repeated. When the same path has been traversed for all the desired currents, the probe is moved to another axial x-station, and the process is repeated.

The Philco-Ford A/D conversion system presently has two active channels, meaning that at each point (x,y) only two numbers can be recorded. However, to get both the fluctuation intensities and the scales we saw in the preceding section that we need three measurements, i.e., e, V and $e^2(f = 0)$. To resolve this problem, it was decided to multiplex the data acquisition so that at one point one reads e and V, whereas at the next, one reads e, $e^2(f = 0)$, then back again to e, V, etc. A special multiplexer was built to perform this switching function.

Referring, now, to Figure 46, the hot-wire signal is channeled to an ADP 12/13 Hot-Wire Amplifier, which boosts it to a gain G of 100-500, compensates it for thermal lag and filters its components below 3 Hz and above 1 MHz. The current i of the wire is permanently displayed during the run on a digital voltmeter; the mean wire voltage V is channeled to the multiplexer, as well as to a flow-calibration analog computer (Model ADP-17). During the earlier part of the work the latter was used to produce flow calibrations of the anemometer prior to each measurement (see further discussion of this under Section III.

The a.c. hot-wire signal e is carried to a Hewlett-Packard Model 3400A rms voltmeter, through which it is converted to a d.c. voltage Z with a transfer function t_1 such that e(rms volts) = t_1Z(d.c. volts). Usually the rms meter is set to a 3-V full-scale so that $t_1 = 3$. The output Z is then fed to a Hewlett-Packard Model 3440A Digital Voltmeter (DVM) which is part of the Philco-Ford A/D system. In the meantime the a.c. wire signal e is also channeled to a Hewlett-Packard model 302A Wave Analyzer tuned to a frequency f_o which usually lies between 100 and 250 Hz. It is known that the signals involved are very high in frequency, so that $100 < f_o < 250$ Hz lies well into the low-frequency "flat" portion of the spectrum. Thus f_o can be considered to give the zero-frequency and $e^2(f = 0)$ of the spectrum. The function of the wave analyzer is to filter the wideband signal e with a passband of 7 Hz around f_o (i.e., 3.5 Hz on either side of f_o, with a -3 db drop). The signal passing through this window is then extracted from the analyzer in the form of an a.c. signal e_o with a transfer function J such that

$$e_o(\text{folts rms}) = J\, e_i(\text{volts rms}) \tag{6.23}$$

The transfer function J is usually set at 33.3, so that a 30 mV equivalent (sine wave) input e_i will produce a one-volt e_o. If $e^2(f)$ is the spectral density (i.e., the integral of $e^2(f)$ over f produces the wideband signal e^2) then the equivalent input e_i^2 is $7e^2(f_o)$. Therefore the desired quantity $e^2(f_o)$ is related to the analyzer output e_o^2 by

$$e^2(f_o) = \frac{e_o^2}{7J^2} \tag{6.24}$$

Next, the analyzer output e_o(rms volts) is fed to another Hewlett-Packard Model 3400A rms meter with transfer function t_2 (usually $t_2 = 3$) such that its d.c. output

$$t_2 F(\text{volts d.c.}) = e_o(\text{volts a.c.}) \tag{6.25}$$

Thus collecting the various transfer functions in the sequence, the desired spectral density $e^2(f_o)$ is found from the reading F^2 (or F) by

$$e^2(f_o) = \frac{F^2}{7} \frac{t_2^{\,2}}{J^2} \tag{6.26}$$

The output F is also channeled to the multiplexer. This concludes the description of essential elements in the measuring system shown on Figure 46.

As already mentioned, each traverse begins with the probe poised just before the first y position (i.e., y_o) and the multiplexer set to pass through the V (wire mean voltage) signal. Thus as soon as probe motion begins, the first two numbers punched are V and Z, i.e., the data needed to get the fluctuation magnitudes. The multiplexer next switches to produce the F signal, so that at the second point Z, F are read. The multiplexer alternate switching action continues to the end of the traverse so that one-half of the points read are Z, V and the other half are Z, F data. Thus the fluctuation magnitudes are obtained (from Z, V) at points spaced 2 x 0.005D = 0.010D apart and so are the scales (from Z, F), the two alternating along the traverse. Typically, 80 points are probed along each radius, giving 40-point maps for each of the magnitudes and the scales.

c. Data Reduction Procedure. The turbulence data are reduced with the aid of computer program WEM-IV (DRB4E). The following are notes explanatory to the program, with the sub-heading numbers referring to the similarly numbered program steps (see Appendix D).

(7.3.1) The "current group" refers to the wire heating current, which of course changes from one wire to another.

(7.3.3a) The probes used in the experiment have a line resistance of 1.42 ohm.

(7.3.4) For low overheats, it is known that R is a linear function of i^2: $R = c + c_1 i^2$. However, for higher overheats the variation is quadratic, which explains the presence of the $C_2 i^4$ term.

(7.3.11) The "Reynolds No." quantity printed in the output of the WEM-II program is based on a hot-wire diameter of 0.00001" (ten micro-inches). The wire used in the present (WEM-IV) tests are of 0.00002" diameter, which accounts for the factor of 2 in this step.

(7.3.11a/ 7.3.11e) Originally, the hot-wire was "flow calibrated" in the stream external to the wake so that its Nusselt number Nu dependence on the local Reynolds number Re could be learned. Then, once this "flow calibration" Nu = Nu(Re) was known the Reynolds number from step (7.3.11) was used to find Nu at every point of measurement; from this Nu and the Nu = Nu(Re) relation the quantities $(\partial Nu/\partial Re)(Re/Nu)$, etc., were computed for use in the sensitivity coefficients (Reference 17). However it was found that the radial Nu profile so computed differed from that found by a direct measurement Nu_m of the Nusselt number in the wake:

$$Nu_m = \frac{\alpha_o R_o}{\pi \ell} \frac{1}{k} \frac{C}{C_1} \times 10^{-6} \qquad (6.27)$$

where the quantities on the right are actually measured at each point. It was furthermore found that if Nu was used instead of Nu_m, the turbulence results were suspect and varied greatly from one wire to another (for example, the cross-correlation coefficient $r_{\sigma T}$ was found to be positive, contrary to all previous experience and all expectations). The situation was rectified by discarding the flow-calibration process entirely in favor of using the Nu_m matched to the local Re from the WEM-II program results. Steps (7.3.11a) to (7.3.11e) in the program, therefore, aim at deriving the values of the Nusselt number and recovery factor from the known hot-wire data at each point. It will be noted that the curve-fit for $Nu_m = Nu_m(Re)$ is linear (step 7.3.11c), since such a linear fit was judged best from the available data, (over the range of the Reynolds numbers used). The recovery factor $\eta \equiv T_{aw}/T_o$ is fitted with a quadratic in Re also as a result of inspection of the available data.*

6.4.2 PRELIMINARY RESULTS OF THE TURBULENCE MEASUREMENTS

A portion of the data matrix has already been covered, and preliminary results from such measurements will be discussed in this Section. It should be noted that the matrix requires "mass-production" of quantitative hot-wire anemometer

---

* In most other experiments conducted at Philco-Ford the Nu-Re curve-fit is of the type $Nu = A + B\sqrt{Re} + C\,Re$. The present linear curve-fit (which essentially sets B = 0) reflects only the present Re range and should not be mistaken as a more general heat-transfer correlation. Also, the recovery factor is presently fitted by $\eta = H_1 + H_2 Re + H_3 Re^2$ because it attains a maximum near Re = 1. This maximum is due to the finite wire length, by which η does not anymore keep increasing as Re is lowered because end losses take over.

data in an unprecedented scale. The data are therefore to be considered tentative since a need for improving the technique has been found to exist in many areas. The discussion will center on Figures 47 through 49.

The first important finding concerns the fluctuation magnitudes $u'/\bar{u}$ and $T'/\bar{T}$ in the cone boundary-layer at $x = 0$, i.e., at the soulder (see Figure 47). The velocity fluctuation $u'/\bar{u}$ decreases monotonically from the wall outwards, while $T'/\bar{T}$ has a peak in the middle of the boundary-layer, reaching $T'/\bar{T} \simeq 0.09$. This behavior is consistent with expectations from Kistler's work (Reference 9) if one assumes no Reynolds number or geometry effect. That is, the present data at $R_\theta = 1.170$ and a cone geometry agree numerically with Kistler's data for a flat plate taken with a much larger R_θ ($\simeq$ 20,000). Thus the near wake of this test begins "normally" at the body shoulder.*

The second noteworthy result is that the velocity fluctuations $u'/\bar{u}$ decay abruptly beyond the shoulder, consistently with the theoretical prediction on the effect of the expansion on the shed turbulence; that is, from a maximum level of about 5 to 6% ($u'/\bar{u} \simeq 0.06$) in the boundary layer, these fluctuations decrease to the 1-2% level. At least to a certain degree this represents the "anti-transition" (re-laminarization) effect by which turbulence vanishes upon a sudden Reynolds number decrease. Now, Finson (Reference 18) remarks that a minimum turbulence Reynolds number Re_Λ of about 35 is needed to guarantee survival of turbulence in the near wake; this threshold number agrees with a general, rough estimate made in Appendix E of this report. The numerical data quoted above imply that some turbulence activity has survived in our near wake. Thus the Re_Λ in our case (Figure 47) must be at least 35 or so in the near wake, and presumably much higher in the boundary-layer (at $x = 0$). Indeed, using u' from Figure 47 (the $x = 0$ case), the corresponding mean-velocity data (from Reference 19) and an estimated $\Lambda = \delta/5$ we compute $Re_\Lambda = 150$ in the boundary-layer. The conclusion, again, is that for the A experiment of our tests, the configuration fulfills the "small-scale structure" requirements envisaged by the theory.

In Figure 47 it is also seen that beyond the shoulder ($x > 0$) the velocity fluctuations become very large toward the bottom of each graph, as soon as the "recirculation region" is entered. Two comments are in order here. First, in the latter region the measurements cannot be accurate since the direction of fluid motion is quite irregular. Secondly, the fluctuations are plotted in terms of $u'/\bar{u}$ where $\bar{u}$ is the local mean velocity; the latter is very small in that region. That is, u' is not necessarily large in itself. The computer program presenting the data of Figure 47 also prints the fluctuations u' and T' normalized with other quantities such as the flight speed u_e, etc. The normalizations u'/u_e, etc., will be discussed in a later report.

---

* The point made here is that the wake initial conditions begin with a "familiar" profile. Since both this test and Kistler's data are at low M_e ($\simeq$ 3), these results leave unanswered the Mach number dependence of the wake initial conditions. Such an answer is forthcoming from the JPL and AEDC tests (see Sections II and III). Also, in Section IV we summarize the state-of-knowledge based on such results.

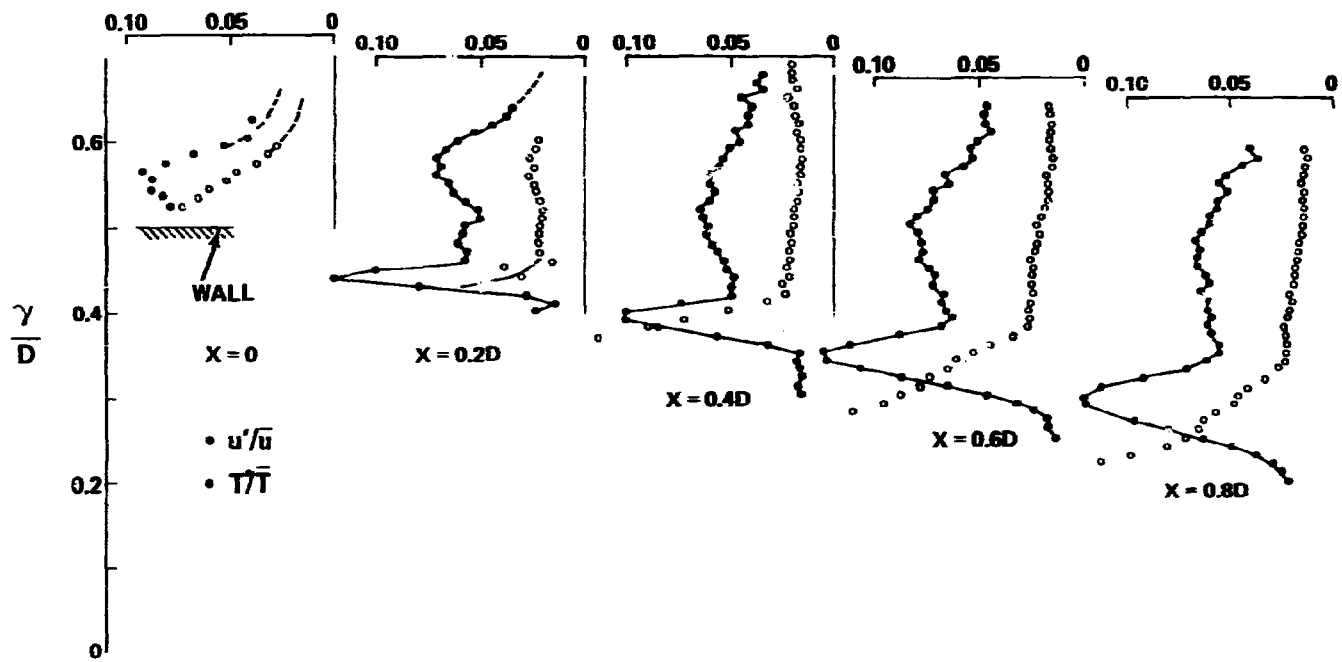

FIGURE 47. WIDEBAND VELOCITY AND TEMPERATURE FLUCTUATIONS IN THE REGION $0 < X < 0.8D$ OF THE TURBULENT NEAR-WAKE (Re_D= 178,000).

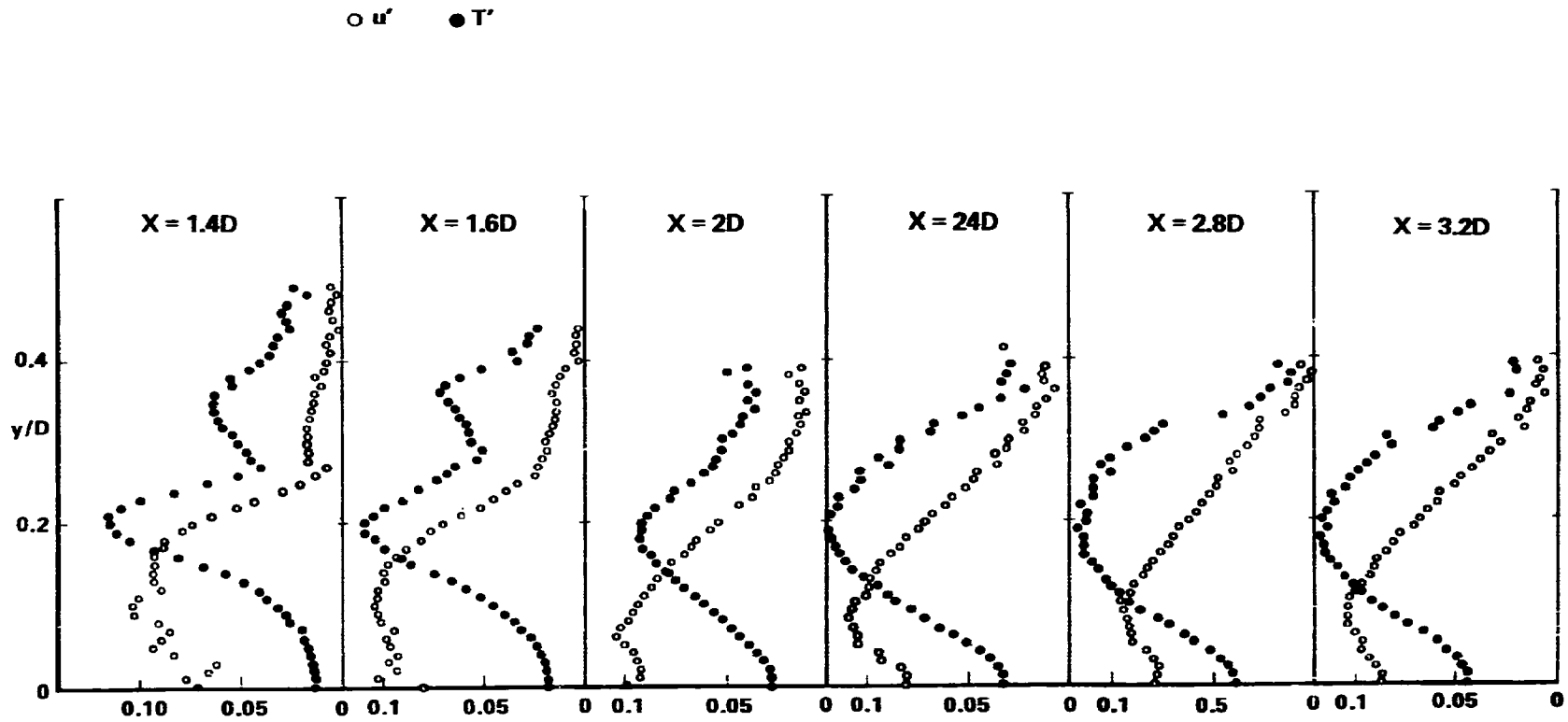

FIGURE 48. WIDEBAND TEMPERATURE AND LONGITUDINAL VELOCITY FLUCTUATIONS IN THE NEAR-WAKE.

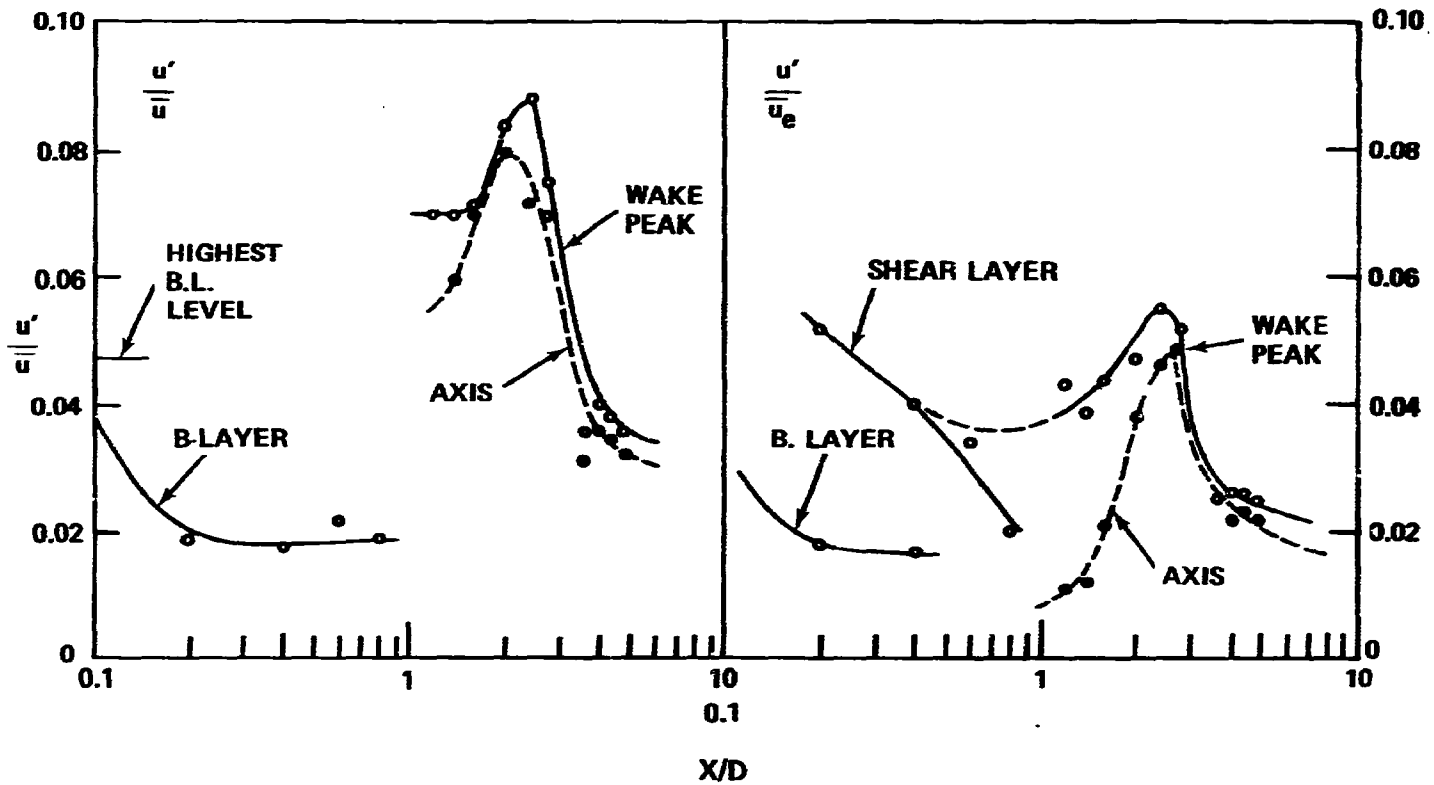

FIGURE 49. VELOCITY FLUCTUATIONS IN POST-BLT NEAR WAKE AS VIEWED IN FLUID AND GROUND-FIXED COORDINATES.

The temperature fluctuation behavior shown on Figure 47 is substantially different from that of $u'/\bar{u}$. The fluctuations $T'/\bar{T}$ are unaffected by the expansion and continue towards the wake neck, at $x/D \simeq 1$, with intensity undiminished at nearly 10% maximum. This result confirms the now-familiar ballistic-range observations showing the fine-grained boundary-layer structure "pouring" into the wake.* Thus, subject to the Re_Λ limitations of this test, it appears that a substantial amount of boundary-layer turbulence continues on into the wake, but that it consists chiefly of temperature/density fluctuations. Qualitatively, this result could have been predicted in advance because of the well-established "Strong Reynolds Analogy" connecting u' and T':

$$\frac{T'}{\bar{T}} = (\gamma - 1)M^2 \frac{u'}{\bar{u}} \tag{6.28}$$

Since the local Mach number M increases upon expansion, the temperature fluctuations $T'/\bar{T}$ increase in a way tending to balance the decreasing $u'/\bar{u}$.

In addition to the peak in $T'/\bar{T}$ of Figure 47 which was just above identified with the boundary-layer remnant, a second peak appears between the remnant and the wake axis. This peak is intense and narrow and is obviously associated with the free-shear layer. Its prominence could perhaps be expected, but the absence of equally intense velocity fluctuations at the same location is puzzling, especially since $u'/\bar{u}$ does not appear like a well-defined "peak" there.

The evolution of the fluctuations $u'/\bar{u}$ and $T'/\bar{T}$ beyond the neck is shown on Figure 48. Just beyond the neck (at $x/D = 1.4$) the boundary-layer remnant and the shear layer can be distinguished from each other. Subsequently they merge into each other, the merging process being complete about 2D beyond the neck (at $x = 3.2D$). Note that there appears, however, to remain a "velocity fluctuation wake" distinguishable from a "temperature fluctuation wake" at $x = 3.2D$. Outwardly, this is evidence of a "double" structure wake whereby strong velocity fluctuations at the core are surrounded by an annulus of temperature fluctuations. In turn, this may be taken as evidence that the wake is formed by (a) the $T'/\bar{T}$ from the remnant (which, as we saw earlier, survives the shoulder expansion) and (b) the $u'/\bar{u}$ contribution from the shear layer. However, judgement on this conclusion should be withheld since the shear layer shows no clear prominence of $u'/\bar{u}$ and because the shear layer already has large $T'/\bar{T}$ (observe the first graph of Figure 48) before it mixes with the remnant. In fact, the double structure of the wake at $x = 3.2D$ is a simple consequence of adiabatic mixing of compressible turbulence as can be seen by re-writing Eqn. (6.28) as follows:

---

* The fact is often overlooked that the ballistic-range photographs show the development of density and temperature fluctuations, not of velocity fluctuations, in the near wake. The interpretation of (velocity) turbulence behavior solely by means of such photographs is therefore quite out of order.

$$\frac{T'/\overline{T}}{u'/\overline{u}} = (\gamma - 1)M^2 = 0.4\,M^2 < 1 \text{ for } M < 1.58$$

Since the axis streamline begins at the neck with M = 0 and increases thereafter, the velocity fluctuations on the axis will be greater than the temperature fluctuations for some distance past the neck, i.e., until M (axis) = 1.58. Furthermore, since M is higher outside the wake the two curves $u'/\overline{u}$ and $T'/\overline{T}$ should cross, which is shown by Figure 48 to occur in practice.

Figure 49 summarizes the tentative fluctuation intensity $u'/\overline{U}$ results. Note the relative roles and intensities of the boundary-layer remnant and of the shear layer. Note, also, that a fluctuation intensity peak occurs in the neighborhood of x/D = 2.5D, reaching 9% of the local velocity $\overline{u}$, and 6% of the external velocity u_e. This peak has also been observed by Gran (Reference 24). However, Gran's observation that the fluctuation maximum occurs on the axis is not borne out by the present results.

SECTION VII

ELECTRON SPACE-TIME CORRELATIONS IN TURBULENT PLASMAS

In the present reporting period the study of the relation between gas temperature and electron density fluctuations in a free turbulent flow has been completed. Most of the effort concentrated on assembling the data collected in previous contract periods, reducing supplementary data when necessary, and collecting the results into a technical report. This report is now under preparation and will be issued soon.

The major findings of this study, abstracted from the report just mentioned, are:

(1) The correlated eddies of the gas temperature tend to be near-spherical structures throughout the turbulent volume, with a scale length of the order of 1/5 the flow diameter.

(2) By contrast, the electron eddies are thin structures elongated in the flow direction, especially on the axis. The "aspect ratio" of these elongated eddies is on the order of 1:5. Near the flow edge, however, the elongation diminishes and the electron eddies appear more coincident with and of similar shape as the temperature eddies.

(3) The electrons decay to a considerable degree within a distance of about 1/2 the flow diameter, that is, recognizeable lifetime of an electron eddy is of order d/2.

The above results are specific to the particular experiment performed, which is described in detail in References 25, 26 and 27. A very detailed picture of simultaneous gas-dynamical, thermal and electronic behavior thus exists for a high-temperature turbulent flow. For example, simultaneous temperature and electron density signals, recorded at many axial and radial positions in the flow, exist on a number of 1/2-inch, 10,000-foot tapes. This tape library is available for further data processing without the need to set-up and repeat the tests.

The actual chemistry of the flowfield is perhaps the most difficult re-entry feature to duplicate in a ground facility, and the results obtained can only be applied to the flight case via a theoretical calculation. That is, if such a theory is available for predicting electron fluctuations in flight, it can use the results of this section as a validity test. However no such theory is presently available. During the contract period just ended, an effort was made to prepare such a theory for non-equilibrium reacting mixtures along lines similar to those of Reference 28 for equilibrium mixtures. Progress was indeed made as far as to indicate the faults of previous attempts (References 29 and 30 for example) and some major improvements. Calculations actually began; however the effort to complete them was, as expected, much beyond the resources, and outside the work statement, of this program. The theoretical work was therefore temporarily halted.

APPENDIX A

EFFECT OF LATERAL DISPLACEMENT OF PROBES ON TRUE PROBE HEIGHT ABOVE CONE SURFACE

The four probes used in the PF/AEDC cone boundary-layer measurements consisted of a hot-wire anemometer (W), a pitot probe (P), a thermocouple (T) and a surface sensing probe (S). These probes were mounted on a single rake with their sensing tips located in a plane normal to the cone surface (we can ignore small displacements in the streamwise direction). In order to avoid contact between the measuring probes W, P and T and the cone surface, these probes were displaced vertically above the sense probe (i.e., in the direction normal to the cone surface) by an amount $y_o(S)$, $y_o(P)$, and $y_o(T)$ respectively (the distance $y_o(i)$ is the separation between the bottom of the surface probe and the center of the sensing area of the measuring probe). This is shown schematically in Figure A1 where the probes have been located with the surface sensor contacting the cone. Figure A1 also indicates the lateral displacement of the probes.

Because of surface curvature the true height H of any probe above the cone surface will differ from the sun $y + y_o$(where y is the vertical travel of the probe) and is given instead by the quantity $H = (R - R_c)$ where R is the length of the straight line segment between the cone center and the probe and R_c is the cone radius. This is illustrated in Figure A2 where the probe position has been defined by the polar coordinates R and θ.

The true probe height can be found in the following manner. From Figures A1 and A2 it can be shown that:

Since:

$$\theta(S)_o = \sin^{-1} \frac{L(S)}{R_c}$$

then:

$$\theta(W) = \tan^{-1} \frac{L(W)}{R_o + y_o(W) + y}$$

$$\theta(P) = \tan^{-1} \frac{L(P)}{R_o + y_o(P) + y} \qquad \text{(A-1)}$$

$$\theta(T) = \tan^{-1} \frac{L(T)}{R_o + y_o(T) + y}$$

and:

$$R_o = L(S)/\tan\theta(S)_o$$

$$R(W) = L(W)/\sin\theta(W)$$

$$R(P) = L(P)/\sin\theta(P) \qquad \text{(A-2)}$$

$$R(T) = L(T)/\sin\theta(T)$$

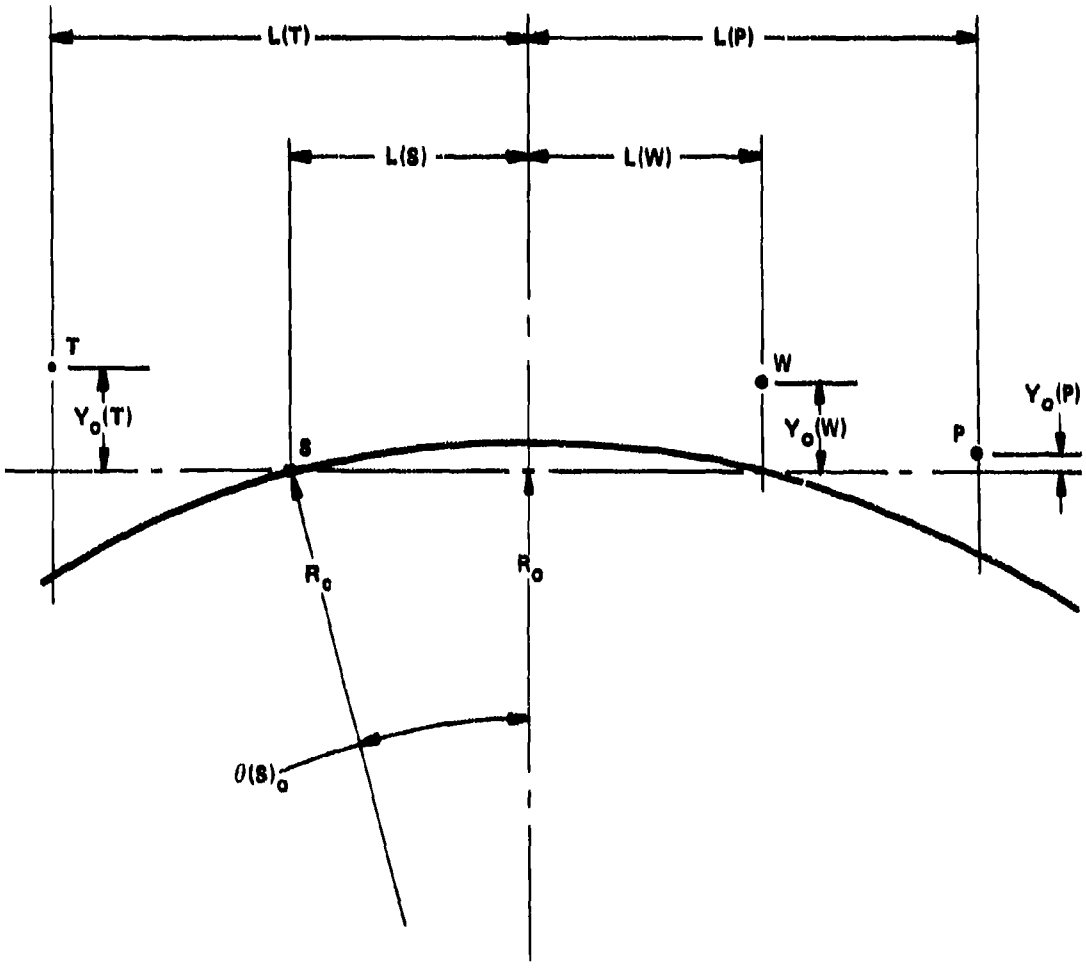

FIGURE A1. LOCATION OF PROBES RELATIVE TO CONE SURFACE WITH SENSE PROBE CONTACTING CONE.

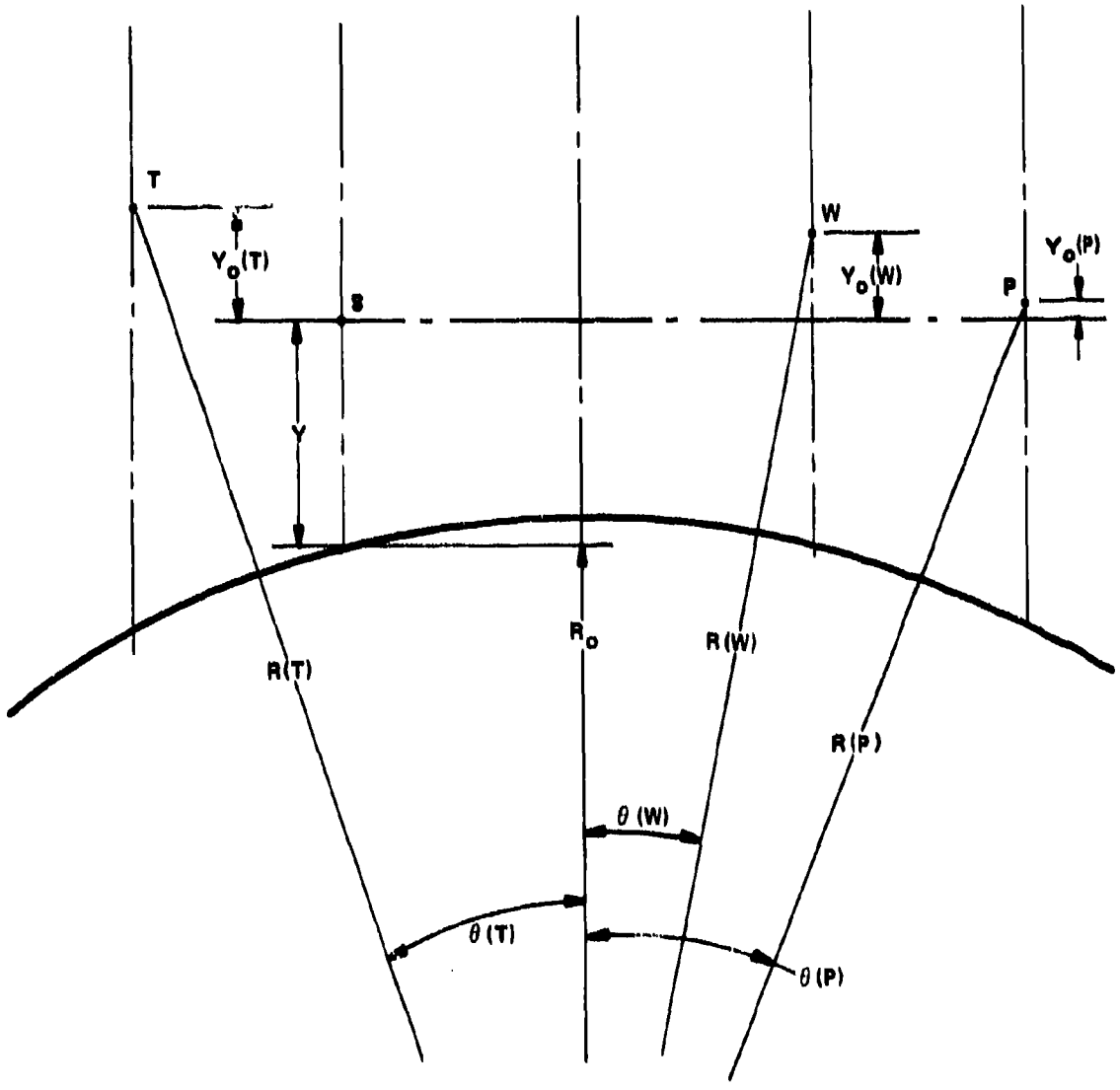

FIGURE A2. LOCATION OF PROBES RELATIVE TO CONE SURFACE SHOWING EFFECT OF SURFACE CURVATURE ON TRUE PROBE HEIGHT.

so that:

$$H(W) = R(W) - R_c$$

$$H(P) = R(P) - R_c \qquad \text{(A-3)}$$

$$H(T) = R(T) - R_c$$

It is clear that the effect of surface curvature (i.e., the difference between $(y + y_o)$ and H increases with decreasing x-Station and with decreasing y.

Since the angles $\theta(i)$ are very small H(i) can be approximated by the quantity D(i) which is defined in Figure A3 where, for simplicity, only the pitot probe is represented. It can be shown that:

$$\theta(P)_o = L(P)/R_c$$

and

$$R_o(P) = L(P)/\tan\theta(P)_o$$

so that:

$$D(P) = R_o - R_o(P) + y_o(P) + y$$

It follows, then, that:

$$D(W) = R_o - R_o(W) + y_o(W) + y \qquad \text{(A-4)}$$

$$D(T) = R_o - R_o(T) + y_o(T) + y$$

These expressions have the advantage that $R_o - R_o(P)$, the correction for surface curvature, is independent of y.

An estimate of the effect of surface curvature is provided by considering the x = 19 inch station.

Let:

R_c = 1.75 inches $\qquad y_o(W)$ = 0.030 inches

L(S) = L(S) = 0.0625 inches $\qquad y_o(P)$ = 0.010 inches

L(P) = L(T) = 0.1875 inches $\qquad y_o(T)$ = 0.040 inches

The corresponding values of y(i), H(i) and D(i) are listed below:

y(i) = 0

Probe	y(i)	H(i)	D(i)	H(i) - y(i)	D(i) - H(i)
W	.030	.0299813	.03	-1.87×10^{-5}	1.87×10^{-5}
P	.010	.0188493	.0189572	.0088	.000108
T	.040	.048683	.0489572	.00868	.000274

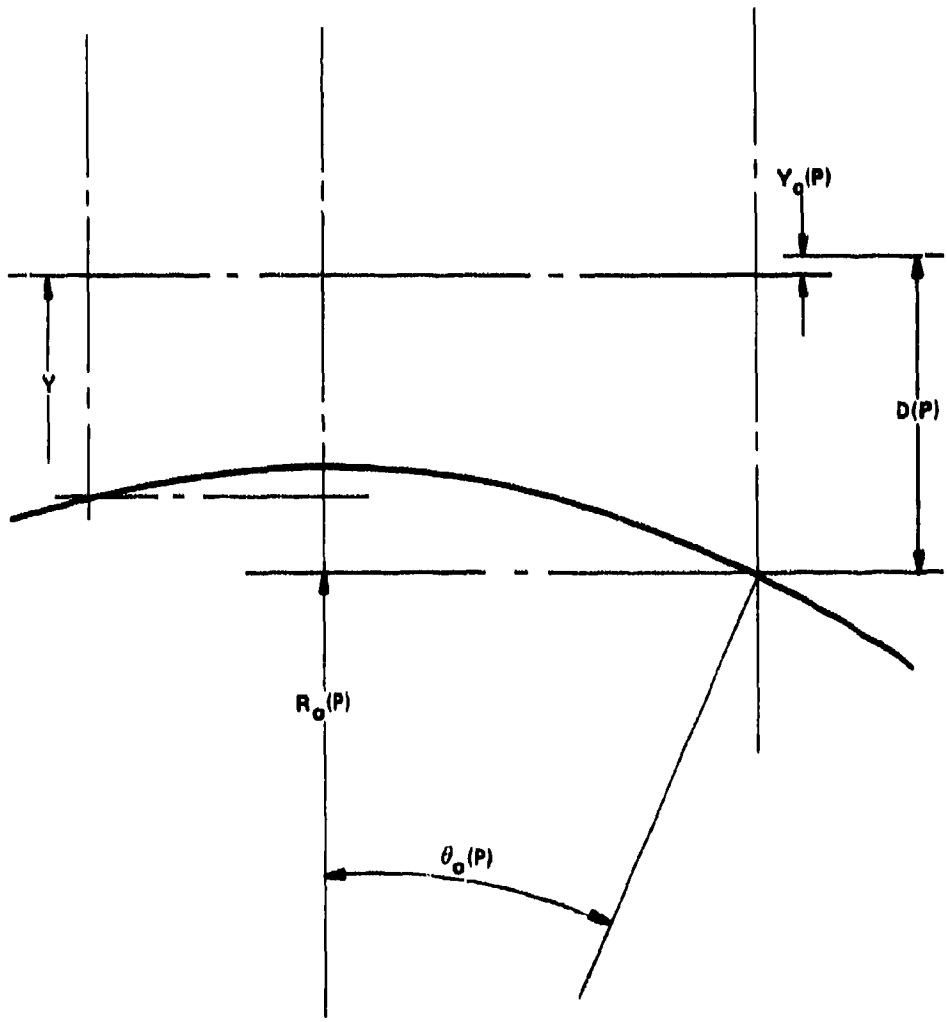

FIGURE A3. APPROXIMATION FOR TRUE PROBE HEIGHT ABOVE CONE SURFACE.

y(i) = 0.25 (outer edge of boundary-layer)

Probe	y(i)	H(i)	D(i)	H(i) - y(i)	D(i) - H(i)
W	.28	.279846	.28	-0.000154	.000154
P	.260	.267615	.268957	.007615	.00134
T	.290	.297487	.298957	.007487	.00147

It is apparent that the surface curvature effect is most significant for the pitot probe located near the surface where the error H(P) - y(P) is of the same order as y(P). It is necessary therefore to include the correction for surface curvature in the data reduction procedure. It is also clear that the difference D(i) - H(i) is within the precision with which the probe position can be specified. Therefore we can set H = D and use the expressions (A-4) to evaluate the "true" probe height.

APPENDIX B

X-PROBE RESPONSE WITH PRESSURE FLUCTUATIONS

The theory of the X-probe response at high speeds and in the absence of pressure fluctuations has been described in Appendix B of Reference 5. When pressure fluctuations cannot be neglected we must recognize that the mode and flow variables are no longer identical (see Reference 1) but rather related by the expressions:

$$T' = \sigma' + (\gamma - 1)\pi' \tag{B-1a}$$

$$u' = \tau' + (n_x/M)\pi' \tag{B-1b}$$

$$v' = \xi' + (n_y/M)\pi' \tag{B-1c}$$

$$p' = \gamma\pi' \tag{B-1d}$$

For a wire normal to flow (i.e., not sensitive to v') the response of the wire is given by:

$$e' = e_T T_T' - e_m m' \tag{B-2}$$

Expanding T_T' and m' in terms of T', u', and ρ', and introducing Eqns B-1a through B-1d and the definitions

$$\alpha \equiv \frac{1}{1 + [(\gamma - 1)/2]M^2} \quad ; \qquad \beta \equiv (\gamma - 1)M^2\alpha$$

equation B-2 can be re-written as

$$e' = e_\sigma\sigma' + e_\tau\tau' + [(\alpha(\gamma - 1) + \alpha(\gamma - 1)Mn_x)e_T - (\frac{n_x}{M} + 1)e_m]\pi' \tag{B-3}$$

Defining the bracketed term as the sensitivity to pressure fluctuations, e_π, Eqn. (B-3) becomes:

$$e' = e_\sigma\sigma' + e_\tau\tau' + e_\pi\pi'$$

where e_π is defined in the Morkovin AGARDO-graph (Reference 17) and it can be shown that:

$$\frac{e_\pi}{e_\sigma} = -\frac{(\gamma - 1)(M^2 - 1)}{1 + (\gamma - 1)M^2} + \frac{\gamma(1 + n_x M) - (M^2 - 1)\frac{n_x}{M}}{1 + (\gamma - 1)M^2} \cdot X$$

and X is the conventional mode parameter e_τ/e_σ.

For a skew wire u' is replaced with u' + v' cot Ø (see Reference 5) and the sensitivity coefficients are based now on the velocity component normal to the wire, $\bar{u}_\perp$, and not the total velocity vector, $\bar{u}$. In this case we can write that again:

$$e' = e_T T_T' - e_m m'$$

which after some algebraic manipulation reduces to:

$$e' = e_\sigma \sigma' + e_\tau \tau' + e_\tau \cot \phi\, \xi' + \Big[[\alpha(\gamma - 1) + \alpha n_x(\gamma - 1)M + \alpha(\gamma - 1)n_y M \cot \phi]e_T \; [\frac{n_x}{M} + \frac{n_y}{M} \cot \phi + 1]\; e_m\Big] \pi' \tag{B-4}$$

If we let $n_x = -\frac{1}{M}$ then Eqn. (B-4) becomes finally:

$$e' = e_\sigma \sigma' + e_\tau \tau' + e_\tau \cot \phi\, \xi' + e_\pi \pi' + [\alpha(\gamma - 1)n_y M\, e_T - \frac{n_y}{M} e_m] \cot \phi\, \pi' \tag{B-5}$$

Let us define now

$$\Delta = \alpha(\gamma - 1)n_y M\, e_T - \frac{n_y}{M} e_m \tag{B-6}$$

Since:

$$e_\sigma = \alpha e_T + e_m, \qquad \text{and} \qquad e_\tau = \beta e_T - e_m$$

then

$$e_T = \frac{1}{\alpha + \beta}(e_\sigma + e_\tau) \qquad \text{and} \qquad e_m = \frac{\beta}{\beta + \alpha} e_\sigma - \frac{\alpha}{\beta + \alpha} e_\tau$$

Consequently, Δ can be written as:

$$\Delta = \alpha(\gamma - 1)n_y M \left[\frac{e_\sigma + e_\tau}{\alpha + \beta}\right] - \frac{n_y}{M}\left[\frac{\beta}{\beta + \alpha} e_\sigma - \frac{\alpha}{\beta + \alpha} e_\tau\right] \tag{B-7}$$

From the definition of α and β it can be shown that:

$$\alpha + \beta = \frac{(\gamma - 1)M^2 + 1}{1 + [(\gamma - 1)/2]M^2}$$

$$\frac{\alpha}{\alpha + \beta} = \frac{1}{1 + (\gamma - 1)M^2}$$

$$\frac{\beta}{\gamma + \beta} = \frac{(\gamma - 1)M^2}{1 + (\gamma - 1)M^2}$$

and therefore that:

$$\Delta = \frac{\gamma n_y M - (M^2 - 1)\frac{n_y}{M}}{1 + (\gamma - 1)M^2} e_\tau = h(M, n_y)\ e_\tau \qquad \text{(B-8)}$$

Substituting Eqn. (B-8) into Eqn. (B-5) we have:

$$e' = e_\sigma \sigma' + e_\tau \tau' + e_\tau \cot \phi\ \xi' + e_\pi \pi' + \Delta \cot \phi\ \pi' \qquad \text{(B-9)}$$

From Morkovin (Reference 17) the hot-wire sensitivity to the sound mode for a wire normal to the flow is given by:

$$e_\pi = f(M)\ e_\sigma + g(M, n_x)\ e_\tau$$

where

$$f(M) = \frac{(\gamma - 1)(M^2 - 1)}{1 + (\gamma - 1)M^2}$$

$$g(M, n_x) = \frac{\gamma(1 + n_x M) - (M^2 - 1)\frac{n_x}{M}}{1 + (\gamma - 1)M^2}$$

For a skew wire, therefore, we can re-define the sound mode sensitivity coefficient as:

$$e_\pi^* = e_\pi + \Delta \cot \phi = f(M) e_\sigma + [g(M, n_x) + h(M, n_y) \cot \phi] e_\tau \qquad \text{(B-10)}$$

so that the hot-wire response equation becomes:

$$e' = e_\sigma \sigma' + e_\tau \tau' + e_\tau \cot \phi\ \xi' + e_\pi^* \pi' \qquad \text{(B-11)}$$

Using the notation of Appendix B, Reference 5 we can write:

$$p = e_\tau$$

$$q = e_\tau \cot \phi = p \cot \phi$$

$$r = e_\sigma$$

$$s = e_\pi^*$$

so that Eqn. (B-11) becomes:

$$e' = p\tau' + q\xi' + r\sigma' + s\pi' \tag{B-12}$$

or, taking the mean square of each of the above equation:

$$\begin{aligned}\overline{e'^2} = {} & p^2\overline{\tau'^2} + q^2\overline{\xi'^2} + r^2\overline{\sigma'^2} + s^2\overline{\pi'^2} + 2pq\overline{\tau'\xi'} + 2pr\overline{\tau'\sigma'} \\ & + 2ps\overline{\tau'\pi'} + 2qr\overline{\xi'\sigma'} + 2qs\overline{\xi'\pi'} + 2rs\overline{\sigma'\pi'}\end{aligned} \tag{B-13}$$

Although Eqn. (B-13) is comprised of the ten unknowns:

$$\overline{\tau'^2} \qquad \overline{\xi'^2} \qquad \overline{\sigma'^2} \qquad \overline{\pi'^2} \qquad \overline{\sigma'\pi'}$$

$$\overline{\tau'\xi'} \qquad \overline{\tau'\sigma'} \qquad \overline{\tau'\pi'} \qquad \overline{\xi'\sigma'} \qquad \overline{\xi'\pi'}$$

with the X-probe we can only find 6 unknowns and must eliminate 4 unknowns before proceeding. As in Reference 1 we rely on Morkovin's suggestion that in a "good" wind tunnel the sound mode is uncorrelated with the other modes. That is, we let:

$$\overline{\tau'\pi'} = \overline{\xi'\pi'} = \overline{\sigma'\pi'} = 0$$

Furthermore we assume that:

$$\overline{\sigma'\tau'} = \left[(\overline{\sigma'})^2 \cdot (\overline{\tau'})^2\right]^{\frac{1}{2}}, \quad \text{i.e., that } R_{\sigma\tau} = -1.0$$

With the above assumptions, Eqn. (B-13) reduces to:

$$\begin{aligned}\overline{e'^2} = {} & p^2\overline{\tau'^2} + q^2\overline{\xi'^2} + r^2\overline{\sigma'^2} + s^2\overline{\pi'^2} + 2pq\overline{\tau'\xi'} \\ & - 2pr(\overline{\sigma'^2})^{\frac{1}{2}}(\overline{\tau'^2})^{\frac{1}{2}} + 2qr\overline{\xi'\sigma'}\end{aligned} \tag{B-14}$$

Letting finally $p/r = e_\tau/e_\sigma \equiv X$ and dividing both sides of Eqn. (B-14) by r^2 we obtain:

$$\begin{aligned}Y^2 \equiv \frac{\overline{e'^2}}{r^2} = {} & X^2\overline{\tau'^2} + X^2 \cot^2\phi\, \overline{\xi'^2} + \overline{\sigma'^2} \\ & + \left[f(M) + [g(M,n_x) + h(M,n_y) \cot\phi]\, X\right]^2 \overline{\pi'^2} \\ & + 2X^2 \cot\phi\, \overline{\tau'\xi'} - 2X\,\sigma\tau + 2X \cot\phi\, \overline{\xi'\sigma'}\end{aligned} \tag{B-15}$$

which, after collecting like powers of X, can be written as:

$$Y^2 = X^2 \left[\overline{\tau'^2} + \cot^2 \phi\, \overline{\xi'^2} + 2\cot\phi\, \overline{\tau'\xi'} + (g + h\cot\phi)^2\, \overline{\pi'^2}\right] - 2X\left[\sigma\tau - \cot\phi\, \overline{\xi'\sigma'} - f(g + h\cot\phi)\, \overline{\pi'^2}\right] + \left[\overline{\sigma'^2} + f^2\, \overline{\pi'^2}\right] \quad \text{(B-16)}$$

or

$$Y^2 = AX^2 + BX + C \quad \text{(B-17)}$$

For an X-probe we can write the above expression for both wires (denoted 1 and 2) and modal analysis will yield the following quantities:

$$A_1 = \overline{\tau'^2} + \cot^2 \phi_1\, \overline{\xi'^2} + 2\cot\phi_1\, \overline{\tau'\xi'} + (g + h\cot\phi_1)^2\, \overline{\pi'^2} \quad \text{(B-18a)}$$

$$B_1 = -\sigma\tau + \cot\phi_1\, \overline{\xi'\sigma'} + f(g + h\cot\phi_1)\, \overline{\pi'^2} \quad \text{(B-18b)}$$

$$C_1 = \overline{\sigma'^2} + f^2\, \overline{\pi'^2} \quad \text{(B-18c)}$$

$$A_2 = \overline{\tau'^2} + \cot^2 \phi_2\, \overline{\xi'^2} + 2\cot\phi_2\, \overline{\tau'\xi'} + (g + h\cot\phi_2)^2\, \overline{\pi'^2} \quad \text{(B-18d)}$$

$$B_2 = -\sigma\tau + \cot\phi_2\, \overline{\xi'\sigma'} + f(g + h\cot\phi_2)\, \overline{\pi'^2} \quad \text{(B-18e)}$$

$$C_2 = \overline{\sigma'^2} + f^2\, \overline{\pi'^2} \quad \text{(B-18f)}$$

Note that C_1 must equal C_2 and therefore Eqns. (B-18c) and (B-18f) reduce to a single expression:

$$C = \overline{\sigma'^2} + f^2\, \overline{\pi'^2} \quad \text{(B-18g)}$$

We can also write for wires 1 and 2

$$e_1' = p_1\tau' + p_1\cot\phi_1\, \xi' + r_1\sigma' + [fr_1 + (g + h\cot\phi_1)\, p_1]\, \pi' \quad \text{(B-19)}$$

$$e_2' = p_2\tau' + p_2\cot\phi_2\, \xi' + r_2\sigma' + [fr_2 + (g + h\cot\phi_2)\, p_2]\, \pi' \quad \text{(B-20)}$$

Then, taking the mean square of the product $e_1'e_2'$ yields:

$$
\begin{aligned}
\overline{e_1' e_2'} = {} & p_1 p_2 \overline{\tau'^2} + p_1 p_2 \cot \phi_2 \, \overline{\xi'\tau'} - p_1 r_2 \, \sigma\tau \\
& + p_1 p_2 \cot \phi_1 \, \overline{\xi'\tau'} + p_1 p_2 \cot \phi_1 \cot \phi_2 \, \overline{\xi'^2} \\
& + p_1 r_2 \cot \phi_1 \, \overline{\xi'\sigma'} - p_2 r_1 \, \sigma\tau + p_2 r_1 \cot \phi_2 \, \overline{\xi'\sigma'} \qquad \text{(B-21)} \\
& + r_1 r_2 \, \overline{\sigma'^2} + [f r_1 + (g + h \cot \phi_1) \, p_1] \, [f r_2 \\
& + (g + h \cot \phi_2) \, p_2] \, \overline{\pi'^2}
\end{aligned}
$$

or

$$
\begin{aligned}
\overline{e_1' e_2'} = {} & p_1 p_2 \overline{\tau'^2} + p_1 p_2 \cot \phi_2 \, \overline{\xi'\tau'} + p_1 p_2 \cot \phi_1 \, \overline{\xi'\tau'} \\
& + p_1 p_2 \cot \phi_1 \cot \phi_2 \, \overline{\xi'^2} - p_1 r_2 \, \sigma\tau + p_1 r_2 \cot \phi_1 \, \overline{\xi'\sigma'} \\
& - p_1 p_2 \, \sigma\tau + p_2 r_1 \cot \phi_2 \, \overline{\xi'\sigma'} + r_1 r_2 \, \overline{\sigma'^2} + f^2 \, r_1 r_2 \, \overline{\pi'^2} \qquad \text{(B-22)} \\
& + p_1 r_2 \, f(g + h \cot \phi_1) \, \overline{\pi'^2} + p_2 r_1 \, f(g + h \cot \phi_2) \overline{\pi'^2} \\
& + p_1 p_2 \, (g + h \cot \phi_1)(g + h \cot \phi_2) \, \overline{\pi'^2}
\end{aligned}
$$

Dividing both sides of (B-22) by $r_1 r_2$ we have:

$$
\begin{aligned}
Z \equiv \frac{\overline{e_1' e_2'}}{r_1 r_2} = {} & X_1 \Big[X_2 [\overline{\tau'^2} + \cot \phi_2 \, \overline{\xi'\tau'} + \cot \phi_1 \, \overline{\xi'\tau'} \\
& + \cot \phi_1 \cot \phi_2 \, \overline{\xi'^2} + (g + h \cot \phi_1)(g + h \cot \phi_2) \, \overline{\pi'^2}] \\
& + [-\sigma\tau + \cot \phi_1 \, \xi'\sigma' + f(g + h \cot \phi_1) \, \pi'^2] \Big] \qquad \text{(B-23)} \\
& + X_2 [-\sigma\tau + \cot \phi_2 \, \overline{\xi'\sigma'} + f(g + h \cot \phi_2) \, \overline{\pi'^2}] \\
& + [\sigma'^2 + f^2 \, \overline{\pi'^2}]
\end{aligned}
$$

$$
= X_1 \, [D_1 X_2 + D_2] + D_3 X_2 + D_4 \qquad \text{(B-24)}
$$

Equation (B-24) can be solved by the "correlation mode" scheme described in Reference 5 to yield:

$$D_1 = \overline{\tau'^2} + \cot \phi_1 \cot \phi_2 \overline{\xi'^2} + (\text{cor } \phi_1 + \cot \phi_2) \overline{\xi'\tau'} + (g + h \cot \phi_1)(g + h \cot \phi_2) \overline{\pi'^2} \tag{B-25a}$$

$$D_2 = -\sigma\tau + \cot \phi_1 \overline{\xi'\sigma'} + f\,(g + h \cot \phi_1) \overline{\pi'^2} \tag{B-25b}$$

$$D_3 = -\sigma\tau + \cot \phi_2 \overline{\xi'\sigma'} + f\,(g + h \cot \phi_2) \overline{\pi'^2} \tag{B-25c}$$

$$D_4 = \overline{\sigma'^2} + f^2 \overline{\pi'^2} \tag{B-25d}$$

Note again that $D_4 = C$ and that Eqns. (B-18b) and (B-18c) are identical respectively, to Eqns. (B-25b) and B-25c).

Defining $A_3 = B_1 = D_2$ and $A_4 = B_2 = D_3$, the governing equations, therefore, reduce to the following expressions:

$$A_1 = \overline{\tau'^2} + \cot^2\phi_1 \overline{\xi'^2} + 2\cot \phi_1 \overline{\xi'\tau'} + (g + h \cot \phi_1)^2 \overline{\pi'^2} \tag{B-26a}$$

$$A_2 = \overline{\tau'^2} + \cot^2\phi_2 \overline{\xi'^2} + 2\cot \phi_2 \overline{\xi'\tau'} + (g + h \cot \phi_2)^2 \overline{\pi'^2} \tag{B-26b}$$

$$A_3 = -\sigma\tau + \cot \phi_1 \overline{\xi'\sigma'} + f(g + h \cot \phi_1) \overline{\pi'^2} \tag{B-26c}$$

$$A_4 = -\sigma\tau + \cot \phi_2 \overline{\xi'\sigma'} + f(g + h \cot \phi_2) \overline{\pi'^2} \tag{B-26d}$$

$$D_1 = \overline{\tau'^2} + \cot \phi_1 \cot \phi_2 \overline{\xi'^2} + (\cot \phi_1 + \cot \phi_2) \overline{\xi'\tau'} + (g + h \cot \phi_1)(g + h \cot \phi_2) \overline{\pi'^2} \tag{B-26e}$$

$$C = \overline{\sigma'^2} + f^2 \overline{\pi'^2} \tag{B-26f}$$

Eqns. (B-26a) to (B-26f) represent a set of six non-linear simultaneous equations which can be solved to find the six unknowns:

$\overline{\tau'^2}$, $\overline{\sigma'^2}$, $\overline{\xi'^2}$, $\overline{\pi'^2}$, $\overline{\xi'\tau'}$ and $\overline{\xi'\sigma'}$.

APPENDIX C

CONE DRAG BUDGET

(a) Pressure (Inviscid) Drag

The cone pressure drag $\mathcal{D}_p$ is made up of the curved-surface drag $\mathcal{D}_c$ and the base pressure drag $\mathcal{D}_b$. The former is the product of the axial component $p_x = p_c \sin\theta$ of the surface pressure p_c, times the cone curved area

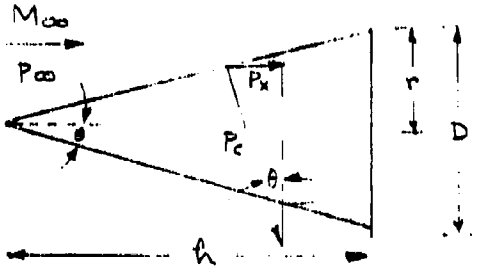

$$A_c = \frac{\pi r^2}{\sin\theta} \qquad \text{(C-1)}$$

Thus,

$$\mathcal{D}_c = p_c \sin\theta \frac{\pi r^2}{\sin\theta} = p_c \pi r^2 \qquad \text{(C-2)}$$

Furthermore since the cone is slender ($\theta = 5^\circ$) we can approximate (for $M_\infty = 3$):

$$p_c \simeq p_\infty = \frac{\rho_\infty u_\infty^2}{\gamma M_\infty^2} = \frac{2q}{\gamma M_\infty^2} \qquad \text{(C-3)}$$

where $q = (1/2)\,\rho_\infty u_\infty^2$, the dynamic pressure. Thus,

$$\mathcal{D}_c = \frac{2q}{\gamma M_\infty^2}\pi r^2$$

The base pressure can only be estimated from the available data as:

$$p_b \simeq \frac{1}{4} p_\infty = \frac{1}{4}\frac{2q}{\gamma M_\infty^2}$$

and

$$\mathcal{D}_p = -p_b \pi r^2$$

so that

$$\mathcal{D}_p = \mathcal{D}_c + \mathcal{D}_b = q\pi r^2 \frac{2}{\gamma M_\infty^2}\left(1 - \frac{1}{4}\right) = q(\pi r^2)\left[\frac{1.5}{\gamma M_\infty^2}\right] \qquad \text{(C-4)}$$

(b) Viscous Drag (Laminar)

Since the laminar shear stress τ_w is a function of the distance s along a ray, we have to integrate its x-component $\tau_{wx} = \tau_w \cos\theta$ over the cone area:

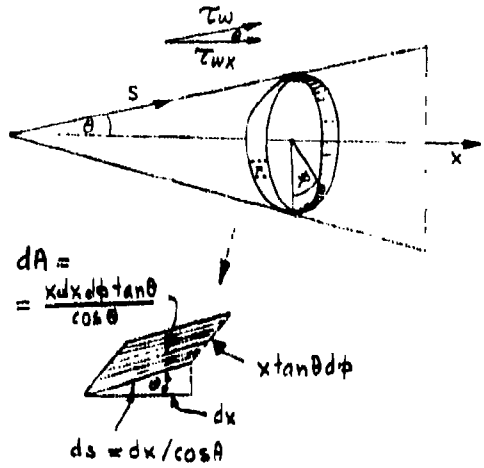

$$\text{viscous drag } \mathcal{D}_v = \int_A \tau_{wx}\,dA = \cos\theta \int \tau_w\,dA \qquad \text{(C-5)}$$

From the sketch, we find that the surface area element dA is

$$dA = \frac{x\,dx\,d\phi}{\cos\theta}\tan\theta \qquad \text{(C-6)}$$

For the skin stress τ_w we write

$$\tau_w = \frac{1}{2}\rho_e u_e^2 c_f \simeq \frac{1}{2}\rho_\infty u_\infty^2 c_f = q c_f \qquad \text{(C-7)}$$

where c_f is a laminar friction coefficient:

$$c_f = \frac{C}{\sqrt{Re_s}} \quad \left(\text{where } Re_s = \frac{u_\infty s_\infty}{\nu_\infty}\right) \qquad \text{(C-8)}$$

Since $s = x/\cos\theta$

$$c_f = \frac{C}{\sqrt{Re'}}\sqrt{\cos\theta/x} \qquad \left(Re' \equiv \frac{u_\infty}{\nu_\infty}, \text{ unit Reynolds No.}\right) \qquad \text{(C-9)}$$

Inserting Eqns. (C-6), C-7), and (C-9) into (C-5) we get:

$$\mathcal{D}_v = \cos\theta \int_\varphi \int_x \frac{qC}{\sqrt{Re'}}\sqrt{\cos\theta}\,\frac{\tan\theta}{\cos\theta}\,\frac{x}{\sqrt{x}}\,dx\,d\varphi$$

$$= \frac{2\pi\, qC\tan\theta\sqrt{\cos\theta}}{\sqrt{Re'}}\int_{x=0}^{h}\sqrt{x\,dx}$$

$$= \frac{4}{3\pi}\,\frac{qC\tan\theta\sqrt{\cos\theta}}{\sqrt{Re'}}\,h^{3/2}$$

Since $h = \frac{D}{2 \tan \theta}$ and $Re' = \frac{u_\infty}{\nu_\infty} \frac{1}{D} = \frac{Re}{D}$,

and since C has to be multiplied by $\sqrt{3}$ to apply to the cone (Reference 31, p.1067) we get

$$\mathcal{D}_v = \pi \sqrt{2/3} \frac{qC^2}{\sqrt{Re_D}} \left[\frac{\cos \theta}{\sqrt{\sin \theta}}\right] \tag{C-10}$$

(c) <u>Viscous Drag (Turbulent)</u>

For the turbulent case, Eqn. (C-8) is changed to

$$c_f = \frac{0.0262}{(Re_\infty)^{1/7}} \left[\frac{2}{2 + \frac{\gamma - 1}{2} M_\infty^2}\right]^{5/7} = \frac{k}{(Re_\infty)^{1/7}} f^{5/7}$$

from Reference 31, p. 1109. Here

$$k = 0.0262$$

$$Re_\infty = \frac{u_\infty s}{\nu_\infty} = \frac{u_\infty}{\nu_\infty} \frac{x}{\cos \theta}$$

$$f = \frac{2}{2 + \frac{\gamma - 1}{2} M_\infty^2}$$

Since θ is small, we write $(\cos \theta)^{1/7} \approx 1$. Then

$$c_f = \frac{kf^{5/7}}{(Re_\infty')} x^{-1/7}, \qquad \text{and} \qquad \tau_w = qc_f = Px^{1/7}$$

where $P = \frac{kqf^{5/7}}{(Re_\infty')^{1/7}}$

Then Eqn. (C-5) becomes

$$\text{Turbulent drag} = \mathcal{D}_T = \int_\phi \int_x P \tan \theta \, x^{-1/7} \, x d \, x d\phi$$

$$= \frac{14}{13} \pi P \tan \theta \, h^{13/7}$$

and since

$$h^{13/7} P = \frac{kqf^{5/7}}{Re^{1/7}} \left[\frac{2}{4 \tan^2 \theta}\right] (2 \tan \theta)^{1/7}$$

with $Re_D = u_\infty / \nu_\infty$, we get

$$T = \frac{7\pi}{26} \frac{D^2 q^2 k f^{5/7}}{\tan\theta \, Re_D^{1/7}} (2 \tan\theta)^{1/7} \qquad \text{(C-11)}$$

(d) Definition of Drag Coefficients

If the total cone drag $\mathcal{D}$ is defined on the basis of the base area

$$A_b = \frac{\pi D^2}{4} = \pi r^2$$

so that

$$\mathcal{D} = \mathcal{D}_p + \mathcal{D}_v = q C_D A_b = q A_b (C_{D_p} + C_{D_v})$$

we can compute the C_D for each contribution as follows:

Pressure drag:

From Eqn. (C-4) we get

$$C_{D_p} = \frac{1.5}{\gamma M_\infty^2}$$

For $M_\infty = 3$, $C_{D_p} = 0.119$.

Laminar viscous drag:

From Eqn. (C-10) we get

$$C_{D_\ell} = 4\sqrt{2/3} \frac{C}{\sqrt{Re_D}} \frac{\cos\theta}{\sqrt{\sin\theta}}$$

A computation will be made for the lowest pressure experiment (F experiment, P_o = 280 mm Hg abs., Re_D = 69,000). The constant C is taken as the Blasius 0.664 reduced by 10% to account for the friction decrease due to Mach 3 (over the incompressible value). We find

$$C_{D_\ell} = 0.0248 \qquad \text{(C-12)}$$

The total C_D for this case is

$$C_D = C_{D_p} + C_{D_\ell} = 0.144.$$

Turbulent viscous drag:

From Eqn. (C-11) we get

$$C_{D_T} = \frac{14}{13} \frac{kf^{5/7}}{\tan\theta} \left[\frac{2 \tan\theta}{Re_D}\right]^{1/7}$$

Here the computation is done for the A experiment, $Re_D = 178{,}000$. The result is

$$C_{D_T} = 0.0284 \qquad \text{(C-13)}$$

The total C_D for this case is

$$C_D = C_{D_i} + C_{D_T} = 0.147 \qquad \text{(C-14)}$$

(e) Comparison of Inviscid, Laminar and Turbulent Drag

We note from Eqns. (C-12) and C-13) that there is little difference between laminar and turbulent friction drag. The actual difference is of course even smaller because in the A configuration only a portion of the model boundary-layer is turbulent. This near-equality is not surprising, even accounting for the usual higher value of the turbulent friction coefficient over the laminar one (Reference 31). The point is that the plots, including those in the latter Reference, show the flat plate coefficients and usually at higher Re_x (from 10^5 to 10^7). In the present case the Reynolds numbers are lower, and the laminar friction coefficient is multiplied by the factor $\sqrt{3}$ to account for the conical flow. Thus the present laminar coefficient is equal to or larger than the turbulent one over the front end of the cone.

Without yet looking at the WEM-III computer results which give the "drag diameter" C_DA, we ask how the C_DA values computed above compare with the base diameter D. For the A test condition (the post-BLT case) we have

$$C_DA = (C_{D_i} + C_{D_T})A = 0.147 \frac{\pi D^2}{4} = 0.115D^2$$

$$(C_DA)^{1/2} = 0.34D, \qquad D = 2.94\,(C_DA)^{1/2}$$

with negligible difference for the laminar F condition (pre-BLt, Eqn. (C-12)). Thus, 6 base diameters (the limit of the present test surveys) mean a distance of 17.7 $(C_DA)^{\frac{1}{2}}$. However, the proper similarity parameter is the wake drag diameter $(C_DA)_w^{\frac{1}{2}}$. Since this corresponds only to the viscous-friction portion $C_{D_T}A$ of the body drag,

$$(C_D A)_w^{\frac{1}{2}} = (C_{D_T} A)^{\frac{1}{2}} = \left(0.0284 \frac{\pi D^2}{4}\right)^{\frac{1}{2}} = 0.15D,$$

$$D = 6.66\ (C_D A)_w^{\frac{1}{2}}$$

for the turbulent case and, similarly,

$$(C_D A)_w^{\frac{1}{2}} = 0.14D, \qquad D = 7.15\ (C_D A)_w^{\frac{1}{2}}$$

for the laminar case. Thus a surveyed distance of 6D equals a distance of about 40 <u>wake</u> drag diameters in the A test and of about 43 wake drag diameters in the F test.

APPENDIX D

COMPUTER PROGRAM WEB-IV (DRB4E)

COMPUTATION INSTRUCTIONS*

7.1 Segregate the (Z,V) from the (Z,F) points. Note that the first point of each set (i.e., each current code A, B, etc.) is a Z, V point. The points are in increasing order of y and alternate from Z, V to Z, F.

7.2 Assign y's to each Z, V or Z, F point. To do that, first note the first (y_o) and last (y_e) points for that x; see Table 1. All current codes of that x obey the same rules. Then add 0.010 inch to the next point in line, all the way, until the last point y_e.

For example, the card on p. 2 is the first card of the K set, x = 0.8, WEMA. According to Table 1, y_o = 0.200, y_e = 0.595. Thus the points are listed as follows:

Z, V Points			Z, F Points		
y	Z	V	y	Z	F
0.200	-.4722	.2409	0.205	-.4769	-.4933
0.210	-.4812	.2406	0.215	-.4881	-.5132
0.220	-.4967	.2403	0.225	(first point on next card)	
.	.	.	.	.	.
.	.	.	.	.	.
.	.	.	.	.	.

The y points correspond to those of the WEM-I, II outputs (where they are listed as y/D). From now on, we work with the Z, V points separately from the Z, F points.

7.3 Computation of the "Sensitivity Matrix" (Z, V Data Only)

7.3.1 For each x, go to Table 1, select the "current group". Then Table 2 gives the current i, for each group, matched to the current code, B, C.....K. At each y of that particular x,

---

* Numbering of subsections in this Appendix is kept identical to that of the actual program on file at Philco-Ford. Consistently, references to page and Table numbers refer to that file, not to page or Table numbers in this report.

7.3.2 Match the V from each current code with the i from Table 2. You now have an i, V curve.

7.3.3 Compute $R' = 1000\ V/i$ for each i. You now have an i, R' curve.

7.3.3a Compute $R = R' - 1.42$.

7.3.4 Compute by least squares the coefficients C, C_1 and C_2 from the curve R, i^2:

$$R = C + C_1 i^2 + C_2 i^4$$

(That is, "plot" R versus i^2 and curve-fit that with a second-degree polynomial in i^2).

7.3.5 Compute:

$$A_w' = \frac{1}{2} \frac{i}{R} \frac{dR}{di} = \frac{i^2}{R} (C_1 + 2C_2 i^2) \quad \text{each i}$$

7.3.6 Compute:

$$T_w = \frac{1}{\alpha_o} \left(\frac{R}{R_o} - 1\right) + 273.18 \qquad \text{each i}$$

using R from 7.3.3 and α_o, R_o from Table 1. (Note that which α_o, R_o you choose depends on x).

7.3.7 Compute:

$$T_{aw} = \frac{1}{\alpha_o} \left(\frac{C}{R_o} - 1\right) + 273.18$$

with C from 7.3.4.

7.3.8 Compute:

$$\tau_{wr} = \frac{T_w - T_{aw}}{T_{aw}} \qquad \text{each i}$$

from 3.3.7 and 3.3.6.

7.3.9 Compute:

$$K = \alpha_o R_o \frac{T_w}{R} \qquad \text{each i}$$

from 7.3.3 and 7.3.6 and α_o, R_o from Table 1.

7.3.10 Compute:

$$C_f = \frac{0.992}{1 + 0.016\ A_w'} \qquad \text{each i}$$

from 7.3.5.

7.3.11 Obtain (at the y considered) the quantity Re = 2 (Wire Reynolds No.)

7.3.11a At each point y compute:

$$k = (6.47 + 0.02268\,(T_{aw} - 390)) \times 10^{-4}$$

with T_{aw} from step 7.3.7.

7.3.11b Compute:

$$Nu_m = \frac{\alpha_o R_o}{\pi \ell} \frac{1}{k} \frac{C}{C_1} \times 10^{-6}$$

where α_o, R_o are from Table 1, $\pi = 3.14.....$, k is from 7.3.11a, C and C_1 from 7.3.4 and ℓ (in inches) is also given from Table 1.

7.3.11c At each y, we now have a value of Nu_m from 7.3.11b and a value of Re as given in 7.3.11. Using the points Nu_m, Re for the particular x-Station only, curve-fit these points into a single straight line:

$$Nu_m = N_1 + N_2\,Re$$

and thus find N_1 and N_2.

7.3.11d Similarly, curve-fit the ratio T_{aw}/T_o versus Re:

$$\eta = \frac{T_{aw}}{T_o} = H_1 + H_2(Re) + H_3(Re)^2$$

where T_{aw} is from step 7.3.7 and T_o is from the WEM-II output, designated TOTAL TEMP (deg. K). Thus find the constants H_1, H_2 and H_3.

7.3.11e Print the quantities N_1, N_2, H_1, H_2 and H_3 on top of the output page called "INTENSITIES" for that particular x-Station.

7.3.12 Compute:

$$\phi = \frac{Re}{Nu_m} N_2 = \frac{N_2\,Re}{N_1 + N_2\,Re}$$

with Re from 7.3.11.

7.3.13 Compute:

$$\psi = \frac{Re}{\eta}\,(H_2 + 2H_3\,Re)$$

from Re from 7.3.11, $\eta = T_{aw}/T_o$, H_2 and H_3 from 7.3.11d.

7.3.14 Compute:

$$e_m = C_f A_w' \left[\emptyset - \frac{\psi}{\tau_{wr}} \right] \qquad \text{each } i$$

using C_f from 7.3.10, A_w' from 7.3.5, τ_{wr} from 7.3.8, and $\emptyset$, ψ from 7.3.12 and 7.3.13.

7.3.15 Compute:

$$e_T = C_f \left[K + A_w' \, (K + 0.765\emptyset - 1.885) - 0.765\psi \frac{A_w'}{\tau_{wr}} \right]$$

each i

with C_f, A_w', $\emptyset$, ψ, and τ_{wr} as before and K from 7.3.9.

7.3.16 Compute:

$$\alpha \equiv \frac{1}{1 + 0.2\, M^2}, \qquad \beta = 0.4\, \alpha\, M^2$$

where M is the Mach number at this particular y (from the output of WEM-II).

7.3.17 Compute:

$$X = \frac{\beta e_T - e_m}{\alpha e_T + e_m} \qquad \text{each } i$$

using 7.3.14, 7.3.15 and 7.3.16. Note: It is desired to print out the matrix i, y, X(the "sensitivity matrix").

Experiment: _____, X = _____

i corresponding to current codes (see Table 2)

y	Code A	Code B	Code C	Code D	.....K
.					
.					
.					
.					
.					
.					

Values of X from 7.3.17.

7.3.18 Print the "Wire Voltage Matrix" for the Z, V data:

i corresponding to current codes (see Table 2)

Y/D	Code A	Code B	.....K
.			
.			
.			
.			

Values of V at each point, fron input cards. Print this between the "sensitivity matrix" and the "mode matrix" for the Z, V data.

7.4 Computation of the Mode Matrix for Wideband Fluctuations

At each x, consider now the points which have Z, V data only. At eacy y:

7.4.1 Match the Z and V from each current code with the i from Table 2.

7.4.1a Compute:

$$Z_1 = t_1(Z^2 - Z_N^2)^{\frac{1}{2}} \qquad \text{each } i$$

where Z_N, t_1 come from Table 1 (one Z_N for each experiment and x-Station).

If $(Z^2 - Z_N^2)$ is negative, set to zero.

7.4.2 Compute:

$$Z' = \frac{Z_1}{GV} \qquad \text{each } i$$

where G comes from Table 1.

7.4.3 Compute:

$$Y^2 = \left[\frac{Z'}{\alpha e_T + e_m}\right]^2 \qquad \text{each } i$$

using Z' from 7.4.2, α from 7.3.16, e_T from 7.3.15 and e_m from 7.3.14.

7.4.4 For each i, we now have an X(from 7.3.17) and a Y^2(from 7.4.3). Solve, by curve-fitting, a second degree polynomial (least squares) for the coefficients A, B, C of

$$Y^2 = AX^2 + BX + C \qquad \text{each } y$$

(do not confuse this with the C of step 7.3.4)!

7.4.5 Call:

$$\tau = (A)^{\frac{1}{2}}$$
$$\sigma = (C)^{\frac{1}{2}} \qquad \text{each } y$$
$$r_{\sigma\tau} = B/2\,\sigma\tau$$

so that at each y we have a τ, a σ, and an $r_{\sigma\tau}$.

7.4.6 Compute:

$$SRA = \frac{\sigma}{0.4\ M^2\ \tau} \qquad \text{each } y$$

Note: Print out the X-Y matrix:

Experiment: _____, X = _____

	Code A	Code B		Code K
y	X	X		X
.			Y values	
.				
.				
.				
.				
.				

7.4.7 Print, at each x and y/D:

$$u'/u_\infty = (\tau)u = \frac{u'}{u}\,\frac{u}{u_\infty}$$

where τ is from step 7.4.5 and u is from the WEM-II output (the same as used in step 7.5.9).

7.4.8 Similarly, print at each x, y/D:

$$T'/T_\infty = (\sigma)T = \frac{T'}{T}\,\frac{T}{T_\infty}$$

where σ comes from step 7.4.5 and T is from the WEM-II output. (In the WEM-II, this T is printed out as "non-dim temperature").

7.4.9 Also form the quantity

$$u'/\Delta u = \frac{(u'/u_\infty)}{w}\,\frac{63600}{u_e}$$

where u'/u_∞ is from step 7.4.7 and w, u_e are a function of x-Station only. It is the same w and u_e output in the WEM-III program for each x, from Table 3. That is, the u'/u_∞ column at each x is multiplied by the constant $1/w\ (63600/u_e)$ and plotted adjacently.

Note: u_e and w are unique (constant) for each x).

7.4.10 Similarly, form

$$T'/\Delta T = \frac{(T'/T_\infty)}{\theta}$$

where T'/T_∞ is from step 7.4.8 and θ is output at each x in WEM-III from Table 3.

7.5 Computation of the Mode Matrix for the Scales

Consider now the y point (at each x) having Z, F data only. For each y,

7.5.1 Match the F from each current code with the i from Table 2.

7.5.1a Compute:

$$F_1^2 = F^2 - F_N^2 \qquad \text{each } i$$

where F_N comes from Table 1. If $(F^2 - F_N^2)$ is negative, set to zero.

7.5.2 Compute:

$$e^2 = \frac{F_1^2}{7G^2} \frac{t_2^2}{J^2} \qquad \text{each } i$$

where G is on Table 1.

7.5.3 Compute:

$$Y_F^2 = \frac{e^2}{(\alpha e_T + e_m)^2 V^2} \qquad \text{each } i$$

where V is interpolated from the Z, V data, using e^2 from 7.5.2, α from 7.3.16, e_T from 7.3.15, and e_m from 7.3.14.

7.5.4 For each i, we now have an X (from 7.3.17) and a Y_F^2 (from 7.5.3). Solve by curve-fitting a second-degree polynomial (by least squares) for the coefficients A_F, B_F, C_F of

$$Y_F^2 = A_F X^2 + B_F X + C_F$$

(Do not confuse this C_F with C_f of step 7.3.10!)

7.5.5 Call:

$$\tau_F = (A_F)^{\frac{1}{2}}, \qquad \sigma_F = (C_F)^{\frac{1}{2}} \qquad \text{each } y.$$

7.5.6 Now consider the Z's matching the F's of step 7.5.1. Compute:

$$Z_F^2 = \frac{t_1^2 (Z^2 - Z_N^2)}{G^2}$$

with t_1, G, Z_N from Table 1 as before. If $(Z^2 - Z_N^2)$ is negative, set to zero.

7.5.7 Again form:

$$Y_{FF}^2 = \frac{Z_F^2}{(\alpha e_T + e_m)^2 V^2} \qquad \text{each } i$$

as in step 7.5.3.

7.5.8 Repeat the procedure of step 7.5.4: Find A_{FF}, B_{FF}, C_{FF} from:

$$Y_{FF}^2 = A_{FF}X^2 + B_{FF}X + C_{FF}$$

with X from 7.3.17 as always.

7.5.9 Form:

$$\Lambda_u = \frac{u'}{4} \frac{A_F}{A_{FF}}$$

with u' = 63,600 u (us is from WEM-II output). A_F is from step 7.5.4, A_{FF} from step 7.5.8.

7.5.10 Also form:

$$\Lambda_T = \frac{u'}{4} \frac{C_F}{C_{FF}}$$

with u', C_F, C_{FF} as per above.

7.5.11 Also form:

$$\frac{\Lambda_u}{D} = \frac{\Lambda_u}{2.54}$$

where Λ_u is from step 7.5.9 (i.e., column LAMBDA(U) of printout) and

$$\frac{\Lambda_T}{D} = \frac{\Lambda_T}{2.54}$$

with Λ_T from step 7.5.10 (i.e., column LAMBDA(T) of printout).

<u>Note</u>: Print the matrix for the X, i, Y_F, and X, i and Y_{FF} in a way exactly analogous to the matrix X, i, Y of page 12.

FINAL PRINTOUT

INTENSITIES

Experiment:_____, x = _____

Y/D	TAU	SIGMA	R(ST)	SRA	u'/u_∞	T'/T_∞	$u'/\Delta u$	$T'/\Delta T$
.	.	.	.	.	.	.	.	.
.	.	.	.	.	.	.	.	.
.	.	.	.	.	.	.	.	.
.	.	.	.	.	.	.	.	.
.	.	.	.	.	.	.	.	.
.	.	.	.	.	.	.	.	.

SCALES

Y/D	LAMBDA(U)	LAMBDA(T)	LAM(U)/LAM(T)	LAM(U)/D	LAM(T)/D
.	.	.	.	.	.
.	.	.	.	.	.
.	.	.	.	.	.
.	.	.	.	.	.
.	.	.	.	.	.
.	.	.	.	.	.

APPENDIX E

A CRITERION ESTABLISHING A MINIMUN REYNOLDS NUMBER FOR THE EXISTENCE OF TURBULENCE

It would be helpful to devise a rule establishing a state of fluid flow below which turbulence cannot "exist". There is presently controversy as to whether the turbulent boundary-layer remnant shed into a near wake continues "seeding" the near wake with turbulence, or whether it get completely and quickly obliterated by the shoulder expansion. Theoretical estimates of near-wake turbulence behavior (References 18 and 32) already imply that the effectiveness of such anti-transition hinges on the magnitude of the turbulence Reynolds number

$$Re_\Lambda = \frac{u'\Lambda}{\nu}$$

where u' is the velocity fluctuation, Λ the turbulence scale and ν the kinematic viscosity.

A very approximate criterion can be found as follows: a fluid element moving with speed u' relative to its adjacent fluid loses this speed because of viscous friction. On purely theoretical grounds the element has a finite lifetime τ_t beyond which its speed finally becomes uniform with that of the adjacent fluid, and thus the element ceases being identifiable. During its lifetime τ_t each element traverses a "life-distance" $s = u'/\tau_t$. To qualify as a component of turbulent flow, an element must have a finite life-time τ_t and a distinguishable life-distance s. Here we postulate that the minimum s for element identification is the element ("eddy") size itself (i.e., turbulence is not defined to exist unless the eddies travel a distance at least equal to their own size); that is, for turbulence to exist we require

$$u'\tau = s = \Lambda \tag{E-1}$$

Kovasznay (Reference 4) finds for the lifetime of convected vorticity:

$$\tau = \frac{1}{k^2\nu} = \frac{\Lambda^2}{(2\pi)^2}\,\frac{1}{\nu} \tag{E-2}$$

so that when we combine (E-1) and (E-2) we get a turbulence Reynolds number

$$Re_\Lambda = \frac{u'\Lambda}{\nu} = (2\pi)^2 = 40$$

below which "turbulence cannot exist".

REFERENCES

1. Laderman, A. J. and Demetriades, A., "Turbulence Measurements in the Hypersonic Boundary-Layer over a Cooled Wall," Philco-Ford publication No. U-5079, Newport Beach, California, Sept. 1972.

2. Laderman, A. J. and Demetriades, A., "Mean Flow Measurements in a Hypersonic Turbulent Boundary-Layer," Philco-Ford publication No. U-4950, Newport Beach, Calif., August 1971.

3. Owen, F. K., "Experimental Study of Nozzle Wall Boundary-Layers at Mach Numbers 20 to 47," NASA TN D-6965, Washington, D.C., October 1972.

4. Kovasznay, L. S. G., "Turbulence in Supersonic Flow," J. A. S. Vol. 20, No. 10, p. 657, 1953.

5. Demetriades, A., Final Technical Report, Advanced Penetration Program III, SAMSO-TR-72-161, April 1972.

6. (No author), Test Facilities Handbook, Arnold Engineering Development Center, Arnold Air Force Station, Tennessee, July 1971.

7. Martellucci, A., et al., "Effects of Mass Addition and Angle of Attack on Turbulent Boundary Layer Characteristics of a Slender Cone," General Electric Company report GE-TIS-73-SD210, Philadelphia, Pa., March 1973 (to be published).

8. Doughman, E. L., "Development of a Hot-Wire Anemometer for Hypersonic Turbulent Flow," Review of Scientific Instruments 43, No. 8, p 1200, August 1972.

9. Kistler, A. L., "Fluctuation Measurements in a Supersonic Turbulent Boundary Layer," Phys. of Fluids, 2, p. 290, 1959.

10. Fischer, M. C., Maddalon, D. V., Weinstein, L. M. and Wagner, R. D., "Boundary Layer Pitot and Hot-wire Surveys at $M_\infty \approx 20$," AIAA Journal 9, No. 5, p. 826, May 1971.

11. Fischer, M. C. and Weinstein, L. M., "Cone Transitional Boundary Layer Structure of $M_e = 14$," AIAA Journal 10, No. 5, p. 699, May 1972.

12. Potter, J. L. and Whitfield, J. P., "Boundary Layer Transition under Hypersonic Conditions," AGARDograph 97, Pt. 3, 1965.

13. Townsend, A. A., "The Structure of the Turbulent Boundary Layer," Proc. Cambridge Phil. Soc. Vol. 47, Part 2, p. 375, 1951.

14. Klebanoff, P. S., "Characteristics of Turbulence in a Boundary-Layer with Zero Pressure Gradient," NACA TR No. 1247, 1955.

REFERENCES (Continued)

15. Morkovin, M. V., "Effects of Compressibility on Turbulent Flows," Mecanique de la Turbulence, Centre Nat'l de la Recherche Scientifique, 15 Quai Anatole France, Paris, France, p 367, 1962.

16. Morkovin, M. V. and Phinney, R. E., "Extended Applications of Hot-Wire Anemometry to High-Speed Turbulent Boundary-Layers," AFOSR TN-58-469 (ASTIA AD-158-279), Johns Hopkins Univ., 1958.

17. Morkovin, M. V., "Fluctuation and Hot-Wire Anemometry in Compressible Flows," AGARDograph No. 24, 1956.

18. Finson, M. L., "Hypersonic Wake Aerodynamics at High Reynolds Numbers," AIAA Paper 72-701, Boston, Mass. June 26, 1972.

19. Demetriades, A., "Mean Flow in Turbulent Near Wake," APP Data Report, Philco-Ford Corp., Newport Beach, Calif. 1972.

20. Demetriades, A., "Semi-Annual Progress Report, Advanced Penetration Problems," SAMSO TR 69-312, Los Angeles, Calif., May 15, 1969.

21. Townsend, A. A., "The Structure of Turbulent Shear Flow," Cambridge Univ. Press, 1956.

22. Demetriades, A., "Mean Flow Measurements in an Axi-symmetric Compressible Turbulent Wake," Philco-Ford publication No. U-3978, Newport Beach, Calif. March 1, 1967.

23. Demetriades, A., "Mean Flow Measurements in an Axi-symmetric Compressible Turbulent Wake," AIAA J. Vol. 6, No. 3, p 432, March 1968.

24. Gran, R. L., "A Wind-Tunnel Study of the Post-Boundary-Layer Transition Near Wake of a Cone at Mach 7.5," Proc. of 1972 Low-Altitude Workshop, B. Wolberg, ed., RRI Document No. 72-1183, New York, N. Y., Feb. 1972.

25. Demetriades, A. and Doughman, E. L., "Mean Flow Measurements in a Self-Preserving Turbulent Plasma Jet," SAMSO TR 68-166, Los Angeles, Calif., Feb. 1968.

26. Demetriades, A., Doughman, E. L. and Von Seggern, L., "Intermittency Measurements in a Turbulent Plasma Jet," SAMSO TR 69-138, Los Angeles, Calif., June 1969.

27. Demetriades, A., Doughman, E. L. and Von Seggern, L., "Gasdynamical and Electronic Turbulence in a Plasma Jet," Philco-Ford publication No. UG-4820, Newport Beach, Calif., April 1970.

REFERENCES (Continued)

28. Demetriades, A. and Grabow, R., "Mean and Fluctuating Electron Density in Equilibrium Turbulent Boundary Layers," AIAA J. Vol. 4, No. 8, p 1533, August 1971.

29. Lin, S. C. and Hayes, J. E., "A Quasi-One-Dimensional Treatment of Chemical Reactions in Turbulent Wakes of Hypersonic Objects," AIAA J. Vol. 2, No. 7, p 1214, July 1964.

30. Proudian, A. P. and Feldman, S., "A New Model for Mixing and Fluctuations in a Turbulent Wake," AIAA J. Vol. 3, No. 4, p. 602, April 1965.

31. Shapiro, A. H., "The Dynamics and Thermodynamics of Compressible Fluid Flow," Vol. II, Ronald Press Co., New York, 1953.

32. Hinze, J. O., "Turbulence," McGraw-Hill Book Co., New York, N. Y., 1959.

Unclassified
Security Classification

DOCUMENT CONTROL DATA - R & D

(Security classification of title, body of abstract and indexing annotation must be entered when the overall report is classified)

1. ORIGINATING ACTIVITY (Corporate author) Aeronutronic Division Philco-Ford Corporation Newport Beach, California	2a. REPORT SECURITY CLASSIFICATION Unclassified 2b. GROUP

3. REPORT TITLE
Final Technical Report
Advanced Penetration
Advanced Penetration Program

4. DESCRIPTIVE NOTES (Type of report and inclusive dates)
Final Technical Report

5. AUTHOR(S) (First name, middle initial, last name)
Anthony Demetriades and Arnold J. Laderman

6. REPORT DATE February 1973	7a. TOTAL NO. OF PAGES 148	7b. NO. OF REFS 32
8a. CONTRACT OR GRANT NO. F04701-71-C-0035 b. PROJECT NO. c. none d.	9a. ORIGINATOR'S REPORT NUMBER(S) U-6002 9b. OTHER REPORT NO(S) (Any other numbers that may be assigned this report) SAMSO TR No. 73-129	

10. DISTRIBUTION STATEMENT Distribution limited to U.S. Government Agencies only; Reason: Test and Evaluation; Date statement applied; 1 April 1972 Other requests for this document must be referred to Space and Missile Systems Organization (RSSE), Los Angeles, California 90009.

11. SUPPLEMENTARY NOTES none	12. SPONSORING MILITARY ACTIVITY

13. ABSTRACT

The study of turbulence on a flat plate at Mach 9.4 has been completed with the discovery that the pressure fluctuations predominate, that the velocity fluctuations are very small and that wall-cooling has a strong influence in decreasing the temperature fluctuations. Tests have been performed at AEDC/B to extend these results to the cone geometry, to broaden the Mach- and Reynolds-numbers matrix and to investigate ablation effects. Although still incomplete, analysis of the data show very large temperature fluctuations due to the adiabatic wall, relatively little change of the turbulence level past the transition point, and discernible but small fluctuation increase for small mass injection rates. Correlations have began of all the available boundary-layer turbulence data for the purpose of scaling the fluctuation distribution to arbitrary flight conditions. Thus far the available correlation schemes fit the velocity fluctuation data only in the outer half of the layer. Better success is enjoyed for the temperature difference between the wall and the external flow. Experiments were also conducted to measure the traverse velocity fluctuation component and the turbulent shear stresses with specially-developed hot-wire probes; these data are now available on tape. In the near-wake investigation the completed mean-flow measurements were analyzed and show that a "plateau" tends to form as the Reynolds number increases beyond BLT. The turbulent viscosity was measured and found to decrease beyond BLT as predicted by the AVCO theory. Other theoretical predictions, such as the radial distribution of velocity beyond the neck, were also verified. Fluctuation measurements revealed that the shoulder expansion nearly destroys the velocity but not the temperature fluctuations, and that the wake is "double-structured" beyond the neck. The study of electron, velocity and temperature space-time correlations in the far wake has been completed.

DD FORM 1473

Unclassified
Security Classification

14 KEY WORDS	LINK A		LINK B		LINK C	
	ROLE	WT	ROLE	WT	ROLE	WT